

**Analysis of a Mechanically Ventilated Multiple-skin Facade
with Between-the-Panes Venetian Blinds**

by

Omid Nemati

A thesis
presented to the University of Waterloo
in fulfillment of the
thesis requirement for the degree of
Master of Applied Science
in
Mechanical Engineering

Waterloo, Ontario, Canada, 2009
© Omid Nemati 2009

I hereby declare that I am the sole author of this thesis. This is a true copy of the thesis, including any required final revisions, as accepted by my examiners.

I understand that my thesis may be made electronically available to the public.

ABSTRACT

A Building Integrated Photovoltaic/Thermal (BIPV/T) system that consists of a mechanically ventilated, multi-skin facade, a between-the-panes venetian blind layer, and a between-the-panes Photovoltaic (PV) panel is considered. Ambient air is drawn in and forced to flow upward through the system. As air moves through the system, it is heated by the blind layer, the glazing layers, and the PV panel. This BIPV/T system is especially attractive because it can produce electricity and thermal energy in the form of preheated fresh air and allow for adjustable daylighting.

There is a need to understand, design, and optimize BIPV/T systems. The velocity and temperature fields around the blind slats were experimentally and numerically studied. Experimental observations and numerical models are essential in understanding the complex fluid dynamical and thermal system and providing design and optimization guidelines. Solar-optical and Computational Fluid Dynamics (CFD) models were developed and validated at various blind slat angles and flow mean speeds. Particle Image Velocimetry (PIV) and temperature measurements were taken inside the ventilated facade. A simple empirical one-dimensional (1-D) model was developed, based on average surface temperatures and heat transfer coefficients, to quickly

calculate average surface temperatures and heat flux rates. Between-the-panes convective heat transfer coefficients were obtained from CFD and used in the 1-D model. Despite high vertical temperature stratifications along the glazing, shading, and air layers, the 1-D model can predict the surface temperatures accurately and allow for future optimization and inclusion in building energy simulation software.

ACKNOWLEDGEMENTS

Throughout my research in the University of Waterloo, I had the opportunity to work with my supervisor, Professor Michael R. Collins, who I am greatly indebted to. I greatly appreciate his patience, guidance and academic support. It has been a very rewarding learning experience to work with him over the years, and this thesis would not have been completed without his help. I am also thankful to Professor John L. Wright for his wisdom and encouragement. I would like to thank Professors David Johnson and Gerry Schneider for reviewing my thesis.

I would like to thank the students of the Solar Thermal Laboratory, Nathan for sharing his insights on the subject of the research, and Neil, Bart, Victor, Veronique, Sebastien, Andrew, and Hani for providing a friendly work environment.

During my brief visits to Concordia University, I was very fortunate to work with Professor Andreas K. Athienitis and his student, Luis Candanado, who were very patient and tolerant of my requests.

I acknowledge the financial support of the Solar Buildings Research Network (SBRN), a strategic NSERC (Natural Sciences and Engineering Research Council of Canada) research network.

TABLE OF CONTENTS

LIST OF TABLES	x
LIST OF FIGURES	xi
NOMENCLATURE	xv
CHAPTER 1 INTRODUCTION	1
1.1 FENESTRATION MATERIALS	2
1.1.1 The glazing	4
1.1.2 Low-emissivity Coatings	6
1.1.3 Building-Integrated Photovoltaics	7
1.1.4 Air Flow Windows	8
1.1.5 Between-the-Panes Venetian Blinds	10
1.2 MOTIVATION	11
1.3 OBJECTIVES	13
1.4 THESIS LAYOUT	15
CHAPTER 2 PREVIOUS STUDIES OF BUILDING- INTEGRATED PHOTOVOLTAICS	16
2.1 SOLAR-OPTICAL STUDIES	18
2.1.1 Glazing Layers	18
2.1.2 Venetian Blinds	20
2.2 THERMAL AND FLUID DYNAMIC STUDIES	22
2.2.1 Vertical Walls	32
2.2.2 Venetian Blinds	33
CHAPTER 3 NUMERICAL MODEL DEVELOPMENT	35
3.1 SOLAR-THERMAL SEPARATION	36

3.2 SOLAR-OPTICAL MODEL	36
3.3 CFD MODEL DEVELOPMENT	38
3.3.1 Model Geometry	41
3.3.2 Boundary Conditions	42
3.3.3 Turbulence and Near Wall Modelling	45
3.3.4 Radiation Model	49
3.4 CFD BASIC FLUID DYNAMIC VALIDATION	50
3.5 MESH GENERATION	51
3.5.1 Mesh Independence	52
3.5.2 Near Wall Mesh Generation	53
CHAPTER 4 MODEL VALIDATION	56
4.1 SYSTEM DESCRIPTION	59
4.2 EXPERIMENTAL PROCEDURE	59
4.3 PIV EQUIPMENT SETUP	62
4.4 PIV CORRELATION, VALIDATION AND MASKING	64
4.5 PIV UNCERTAINTY ESTIMATION	68
4.5.1 Particle Displacement	68
4.5.2 Standard Deviation	69
4.5.3 Dynamic Velocity and Spatial Ranges	70
4.6 VELOCITY FIELD VALIDATION	72
4.7 TEMPERATURE VALIDATION	83
4.6 RESULTS	87
CHAPTER 5 SIMPLIFIED APPROACH	90
5.1 MODEL DESCRIPTION	91
5.1.1 Long-wave Radiation Heat Transfer	93
5.1.2 Between-the-Panes Convective Heat Transfer Coefficients	93
5.2 MODEL VALIDATION	99
5.3 PARAMETRIC ANALYSIS	99
5.4 SOLAR AND THERMAL GAINS	106
CHAPTER 6 CONCLUSIONS	108

REFERENCES	111
APPENDICES	115
APPENDIX 1 SOLAR-OPTICAL AND LONG-WAVE MEASUREMENTS OF THE BLIND SLAT	115
APPENDIX 2 THE VENETIAN BLIND MODEL	117
APPENDIX 3 THE SOLAR ABSORPTION MODEL	124
APPENDIX 4 THE THERMAL RESISTOR NETWORK	126

LIST OF TABLES

Table 3.1	Solar-optical glazing and shading surface properties	37
Table 3.2	Absorbed fluxes in each layer	38
Table 3.3	Venetian blind spatially-averaged (effective) properties	38
Table 3.4	Summary of the boundary conditions	46
Table 3.5	Hemispherical long-wave emissivity and total reflectivity of Surfaces	50
Table 4.1	Some control and measurement equipment	59
Table 4.2	Experimental scenario design	60

LIST OF FIGURES

Figure 1.1	Temperature dependence of the peak power generation at various irradiation levels (reproduced from Davis et al., 2001).	8
Figure 1.2	Two typical AFW arrangements: supply-air and exhaust-air.	11
Figure 1.3	Schematic of the two BIPV/T setups at Concordia University.	14
Figure 2.1	Figure 2.1: Recursive summation of multiple transmissions and reflections (Edward's, 1977).	19
Figure 2.2	The four surface and the six surface enclosures used to determine the beam-to-beam, beam-to-diffuse, and diffuse-to-diffuse venetian blinds effective properties	21
Figure 2.3	U- and g-value analysis (reproduced from Infield et al., 2004).	23
Figure 2.4	Air flow in a transparent ventilated cavity and the long-wave radiation exchange between the control volumes (reproduced from Ismail, 2006).	24
Figure 2.5	A BIPV/T system consisting of a PV panel and a double glazing unit (reproduced from Mei, 2005).	29
Figure 2.6	Schematic of a double facade, the direction of air flow for a south-oriented facade with a south wind, and an example of wind pressure coefficients on a building (reproduce from Gratia and De Herde, 2004).	32
Figure 2.7	Flat plate approximations for vertical walls and porous medium representation for venetian blinds (reproduced from Safer et al., 2005).	33
Figure 3.1	The flow domain and boundary conditions.	43

Figure 3.2	Streamwise velocity at a height of 2 m (adapted from Safer et al., 2005).	51
Figure 3.3	The mesh at $\varphi = 0^\circ$.	52
Figure 3.4	Mesh independence test.	53
Figure 3.5	Vertical wall y^+ plots, 10 Hz, 20 Hz, 30 Hz, $\varphi = 0^\circ$.	55
Figure 4.1	The two BIPV/T configurations at Concordia University, a schematic of the Spheral-Solar™ configuration, the location of thermocouples and the plane of PIV measurements.	57
Figure 4.2	The PIV equipment setup.	63
Figure 4.3	An example of the correlation plane	65
Figure 4.4	The super-resolution (adaptive correlation) algorithm showing Interrogation area subdivision (reproduced from FlowManager, 2002).	66
Figure 4.5	A typical PIV picture showing the laser sheet shading on the right side of the slats and the mask.	68
Figure 4.6	The instantaneous velocity field, fan speed = 10 Hz, $V_{in} = 0.13$ m/s.	75
Figure 4.7	The instantaneous velocity field, fan speed = 20 Hz, $V_{in} = 0.31$ m/s.	76
Figure 4.8	The instantaneous velocity field, fan speed = 30 Hz, $V_{in} = 0.56$ m/s.	76
Figure 4.9	Another instantaneous velocity field at 30 Hz, $V_{in} = 0.56$ m/s.	78
Figure 4.10	The streamline contours from CFD.	79
Figure 4.11	Approximate streamline contours and velocity vector field, $\varphi = 0^\circ$, fan speed = 10 Hz, $V_{in} = 0.13$ m/s.	80
Figure 4.12	Approximate streamline contours and velocity vector field, $\varphi = 0^\circ$, fan speed = 20 Hz, $V_{in} = 0.31$ m/s.	81
Figure 4.13	Approximate streamline contours and velocity vector field, $\varphi = 0^\circ$, fan speed = 30 Hz, $V_{in} = 0.56$ m/s.	82

Figure 4.14	Streamwise profile from PIV and CFD, mid-height between slats 8 and 9, and 9 and 10, 10 Hz, $V_{in} = 0.13$ m/s.	83
Figure 4.15	Streamwise profile from PIV and CFD, mid-height between slats 8 and 9, and 9 and 10, 30 Hz, $V_{in} = 0.56$ m/s.	83
Figure 4.16	Experimental temperature readings and corresponding CFD predictions, $\phi = 0^\circ$.	85
Figure 4.17	Experimental temperature readings and corresponding CFD predictions, $\phi = 45^\circ$.	86
Figure 4.18	Experimental temperature readings and corresponding CFD predictions, $\phi = 75^\circ$.	87
Figure 4.19	Streamwise velocity profile mid-height between slats 8 to 9, $y = 431.7$ mm, and 9 to 10, $y = 475.6$ mm.	89
Figure 5.1	Thermal resistor network.	92
Figure 5.2	Local slat-to-slat energy balance and heat fluxes.	95
Figure 5.3	Vertical radiative and total heat transfer rate profiles, $\phi = 0$, 10 Hz.	96
Figure 5.4	Actual air flow around blind slats on the left. Blind representation on the right.	98
Figure 5.5	Average convective heat transfer coefficients.	95
Figure 5.6	1-D and CFD temperature predictions against experimental readings, Scenarios 1, 2 and 3, $\phi = 0$, $I_{tot} = 680$ W/m ² , $T_{int} = 22.8^\circ\text{C}$, $T_{ext} = 13.0^\circ\text{C}$.	100
Figure 5.7	1-D and CFD temperature predictions against experimental readings, Scenarios 4, 5, and 6, $\phi = 45^\circ$, $I_{tot} = 650$ W/m ² , $T_{int} = 22.0^\circ\text{C}$, $T_{ext} = 10.8^\circ\text{C}$.	101
Figure 5.8	1-D and CFD temperature predictions against experimental readings, Scenarios 7, 8 and 9, $\phi = 75^\circ$, $I_{tot} = 692$ W/m ² , $T_{int} = 22.2^\circ\text{C}$, $T_{ext} = 13.1^\circ\text{C}$.	102
Figure 5.9	q_{air} vs. $h_{c,in}$ and $h_{c,out}$.	104
Figure 5.10	q_{air} vs. I_b , V_{in} , T_{in} , ϕ .	105
Figure 5.11	Solar and thermal Gains.	107

Figure A1.1	Spectral normal-hemispherical solar reflectivity of the blind slat.	116
Figure A1.2	The long-wave emissivity of the blind slat.	116

NOMENCLATURE

Abbreviations

AFW	Air Flow Window
BIPV/T	Building Integrated Photovoltaic/Thermal
CCD	Coupled-Charged Device
CHTC	Convective Heat Transfer Coefficient, $\text{W/m}^2\text{-K}$
EWT	Enhanced Wall Treatment
GDF	Glass Double Facade
PCM	Phase Change Materials
PIV	Particle Image Velocimetry
PV	Photovoltaic
SHGC	Solar Heat Gain Coefficient
SWF	Standard Wall Function

Symbols

c_p	Specific Heat, J/kg
ΔC_p	Coefficient of pressure difference
D_h	Hydraulic diameter
g	Gravitational acceleration, m/s^2
\dot{g}	Heat generation rate, W/m^3
g_{trans}	Solar Transmission heat gain across the window
g_{vent}	Solar Transmission heat gain to the channel air
Gr	Grashof number

h	Heat Transfer Coefficient, W/m^2-K
H	Height of window, mm
I	Solar radiation flux, W/m^2
k	Turbulent kinetic energy, m^2/s^2
K	Thermal Conductivity, $W/m-K$
N	Sample size
Nu	Nusselt number
Nu_l	Laminar Nusselt number
Nu_t	Turbulent Nusselt number
P	Pressure, Pa
P_g	Gauge Pressure, Pa
Pr	Prandtl number
q	Enthalpy, J/kg
\dot{q}''	Heat flux rate, W/m^2
q_{air}	The air thermal gain, W/m^2
q_{in}	The convective and radiative heat flux from the inner-most pane to the indoor environment, W/m^2
Q_v	Air flow rate, m^3/s
Re	Reynolds' number
s	Blind slat spacing, mm
St	Stanton number
T	Temperature, $^{\circ}C$
$T.I.$	Turbulent Intensity
U	Velocity component in the X- direction
U_{trans}	Solar transmission heat loss across the window, W/m^2-K
U_{vent}	Solar transmission heat loss from interior to the channel air, W/m^2-K
V	Velocity component in the Y- direction
w	Width of cavity, mm
w_{eff}	Effective width of cavity, mm
X	Axis direction

Y Axis direction

Greek Symbols

ε Emissivity
 ε_k Rate of dissipation of turbulent kinetic energy, m^2/s^3
 ε_s Surface Roughness, m
 μ viscosity, kg/ms
 ρ Density, kg/m^3
 ρ_{bb} Beam-to-beam reflectivity
 ρ_{bd} Beam-to-diffuse reflectivity
 ρ_d Diffuse Incidence reflectivity
 ρ_{dd} Diffuse-to-diffuse reflectivity
 ρ_n Normal Incidence reflectivity
 σ Standard deviation
 σ_u rms in PIV velocity calculations, m/s
 τ_{bb} Beam-to-beam transmissivity
 τ_{bd} Beam-to-diffuse transmissivity
 τ_d Diffuse Incidence transmissivity
 τ_{dd} Diffuse-to-diffuse transmissivity
 τ_n Normal Incidence transmissivity
 θ Angle of incidence, degrees
 φ Blind slat angle, degrees
 Ω Profile angle, degrees

Subscripts

b Back
b Blind
c Convective
ext Outdoor environment
f Front

g	Glazing
i	Indoor glazing, adjacent to the ventilated cavity
ii	Indoor glazing, adjacent to the indoor environment
in	Inlet
int	Indoor environment
lw	Long-wave
λ	Wavelength, m
n	Normal Incidence
o	Outdoor glazing
out	Outlet
r	Radiative
tot	Total
tra	Transmitted

CHAPTER 1

INTRODUCTION

Buildings consume about 40% of the total energy used in Canada, with space heating accounting for 59.3% and 50.3% of the energy consumed in the residential and commercial sectors, respectively (NRCan, 2008). Thus, space heating accounts for a considerable portion of our national energy demand, owing to the cold Canadian climate. In recent years, energy conservation and energy efficiency have become topics of major international importance due to the growing energy demand of all countries, including Canada. To meet this demand, we must implement energy saving and energy efficiency strategies in our buildings.

In buildings, heat loss through windows is responsible for much of the space heating requirement. Many improvements in window technology are aimed at reducing the fenestration total thermal transmittance (U-value) while satisfying daylighting and noise requirements. These improvements include the emergence of glass double facades (GDFs), low-emissivity coatings, low-conductivity substitute fill gases, spectrally-selective coatings, switchable glazings, tinted glazings, and windows with Phase Change Materials (PCMs), such as photocromatics, thermocromatics, and electro-

chromatics. More recent improvements, however, aim to achieve all the aforementioned objectives, while reducing the Heating, Ventilation, and Air Conditioning (HVAC) load of the building, as much as possible.

For residential buildings various PV technologies that produce electricity on-site have been tested and implemented. Amorphous and crystalline PV modules can be mounted on roof tops or used as part of atrium glazing, shading devices, semi-transparent windows or wall cladding. Due to decreasing production costs and the rising electricity prices, PV is becoming more popular in building designs.

BIPV/T systems are very recent advances in window technology that combine PV technologies with thermal collection techniques to offset the cost of both electricity and space heating. These systems are very attractive in building design because they can produce higher overall savings than the stand-alone PV or thermal systems, especially during the heating season.

1.1 FENESTRATION MATERIALS

Windows are commonly used to allow the passage of daylight and provide fresh air. With smart design, sunlight can be used to the advantage of the building designers. The first paper on the effective use of glass was published by Jacob Forst in a U.K. horticultural periodical. It suggested that, with a smart design, a green-house effect can be used to help produce crops. The sun's rays can pass through windows, enter a room,

warm the objects in the room, which in turn warm the air, and then the warmed air can circulate through the building. This is what we know today as a passive solar arrangement (Wigginton and McCarthy, 2000).

The first solar wall, known today as the Trombe-Michel wall, was first built by E.L. Morse in 1882. He placed a layer of iron behind a glazing layer with the idea that the sun's rays can produce heat when shining on a dark piece of metal. The idea of solar walls was popularized in the 1970's when F. Trombe and J. Michel reintroduced (and repatented) the idea (Trombe et al., 1977, and Wigginton and McCarthy, 2000). Trombe-Michel walls are sometimes referred to as thermal storage walls, collector storage walls, or simply solar walls.

Double membrane walls were used extensively in the building facades of French designer, Le Corbusier, in the first half of the 20th century. The walls, sometimes up to two stories high, were placed a few centimeters apart and were made of glass, stone, or a mix of both. The idea was that double membrane walls provide added insulation and can allow the passage of fresh air through them. He proposed that mechanical ventilation be used in between the double membrane walls to guarantee comfortable internal climate conditions (Compagno, 2005). Although not all Le Corbusier's projects met with success, and although he did not subject his designs to rigorous scientific testing, his ideas of double membrane walls were inspiring to others (Wigginton and McCarthy, 2000).

The first double glazing unit was produced in 1935 by Libbey Owens and was named the “thermopane”. It consisted of two glazing layers, separated by a 12 mm hermetically sealed air gap. Double glazing units, double membrane walls, and passive solar arrangements were analyzed through the first half of the 20th century as people sought to better understand how buildings could be constructed to promote greater efficiency and comfort. By the 1960s double glazing units were significant design features.

A significant step in the development of double glazing facades was the double glazing unit built in 1961 by A.E. Morgan for a school. The outdoor layer was clear, but the indoor layer was partially translucent and contained some reversible panels. These panels were black on one side and coated with an aluminum layer on the other. The glazing layers were separated by a 600 mm air gap. This design received much recognition because, without the help of any mechanical ventilation, the facade could be altered to accommodate the occupants’ thermal and illumination needs. Depending on which side of the inner layer was facing the sun, the solar energy could be absorbed or reflected (Wigginton and McCarthy, 2000).

1.1.1 The Glazing

Glass is the primary glazing material used in window construction. It is a somewhat unique material in that its optical properties vary significantly depending on the source of incident rays. It transmits most of the solar rays, but absorbs most of the long-wave radiation emitted from surfaces of the objects located in either side of the glazing. Therefore, it can provide occupants with natural daylight, and it can also block the

direct radiation heat exchange between the indoor and outdoor environment. Even though the glazing is opaque to long-wave radiation, it turns out that it cannot eliminate the long-wave radiation exchange between objects in the indoor and in the outdoor environment. In fact, the glazing can only marginally suppress the magnitude of this radiation exchange across the glazing, because of the high emissivity of the material in the long-wave range (about 0.84 for soda-lime glass). High emissivity of the glazing results in near-to-maximum radiative heat exchange between the glazings and the surroundings. The glazing merely acts as an intermediate medium where heat is transferred from one side to the glazing, conducted through the glazing, and then dissipated to the other side.

Aside from the radiative heat transfer across the glazing, convective heat transfer also occurs on both sides: mainly free convection on the indoor side and forced convection on the outdoor side.

For a material to be best suited in window applications it must insulate as much as possible against radiative and conductive heat exchange across the window. It must also allow for solar illumination. Hence, it must be a “transparent insulator” (Hollands et al., 2001). Finding such materials that satisfy both criteria simultaneously is not a straightforward task. The glazing acts as a good solar transmitter but does not act as a good insulator. In the last two or three decades, advances in window technology have been mainly aimed at introducing new material, such as the glazing, low-e coatings, and

substitute fill gases, to augment the glazing, rather than introducing new material to replace the glazing.

It is not sufficient for window material (or combination of materials) to be a transparent insulator; it must also eliminate occasional overheating problems in the winter season and overcooling in the summer. For example, an excess amount of sunlight in winter can actually result in overheating of a building. Even though shades and drapes can help control the passage of sunlight, overheating can still be a problem. An efficient window is the one that can adjust its optical properties according to the environmental conditions to satisfy the building occupants' comfort level and their changing thermal-illumination needs (Hollands et al., 2001). Such a window is called "switchable".

1.1.2 Low-Emissivity Coatings

Low-emissivity coatings were introduced to the North American market in the early 1980's (Limb, 2002). They can reduce the heating and cooling requirement by more than 50% while achieving daylight requirements (Santamouris, 2001). They are made of material that is highly-reflective in the long-wave, such as metals.

When applied on the surface of a glazing they can reduce the surface emissivity from 0.84 to as low as 0.05, without significantly impacting the solar transmission (a few percentage drop in solar transmissivity). The high reflectivity or low emissivity of the coating in the long-wave reduces the radiative heat transfer from the surface of the glazing, hence reducing the fenestration total heat loss.

Low-emissivity coatings can be applied on any side of a glazing layer. In GDFs they are normally placed on the glass surface facing into the window cavity. In that location, they are protected from damage. Depending on the climate two types of low-emissivity options are available, the ones that have high solar transmittance and the ones that have lower solar transmittance. In Canada the high solar transmittance type is used due to the colder climate.

1.1.3 Building-Integrated Photovoltaics

PV technologies can be used in residential and office buildings to supplement the power taken from the electrical grid or even put power back when electricity is not needed by the building. A typical arrangement for a building-integrated PV is a double-skin facade where PV is placed as part of the outdoor skin, facing the sun directly, and transparent (glazing) or opaque (insulating) walls are placed as part of the indoor skin. PV panels can be installed on the rooftops or on south-facing facades. Rooftop PV panels are advantageous in that they convert more solar energy into electricity due to smaller angles of incidence, but they require a separate mounting structure. Vertical south-facing facades are advantageous, in the northern hemisphere, over vertical non-south-facing facades because they can receive more solar energy.

When integrated into facades, PV may have low construction and implementation costs because they require no separate mounting structure and also because they replace a building's expensive facade material, such as pre-cast walls.

The electrical conversion efficiency of the crystalline cells is about 8 to 16% at 25°C and it exhibits a linear relation with surface temperature (Figure 1.1). Efficiency decreases by about 0.5% for every degree rise in surface temperature (Davis et al., 2001). Despite low electrical efficiency PV can bring considerable combined electrical-thermal savings when a form of mechanical ventilation is used. At Concordia University the combined electrical and thermal efficiency of the BIPV/T systems, the sum of electrical and thermal gains divided by the total incident radiation, can be as high as 70-80% (Liao et al., 2007).

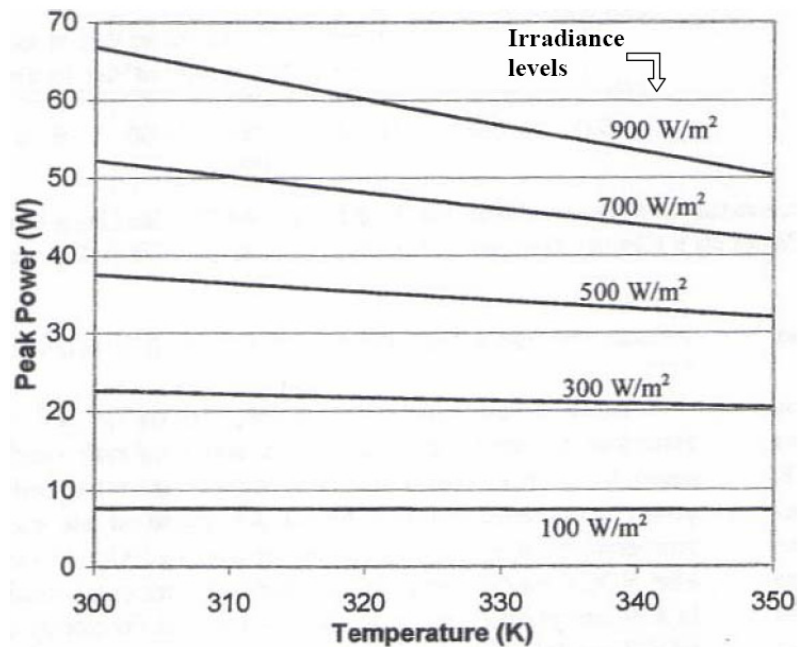


Figure 1.1: Temperature dependence of the peak power generation at various irradiation levels (reproduced from Davis et al., 2001).

1.1.4 Air Flow Windows

Air Flow Windows (AFWs) are ventilated, usually transparent, double-skin facades. The naturally ventilated forms rely on buoyancy and wind effects and have been used for centuries to provide added insulation, mitigate overheating and provide a source of preheated air to the building occupants. In multiple-storey buildings, such as office buildings, they can be designed in such a way that there would be one opening and one exhaust window in each floor, or they can be designed in such a way that only one very wide (about 1.0 m or wider) air column would exist extending all the way from the roof to the ground. In the latter case, each floor can still have one opening to take advantage of the fresh air inside the tall channel.

Despite increasing applicability, particularly in European countries, naturally ventilated AFWs have limitations. For example, naturally ventilated AFWs depend heavily on available solar radiation and proper orientation, and only with careful examination of local considerations may they be used. For a specific setup in Barcelona for example, 12% of the heating energy could be saved, whereas only 2% could be saved in Stuttgart and Loughborough (Mei et al., 2003). Other than the local limitations, the flow rates inside the channel are usually very limited. Further, poor design and inadequate sizing of the openings may result in inadequate fresh air, i.e., the “sick-building syndrome”.

Mechanically ventilated AFWs have the advantage over naturally ventilated AFWs in that they can provide higher flow rates and higher thermal savings. The first record of mechanical ventilation is from Jean-Baptiste Jobard (1849), then the director of the

industrial museum in Brussels, who proposed a double-glazing arrangement with hot air circulating inside in winter and cold air in summer (Saelens, 2002).

Mechanically ventilated windows can be operated in a number of modes, depending on the position of the inlet and outlet with respect to the indoor or outdoor environment, and also the direction of air flow. Two of the most important modes are “supply-air” and “exhaust-air”, because they can effectively reduce the heating and cooling load of a building, respectively (Figure 1.2). A ventilated window, in fact, must be capable of operation under various modes to ensure overall year-round benefits. During the heating season, a supply-air arrangement forms an insulating air layer between the indoor and outdoor environment and also brings heated air inside the building. During the cooling season, an exhaust-air arrangement can be used to reduce overheating. The air inside the building is forced to flow downward or upward through the window, and then exhausted to the outdoor environment. Forced flow lowers the surface temperatures and results in lower overall transmission gains.

1.1.5 Between-the-Panes Venetian Blinds

Shading devices such as venetian blinds are used in building applications to control daylight, reduce glare, and to control the U-value and the Solar Heat Gain Coefficient (SHGC). They are commonly placed on the indoor side of a glazing unit, but can also be placed in between a double- or multi-skin glazing arrangement. There are several advantages of placing a blind layer in a between-the-panes arrangement. It portrays an aesthetically pleasing look and increases thermal savings because of increased solar

absorption. It also facilitates the control and automation of the drive systems because it provides a location to safely place delicate mechanisms. In an experimental study, Rheault and Bilgen (1990) revealed that automated blind systems can reduce auxiliary energy requirements by about 30% in winter and 50% in summer for the Canadian climate.

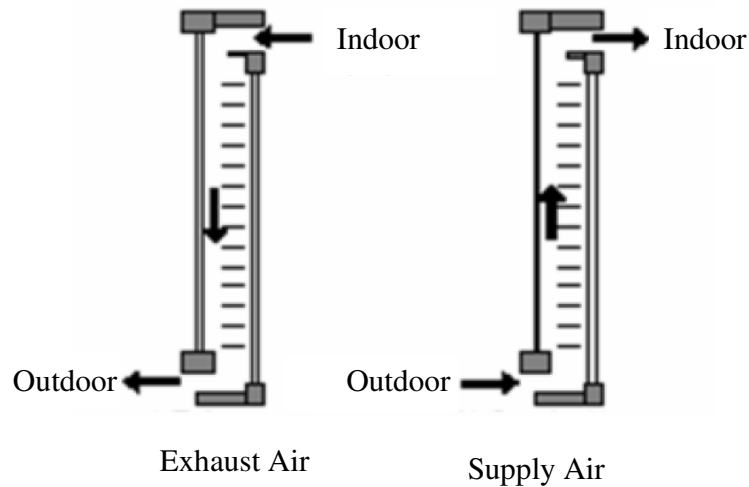


Figure 1.2: Two typical AFW arrangements: supply-air and exhaust-air.

1.2 MOTIVATION

The thermal savings achievable by BIPV/T systems, in the form of heated air, can be many times greater than the electricity generation. In air-based thermal systems the air gets preheated as it flows over a PV panel and the preheated air can be used inside the building as a source of fresh ventilation air. While water-based systems are possible, none exists to the author's knowledge, perhaps due to their complexity. While the electrical conversion efficiency of PV is very low, the thermal collection efficiency can

be as high as 50–70% (Liao et al., 2007). Combining PV and thermal collection techniques in one unit is very attractive in building design because each can enhance the effect of the other. In any solar system, an extra absorbing layer such as a PV layer can contribute to higher thermal gains, whereas forced ventilation around the PV panel can lower its temperature and, therefore, raise its electrical conversion efficiency.

Two BIPV/T setups have been constructed at Concordia University, on a rooftop test facility, to study the performance and potentials of BIPV/Ts (Figure 1.3). Each setup can be divided into two parts, a lower opaque PV part, and an upper adjustable shading and vision part. One configuration, hereafter referred to as the Photowatt™ configuration, uses the Photowatt™ panels placed directly behind a glazing cover and an insulating wall separating the PV from the indoor space, on the lower part. The shading device used in the upper part of this configuration is a roller blind, placed in the middle of a glass double glazing arrangement. The other configuration, hereafter referred to as the Spherical-Solar™ configuration, uses the Spherical-Solar™ panels, placed in the middle of a transparent glazing wall on the front, and an opaque insulating wall on the back. The shading device used in this configuration is a venetian blind layer. Variable-frequency fans induce forced flow through each setup, and the shading layers are adjustable and motorized.

The lower sections of both configurations have been studied at Concordia University. Experimental measurements were made at the test facility, and numerical 1–D, two-dimensional (2–D), and CFD models were developed (Liao et al., 2007, and Charron

and Athientitis, 2006). The upper section of the Photowatt™ configuration has also been experimentally and numerically studied (Hadlock, 2006). Preliminary results show that the combined electrical-thermal efficiency of the PV section of the Photowatt™ configuration is lower than that of the Spherical-solar™ configuration, because a higher portion of the incident solar radiation is readily lost to the outdoor environment. When PV panels are placed on the exterior layer of a fenestration system, facing the sun directly, about 70-80% of the incident solar radiation is lost to the outdoor environment in the form of convective and long-wave radiative heat transfer (Liao et al., 2007, and Charron and Athientitis, 2006). Placing the PV panels in between a double or multi-glazing arrangement is an alternative that can maximize the degree of overall solar utilization, because the circulating air can remove much of the heat that would otherwise be lost to the exterior.

The upper section of the Spherical-Solar™ configuration has not been studied to date. A review of literature on BIPV/Ts and double glazing facades reveals that the majority of work has focused in the past on natural convection between parallel plates (with or without shading devices) where the plates can be sealed at the ends or they can be open to the ambient air. There are very few studies that consider forced flow inside a double-glazing facade, with large flow obstructions (blind slats). The present work aims to provide a combined experimental and numerical study on the mechanically ventilated BIPV/T with venetian blinds and also to complete the understanding of the two BIPV/T systems at Concordia University.

1.3 OBJECTIVES

The objectives of this thesis are:

- 1) To study the velocity and the temperature fields experimentally using PIV and temperature measurements taken in an outdoor test facility.

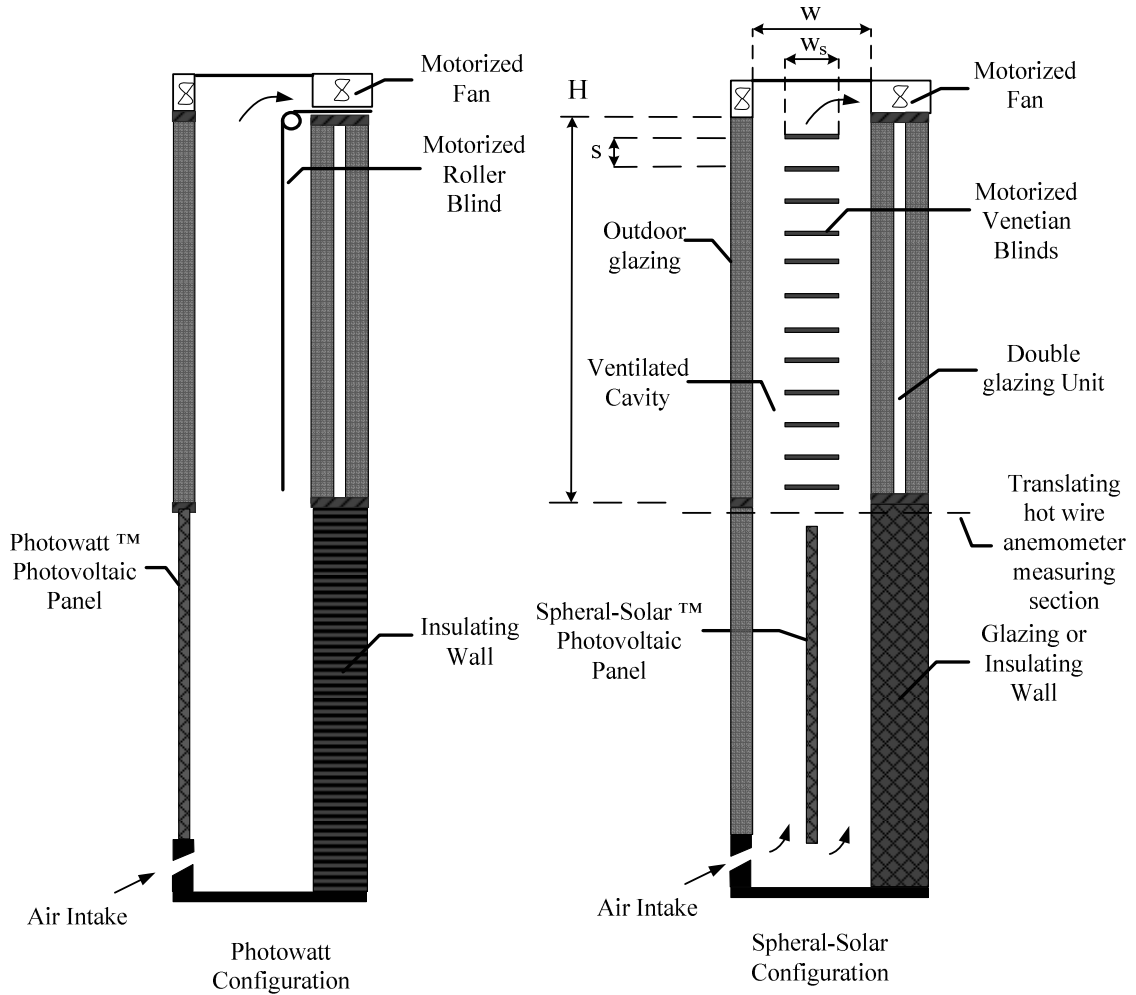


Figure 1.3: Schematic of the two BIPV/T setups at Concorida University: Photowatt™ on the left and Spheral-Solar™ on the right.

- 2) To develop a combined analytical solar-optical and CFD numerical model to predict the fluid flow and the thermal dynamics of the BIPV/T.
- 3) To develop a simplified 1-D empirical model to predict the layer temperature and the heat transfer coefficients. The long-wave radiation exchange can be modelled inside the channel and across the spatially non-uniform venetian blind layer. The 1-D model can be used to perform quick energy balance calculations.
- 4) To calculate average glazing and shading layer Convective Heat Transfer Coefficients (CHTCs) for various blind slat angles and air flow rates. Once calculated and validated for a broad range of blind slat angles and air flow rates the CHTCs can be easily incorporated into building energy simulation software to optimize the performance of BIPV/Ts.

1.4 THESIS LAYOUT

Chapter 2 presents common methods to analyze BIPV/T systems. Chapter 3 presents the upper section of the Spherical-Solar™ BIPV/T configuration and the specific numerical models developed to study its fluid dynamic and thermal characteristics. Chapter 4 presents the experimental equipment, procedure, and validation. Chapter 5 presents the empirical model and the average CHTCs. Finally Chapter 6 presents a summary of the results.

CHAPTER 2

PREVIOUS STUDIES OF BUILDING-INTEGRATED PHOTOVOLTAICS/THERMAL SYSTEMS

The main goal in the analysis of a ventilated window, from the point of view of a building designer, is to predict the heat transfer (and fluid flow) through the system. Analysis of a ventilated window usually comprises of a spectral optical and a CFD model, comparing simulation results with experimental measurements made in outdoor test facilities (Balocco and Colombari, 2006).

Heat transfer in a mechanically ventilated BIPV/T system is mainly governed by convection and long-wave radiation. The flow in such a system is essentially a low-speed channel flow, between two parallel plates, with or without flow obstructions such as shading devices, where the plates or the obstructions may be heated or cooled. The physics of flow in any mechanically ventilated BIPV/T system are identical to indoor ventilation applications, and many flow modelling assumptions and procedures in indoor air flow simulations apply to BIPV/Ts (Chen, 1995, and Posner et al., 2003).

The flow can be driven by buoyancy and/or wind effects, or it can be mechanically driven using an external ventilation fan. While some use laminar flow models (Mootz

and Bezia, 1996, and Brinkworth, 2002), turbulent models are recommended (Safer et al., 2005, Moshfegh and Sandberg, 1996, and Zollner et al., 2002). In mechanically ventilated systems, because of relatively high air flow speeds in comparison with naturally ventilated systems, the use of turbulent models is usually justified over the laminar models. Turbulent models may be preferred over the laminar models in naturally ventilated systems also, because the buoyancy driven flows can be quite turbulent. Given a mechanically-ventilated window with integrated venetian blinds, it is not clear if the flow will be driven primarily by forced or natural convection forces. Also, it is not clear if the flow will be laminar, turbulent, or exist in both regimes at different locations in the system. Both natural and forced convection (mixed convection) must be considered.

It is not clear if long-wave radiation must be taken into account in the analysis of BIPV/Ts. The long-wave radiation exchange is usually modelled (Ismail et al., 2006, Brinkworth, 2002, and Manz, 2004) but sometimes not (Ye et al., 1999). Because highly irradiated surfaces may get very hot (temperatures in excess of 60 °C are common) the long-wave radiation exchange can be quite comparable to the convective forces and must therefore be carefully modelled.

The numerical modelling of a BIPV/T system is a very complex task because of the presence of these coupled heat transfer mechanisms (Infield et al., 2004, and Salenes, 2002). Laminar and turbulent, and free or forced (or mixed) convection, and long-wave and short-wave radiation exchange may all be present. Therefore, a successful model

must be capable of successfully modelling all modes of heat transfer. Besides the complexities mentioned above, the numerical modelling of the system may be difficult because modelling local phenomena such as wind effects may be difficult.

2.1 SOLAR-OPTICAL STUDIES

When solar rays reach a window, a portion of the incident solar flux gets reflected from, transmitted through or absorbed by every glazing or shading layer. Solar-optical studies aim to track the solar flux inside a window, and calculate precisely the portion reflected, transmitted or absorbed by every layer.

2.1.1 Glazing Layers

There exist several methods to analyze the solar-optical properties of parallel planar glazing arrangements, such as ray tracing methods. The simplest and most computationally effective method was based on a recursive summation of multiple reflections and transmissions. If front and the back reflectivities (and transmissivities) of each glazing layer were assumed to be equal, the solar optical analysis of the glazing arrays would result in a recursive summation of multiple internal reflections and transmissions (Edwards, 1977). This recursive analysis was computationally inexpensive (hand calculations can be made for small number of layers) and yet very powerful. It can be applied to any number of glazing layers. Assuming that only beam reflection and transmission occurs from a beam radiation source (I_b) and only diffuse reflection and transmission occurs from a diffuse radiation source (I_d), then the recursive analysis can be used to track both beam and diffuse radiation individually.

Therefore, the following four parameters represent the effective solar-optical properties of the glazing layers: the beam-to-beam reflectivity and transmissivity (ρ_{bb} , τ_{bb}), and the diffuse-to-diffuse reflectivity and transmissivity (ρ_{dd} , τ_{dd}) (Figure 2.1).

$$\rho_{bb} = \frac{I_{b,ref.}}{I_b} \quad (2.10)$$

$$\tau_{bb} = \frac{I_{b,tra.}}{I_b} \quad (2.11)$$

$$\rho_{dd} = \frac{I_{d,ref.}}{I_d} \quad (2.12)$$

$$\tau_{dd} = \frac{I_{d,tra.}}{I_d} \quad (2.13)$$

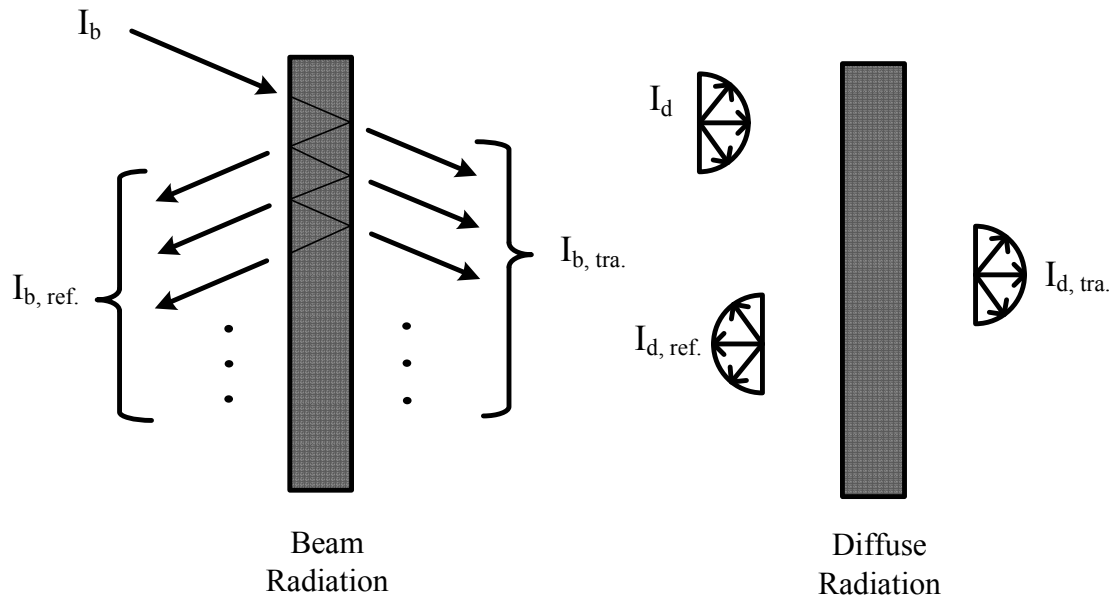


Figure 2.1: Recursive summation of multiple transmissions and reflections (Edward's, 1977).

The solar-optical analysis of a venetian blind layer is more complex than a glazing layer due to its non-uniformity (openness). Upon the interaction of solar rays with the slat surfaces a complex split of specular and diffuse reflections may occur. Therefore, to analyze the venetian blinds in great detail, a set of bi-directional reflectivity properties must be defined. To accurately model daylighting, for example, a bi-directional phase function can be defined to find the location in the room where most daylighting is reflected toward.

Due to the complexity of bi-directional phase functions a simpler approach can be sought. The recursive analysis of glazing layers (Edwards (1977)) can actually be modified to include a venetian blind layer. Allowing unequal front and back properties, beam-to-beam, beam-to-diffuse, and diffuse-to-diffuse reflectivities and transmissivities can be defined for each glazing and shading layer. For the venetian blind layer its spatially averaged (effective) properties can be used in place of the otherwise front-and-back-equal glazing properties. Once the effective properties of each layer and also the incoming beam and diffuse fluxes are known, a set of linear algebraic equations can be solved to give the absorbed fluxes in each layer (Wright and Kotey, 2006).

2.1.2 Venetian Blinds

Assuming that only beam-to-diffuse and diffuse-to-diffuse reflections occur from the blind slat surfaces a four surface or a six surface enclosure can be formed by the blind slats on top and bottom and openings connecting the tips of the slats on right and left (Figure 2.2). By applying a grey diffuse enclosure analysis to this enclosure the

spatially-averaged (effective) beam-to-beam, beam-to-diffuse and diffuse-to-diffuse transmissivity and reflectivity (τ_{bb} , τ_{bd} , τ_{dd} , ρ_{bb} , ρ_{bd} , and ρ_{dd}) of the shading layer can be calculated (Kotey and Wright, 2006). A k-surface grey diffuse enclosure analysis solves for surface radiosities, J_k , based on surface incident radiation, G_k , geometry and surface radiation properties. The venetian blind layer spatially-averaged (effective) properties depend on the blind slat reflectivity, spacings, blind slat angle, ϕ , and the profile angle, Ω .

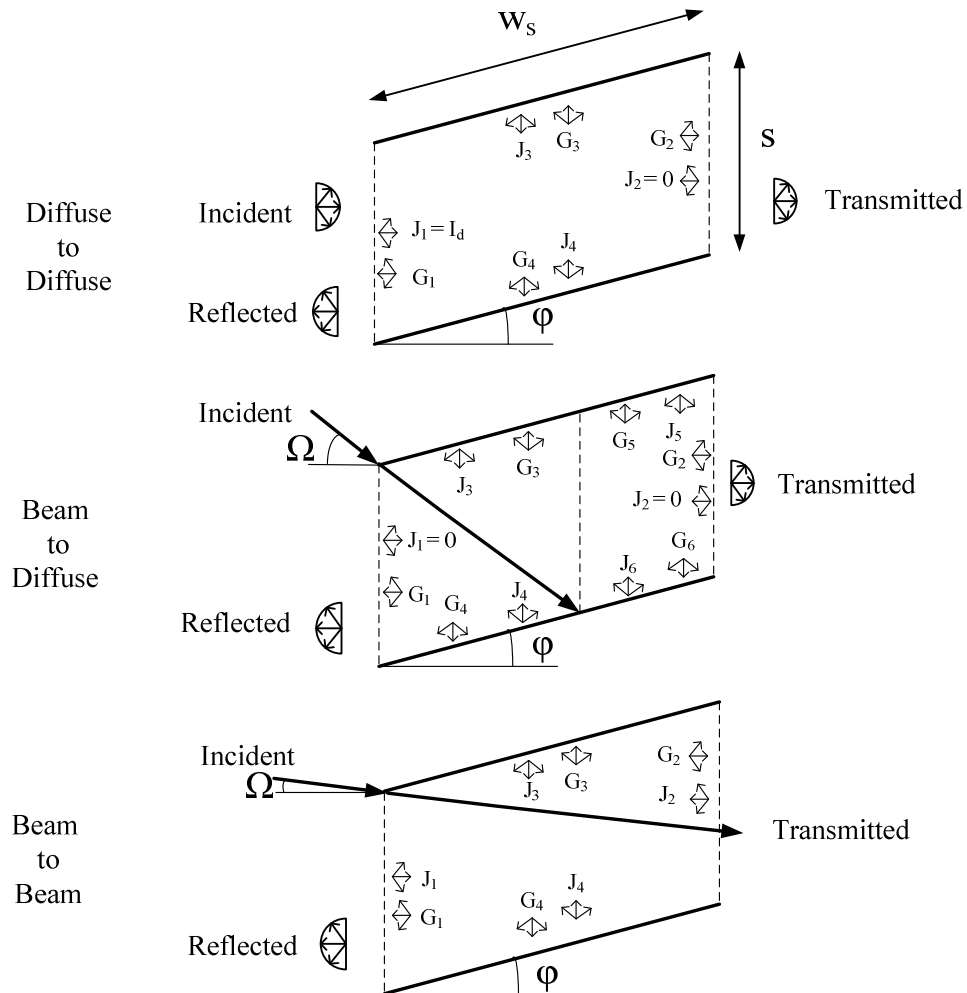


Figure 2.2: The four surface and the six surface enclosures used to determine the beam-to-beam, beam-to-diffuse, and diffuse-to-diffuse venetian blinds effective properties

2.2 THERMAL AND FLUID DYNAMIC STUDIES

A conventional steady-state U- and g-value (thermal transmittance and solar heat gain) window thermal analysis cannot be used in BIPV/Ts because it does not take into account the enthalpy change of the air inside the channel. In other words, heat transfer occurs not only in the horizontal direction (across the window), but also in the vertical direction (with the air). A modified U- and g-value approach however, can be used in BIPV/Ts (Infield et al., 2004) (Figure 2.3). In the modified approach, four U- and g-values are defined to not only take into account the center-window transmission but also to take into account enthalpy transfer to the channel air: U_{trans} represents the thermal transmission heat loss from the room (Temperature T_{int}) to the outdoor ambient (Temperature T_{ext}), U_{vent} represents the thermal transmission heat loss from interior to channel air, g_{trans} represents the solar transmission gain across the window, and g_{vent} represents the solar heat gain to channel air. The heat transfer rates to the room across the window and to the air are

$$Q_{trans} = g_{trans} I_{tot} - U_{trans} (T_{int} - T_{ext}) \quad (2.1)$$

$$Q_{vent} = g_{vent} I_{tot} - U_{vent} (T_{int} - T_{inlet}) \quad (2.2)$$

Two-dimensional control-volume based models, where every glazing, shading and air layer is divided into a number of control volumes, can be used to study ventilated windows. Balocco (2002) solved for the surface and air temperatures at each step Δy of the channel height of a ventilated facade. He used a finite element code, with an iterative procedure, to solve an energy balance equation in every control volume. His results showed that it was possible to achieve a sensible summer-time cooling effect

(associated with the decrease in dry bulb temperature, not the humidity ratio) when the air channel width was wider than 7 cm. A reduction of 27.5% in summer over-heating can be achieved for a channel width of 35 cm, whereas only 7% can be achieved for a channel width of 7 cm. For channel widths wider than 10–15 cm the cooling effect became more stable.

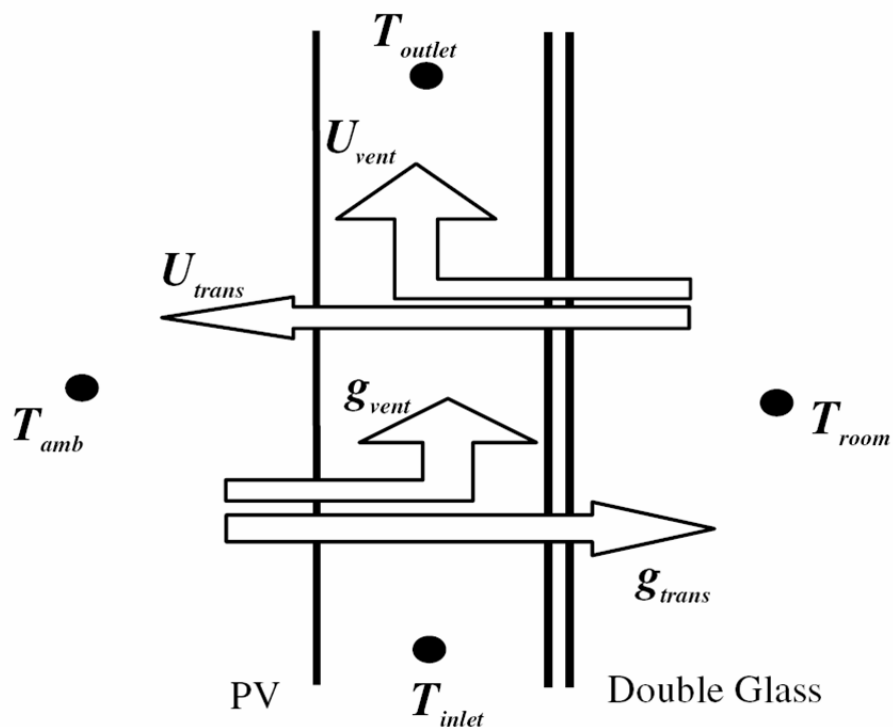


Figure 2.3: U- and g-value analysis (reproduced from Infield et al., 2004).

Ismail and Henriquez (2006) also used a control-volume based approach to study the thermal interactions inside a mechanically ventilated glass window consisting of two glass sheets and an air gap in between (Figure 2.4). The glass sheets and the air gap were divided into small control volumes and an energy balance can be performed at

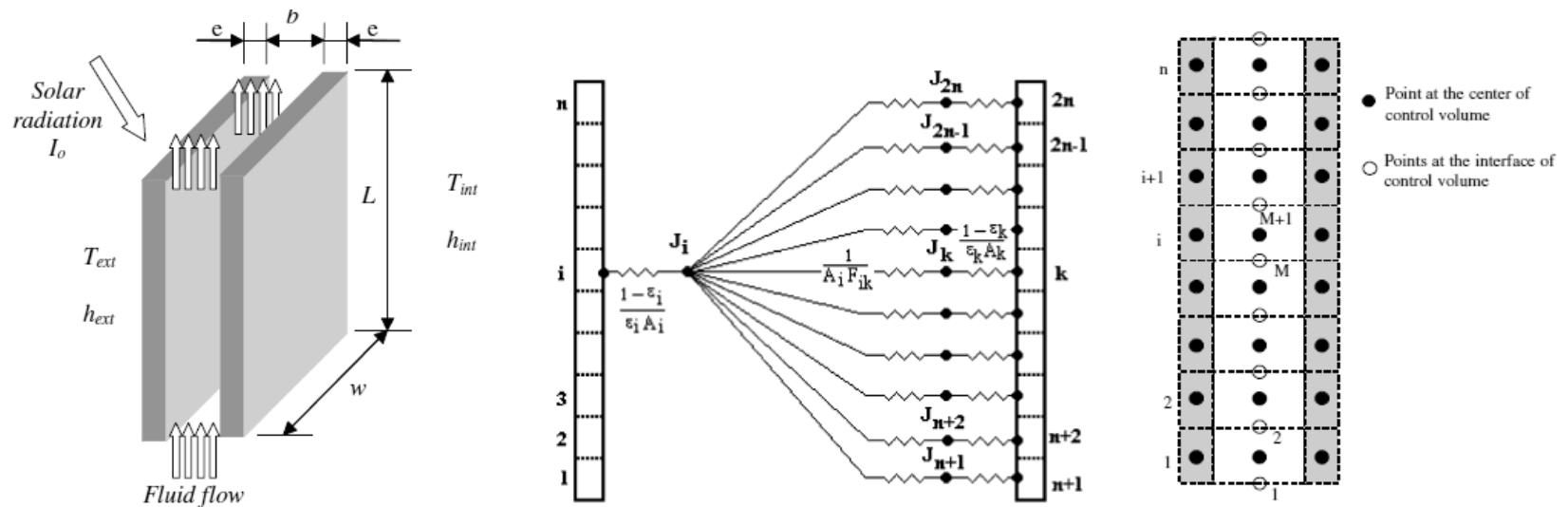


Figure 2.4: Air flow in a transparent ventilated channel and the long-wave radiation exchange between the control volumes (reproduced from Ismail, 2006).

every control volume. Variations of both boundary conditions on either side of the glazing and the incident radiation levels can be implemented. The view factors and the long-wave radiation exchange can be solved between every two arbitrary vertical parallel rectangular plates. The effect of mass flow rate, spacing between the glass sheets, and inlet temperature on the heat gain and the shading coefficients can be studied.

Non-dimensional analysis can be applied to study energy performance of ventilated windows. Bolocco and Colombari (2006) performed a non-dimensional analysis of a double glazed facade with a between-the-panes shading layer. Non-dimensional analysis can be used to help understand how a complex thermodynamic system operates but its utilization in window analysis is not so widespread. The reason it is not widely applied to window analysis is perhaps because of the complexity in the derivation and correlation of the non-dimensional parameters, especially that they have to be specific to a given geometry. Thermo-physical analysis of the system results in 16 dimensional variables that describe the heat transfer inside the channel. So the heat flux, \dot{q}'' , for example, can be a function of 15 parameters:

$$\dot{q}'' = (k_{ext}, D_h, \Delta T, I_{tot}, \rho_a, \mu_{ext}, \mu_a, R_{w1}, R_{w2}, \varepsilon_s, \dot{m}, \Delta P, c_p, H, T_a)$$

where

\dot{q}'' Heat transfer to the channel (W/m²)

k_{ext} External air thermal conductivity (W/m-K)

D_h Hydraulic Diameter (m)

ΔT	Temperature difference between internal and external air (°C)
I_{tot}	Total incident solar radiation (W/m ²)
ρ_a	Air density inside channel (kg/m ³)
μ_{ext}	External air viscosity (Pa-s)
μ_a	Air viscosity inside channel (Pa-s)
R_{w1}	Internal glass thermal resistance (m ² -K/W)
R_{w2}	External glass thermal resistance (m ² -K/W)
ε_s	Roughness
\dot{m}	Mass flow rate (kg/s)
ΔP	Inlet-to-outlet pressure difference (Pa)
c_p	Specific heat of air (J/Kg-K)
H	Height of channel (m)
T_a	Air temperature inside channel (°C)

Buckingham π theorem application results in 12 independent non-dimensional groups based on the 16 parameters listed above. These independent groups are

$$N1^* = \frac{\dot{q}'' D_h}{k_{ext} \Delta T} = Nu \qquad N7^* = \frac{H}{D_h} = \text{aspect ratio}$$

$$N2^* = \frac{\dot{m} c_p}{k_{ext} D_h} = Re Pr = Pe \qquad N8^* = \frac{k_{ext} \Delta T}{D_h I_{tot}}$$

$$N3^* = \frac{\dot{m}}{\mu_{ext} D_h} = Re \qquad N9^* = \frac{\varepsilon_s}{D_h} = \text{relative roughness}$$

$$N4^* = \frac{\dot{m}}{\mu_a D_h} = Re \qquad N10^* = \frac{k_{ext} R_{w1}}{D_h}$$

$$N5^* = \frac{\dot{m} k_{ext} \Delta T}{\Delta P^2 D_h^3}$$

$$N11^* = \frac{k_{ext} R_{w2}}{D_h}$$

$$N6^* = \frac{k_{ext} D_h^5 \Delta T \rho_a^2}{\dot{m}^3}$$

$$N12^* = \frac{\Delta T}{T_a}$$

Combining some of the above groups results in some groups with familiar physical phenomena. For example combining Nusselt number, Nu , with Peclet Number, Pe , Stanton number, St , can be derived. Similarly, friction factor, f , can be derived.

$$N1 = \frac{\dot{q}'' D_h}{k_{ext} \Delta T} = Nu$$

$$N7 = \frac{H}{D_h} = \text{aspect ratio}$$

$$N2 = \frac{\dot{m} c_p}{k_{ext} D_h} = Re Pr = Pe$$

$$N8 = \frac{k_a \Delta T}{D_h I_{tot}}$$

$$N3 = \frac{N1^*}{N2^*} = \frac{\dot{q}'' D_h^2}{\dot{m} c_p \Delta T} = St$$

$$N9 = \frac{\varepsilon_s}{D_h} = \text{relative roughness}$$

$$N4 = \frac{\dot{m}}{\mu_a D_h} = Re$$

$$N10 = \frac{k_a R_{w1}}{D_h}$$

$$N5 = \frac{\dot{m} k_a \Delta T}{\Delta P^2 D_h^3}$$

$$N11 = \left(\frac{N6^*}{N5^*} \right)^{1/2} \times \frac{1}{N7^*} = \frac{D_h^5 \rho_a \Delta P}{\dot{m}^2 H} = \text{friction factor, } f$$

$$N6 = \frac{k_a D_h^5 \Delta T \rho_a^2}{\dot{m}^3}$$

$$N12 = \frac{\Delta T}{T_a}$$

It is desirable to find a correlation using these new groups instead of the previous ones because some of these groups now have physical meanings. These 16 non-dimensional groups were calculated from experimental data, and a correlation of the following form was proposed:

$$N1 = a \times N2^b \times N3^c \times N4^d \times N5^e \times N6^f \times N7^g \times N8^h \times N9^i \times N10^m \times N11^n \times N12^p \quad (2.3)$$

The coefficient a and exponents b to p were calculated and the errors associated with them were also calculated. The validity of the correlation was confirmed because the average error on the multivariable correlation evaluated by χ^2 expression was 0.1181. It appears however that when investigating a correlation of type Equation 2.3 based on the new non-dimensional groups (N1, N2 ... N12), the uniqueness of the exponents is really in question. The new non-dimensional groups have some interdependency and the exponents of some of these groups (St and f) really depend on other exponents. For example, when writing $N3 = \frac{N1}{N2}$, the exponent c must depend on other exponents.

Therefore, although the correlation has been validated using experimental data, its uniqueness is really in question.

The range of applicability of the correlation based on Re , St , and f is very wide and covers all scenarios that may be encountered in experiment:

$$1.35 \times 10^5 < Re < 4.21 \times 10^5$$

$$3.98 < St < 64.86$$

$$0.11 < f < 0.45$$

Transient models can be used to study BIPV/T systems. Mei et al. (2003) developed a transient model in the computer program TRNSYS (A TRaNsient SYstems Simulation

program) (TRNSYS, 2005) and validated for a BIPV/T system consisting of a PV facade on the outdoor side, directly facing the sun, and a double glazing unit on the indoor side (Mei et al., 2003). The BIPV/T system in that study was 6.5 m high and was located in the Mataro library near Barcelona, Spain (Figure 2.5). The air flow rates inside the BIPV/T attributed to buoyancy effects were limited, and therefore, forced

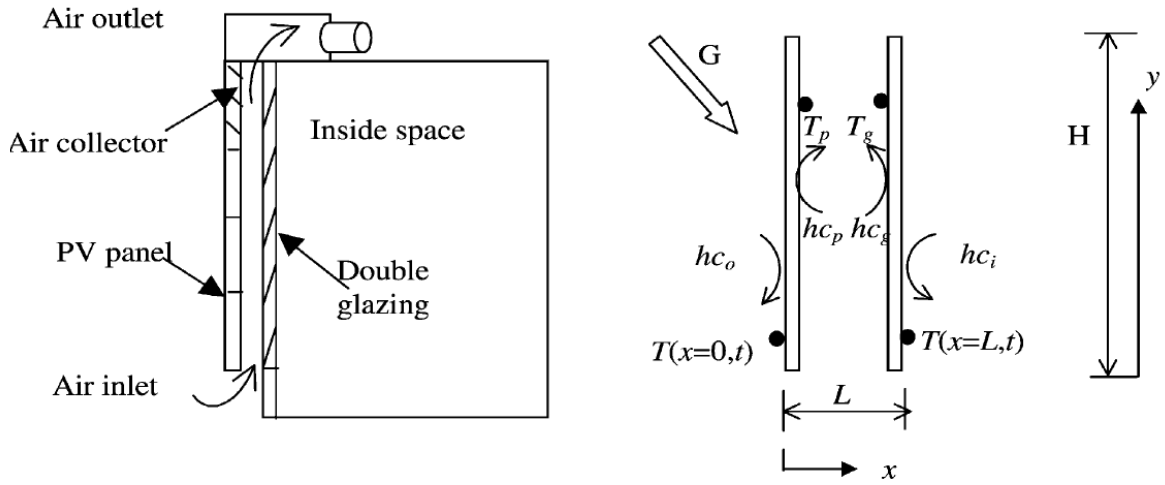


Figure 2.5: A BIPV/T system consisting of a PV panel and a double glazing unit (reproduced from Mei, 2005).

ventilation was utilized. The long-wave radiation exchange was modelled assuming isothermal surfaces. The Nusselt number, Nu , was estimated from a combination of laminar, Nu_l , and turbulent Nusselt number, Nu_t , correlations:

$$Nu = (Nu_l^2 + Nu_t^2)^{1/2} \quad (2.4)$$

$$Nu_l = 0.644\sqrt{Re}\sqrt[3]{Pr} \quad (2.5)$$

$$Nu_t = \frac{0.037 Re^{0.8} Pr}{1 + 2.444 Re^{-0.1} (Pr^{2/3} - 1)} \quad (2.6)$$

$$Re = \sqrt{Re_{force}^2 d + Re_{H, free}^2} \quad (2.7)$$

$$\text{Re}_{forced} = \frac{VH}{\nu}, \text{Re}_{free} = \sqrt{\frac{Gr_H}{2.5}} \quad (2.8)$$

where

Nu Nusselt number

Nu_l Laminar Nusselt number

Nu_t Turbulent Nusselt nNumber

Re Reynolds' number

Re_{forced} Forced convection Nusset number

Re_{free} Free convection Nusselt number

Pr Prandlt number

Gr Grashof Number

The facade outlet temperature reached around 50°C in summer and 40°C in winter. Both heating and cooling conditions were considered. It was observed that the presence of a PV panel in the facade contributes marginally to higher cooling loads (about 10% in Barcelona and 14% in Stuttgart) whereas the savings in heating loads can be rather significant, but still very location dependent. In Barcelona, due to hotter climates, the savings in heating loads were 13% (14600 kWh per year), but in Stuttgart they were only about 3.5% (11200 kWh per year).

Knowledge of the air flow rate is essential in numerical modelling of naturally-ventilated facades. Gratia and De Herde (2004) studied the impact of local and ambient conditions on the performance of a 5-storey high, naturally-ventilated, double skin

facade (Figure 2.6). That study attempted to model the air flow rate, Q_v , due to buoyancy effects in terms of the available area for the opening, A , the height between the openings, H , the temperature difference between the indoor and outdoor air, ΔT , and the outdoor air T_e (Gratia and De Herde, 2004):

$$Q_v = C_d \times A \times \sqrt{g \times H \times \Delta T / T_e} \quad (2.9)$$

where

C_d A model constant

g gravitational acceleration, m/s^2

The pressure distribution around a building caused by the wind may change and the airflow rate due to wind effects can be modelled as follows:

$$Q_v = C_d \times A \times \sqrt{\Delta C_p \times v^2 / 2} \quad (2.10)$$

where

ΔC_p coefficient of pressure difference

v wind speed at top of the building

The direction of air flow can change due to the combined effects of buoyancy and pressure. During the night, the buoyancy effect (stack effect or chimney effect) is nearly non-existent and wind pressure effects can dominate. The direction of flow may be from top to bottom depending on time and location. For a northern-facing facade orientation considered in Gratia and De Herde (2004) the direction of flow tends to be from top to bottom at night time. In another study of naturally ventilated facades,

upward flow was noticed 90% of time in summer and 73% of time in winter (Saelens, 2002).

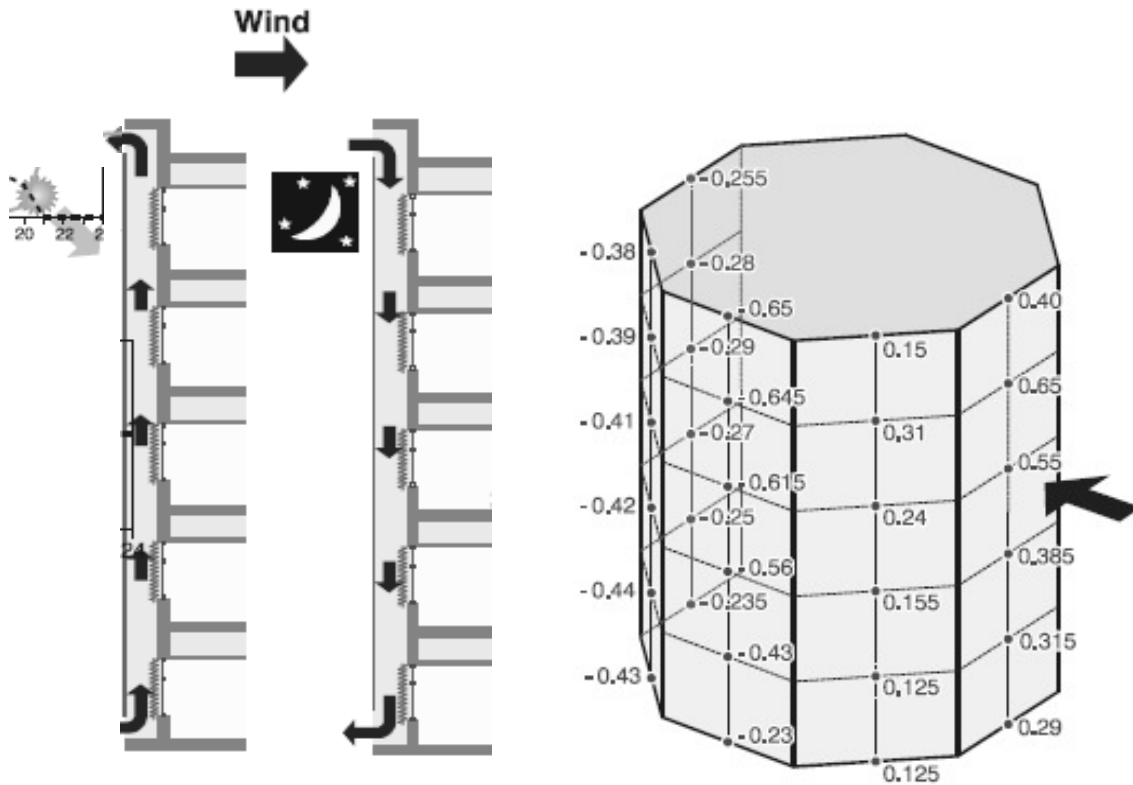


Figure 2.6: Schematic of a double facade, the direction of air flow for a south-oriented facade with a south wind, and an example of wind pressure coefficients on a building (reproduced from Gratia and De Herde, 2004).

2.2.1 Vertical Walls

The “flat plate flow approximation” is sometimes applicable to vertical walls in BIPV/Ts; i.e., glazing or PV walls. Thus, if the spacings are large, the flow can be treated as having separate flow regimes, and the flow near the glazing boundaries can be modelled as flow over a flat plate (Figure 2.7). A number of studies justify the

applicability of the flat plate approximation, but much disagreement exists as to what gap width is sufficient to justify the applicability of the flat plate approximation. Despite slightly different boundary conditions in different studies, the range of gap widths is large. For a 2.5-m one-storey high facade, the use of the flat plate approximation is justified for gap widths of at least 14 cm (Mei et al., 2003), 30 cm (Rodriguez et al., 2000), and 60 cm (Zollner et al., 2002).

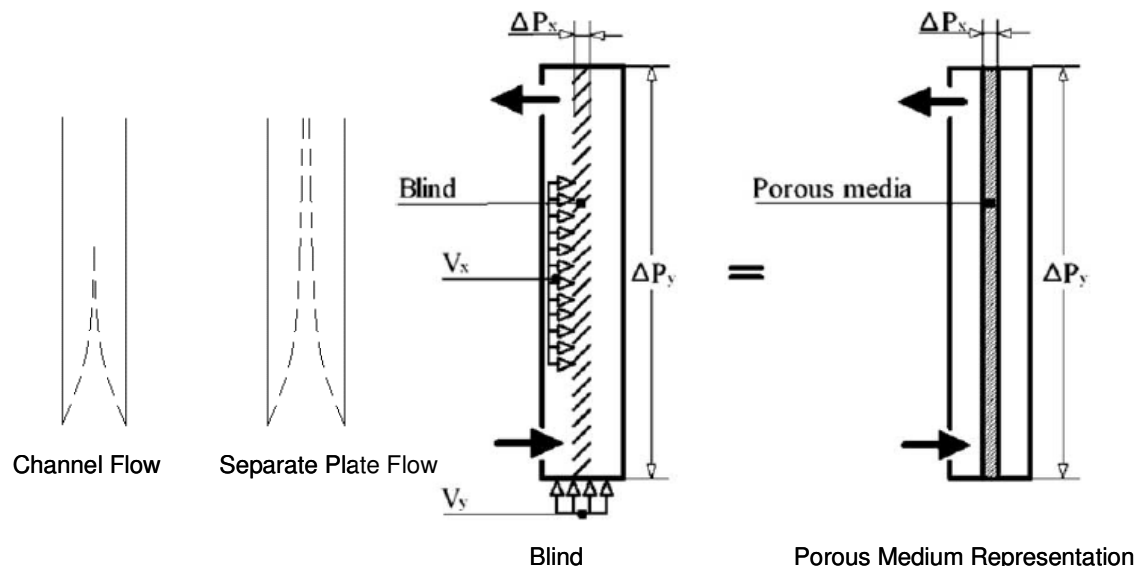


Figure 2.7: Flat plate approximations for vertical walls. Porous medium representation for venetian blinds (reproduced from Safer et al., 2005).

2.2.2 Venetian Blinds

Venetian blinds placed next to a glazing layer, on the indoor side, were studied by Ye et al. (1999). The influence of blind-to-glass spacing and slat tilt angle on the flow pattern and the heat transfer around venetian blinds was studied. The blind tilt angle can have a significant impact on the heat transfer coefficients in a naturally ventilated system unless the blind-to-plate spacing is sufficiently wide.

Venetian blinds placed between the panes of a sealed double glazing unit were extensively studied by Ye et al. (1999), Garnet (1999), and Tasnim (2004). The U-value of the double-glazing with the venetian blind layer has been calculated and compared to that of a single glazing layer and of a conventional double glazing unit.

Forced flow around between-the-panes venetian blind slats was modelled numerically (Safer et al., 2005). For a specific geometry and for summer-time outdoor conditions, the optimum location for the placement of the blind layer was closer to the indoor glazing. When placed in this location, higher airflow rates (and higher heat transfer coefficients) can be induced near the outdoor glazing than the indoor glazing. Therefore, a higher fraction of the absorbed solar energy will be readily lost to the outdoor environment. Also, the blind slat angle had a negligible effect on the heat transfer through the window if placed closer to the indoor glazing. Therefore, a suitable blind slat angle can be chosen according to daylighting needs without affecting the heat transfer through the window.

Venetian blinds were numerically modelled as a porous medium representation to reduce the number of grid elements (Safer et al., 2005) (Figure 2.7). Porous medium pressure drop, in the X- and Y-direction, and other porosity parameters determine the effect of the porous medium on the velocity field and the amount of mass crossing through the blind, if any.

CHAPTER 3

NUMERICAL MODEL DEVELOPMENT

This chapter presents the development of models that are used to study the air flow in the BIPV/T system. The geometry, flow domain and numerical development are presented. In addition, solar-optical and long-wave material properties are presented. Numerical solar-optical and CFD models are developed at various blind slat angles to predict the basic fluid flow and heat transfer inside the BIPV/T. These models are essential to understanding how a complex fluid dynamic and thermal system works.

Detailed CFD modelling is the first step to analyze and optimize the performance of BIPV/Ts. To provide a detailed numerical study of the BIPV/T is beyond the scope of this thesis; however, the aim is to be able to roughly obtain the heat flux distribution and local and average heat transfer coefficients at various blind slat angles and various boundary conditions.

3.1 SOLAR-THERMAL SEPARATION

Numerical modeling of all solar-thermal systems is typically carried out using a solar-thermal separation technique. The solar absorption by each layer is first calculated in a sub-model, the results of which feed into a main CFD model. The solar absorption sub-model provides the main thermal CFD model with heat generation terms. The CFD model can determine the whole flow field at once; Therefore, neither the flat plate approximation nor the porous media representation need to be used. The CFD model accounts for long-wave and convective exchange, but not solar radiation exchange.

3.2 SOLAR-OPTICAL MODEL

The aim of the solar-optical analysis is to track beam and diffuse solar radiation, I_b and I_d respectively, through the glazing and shading layers. For glazing layers, the effective transmissivity and reflectivity that are used in the solar-optical analysis are the normal beam-to-beam transmissivity, τ_n , and the normal beam-to-beam reflectivity, ρ_n , in case of beam incidence radiation, and the diffuse-to-diffuse transmissivity, τ_d , and the diffuse-to-diffuse reflectivity, ρ_d , in case of diffuse incidence radiation. The glazing layers effective properties were introduced in Chapter 2. They were all taken from Hadlock (2006) and are presented in Table 3.1.

For the blind layer, the slat surface solar normal-hemispherical reflectivity is needed for the effective properties calculations. The definition of surface solar normal-hemispherical reflectivity can be found in Seigel and Howell (2002). It was measured to

be 0.58 using a CARY5000 spectrophotometer (Appendix 1). The blind layer effective beam-to-diffuse transmissivity and reflectivity (ρ_{bd} and τ_{bd}) and diffuse-to-diffuse transmissivity and reflectivity (ρ_{dd} and τ_{dd}) were calculated according to the procedure described by Kotey and Wright (2006) and outlined in Chapter 2. The blind layer effective properties calculations are presented in Appendix 2 and the results are listed in Table 3.2 for three different blind slat angles.

After all layer effective properties were calculated (or previously given) the absorbed fluxes in each layer (heat generation terms) were calculated according to the analysis described by Wright and Kotey (2006) and outlined in Chapter 2. The absorbed fluxes calculations are presented in Appendix 3 and the results are listed in Table 3.2. The measurement scenarios referred to in Table 3.2 and 3.3 will be described later in Chapter 4. In Tables 3.1 and 3.2, the profile angles, Ω , calculated from standard formulae, were always approximately 45°. The calculation of solar angles and the absorbed fluxes are given in Appendix 2.

Table 3.1: Solar-optical glazing effective and blind surface properties

	τ_n	ρ_n	τ_d	ρ_d
Clear glass 5mm	0.79	0.066	0.705	0.125
Clear glass 3mm	0.84	0.07	0.76	0.13
Low-e glass	0.7	0.12	0.63	0.18
Blind surface	0	0.58		

Table 3.2: Venetian blind spatially-averaged (effective) properties

Scenarios	φ	Ω	τ_{bb}	ρ_{bb}	τ_{bd}	ρ_{bd}	τ_{dd}	ρ_{dd}
1–3	0	$\approx 45^\circ$	0	0	0.21	0.23	0.52	0.14
4–6	+ 45°	$\approx 45^\circ$	0	0	0.08	0.44	0.38	0.25
7–9	+ 75°	$\approx 45^\circ$	0	0	0.02	0.55	0.14	0.44

Table 3.3: Absorbed fluxes in each layer

Scenarios	φ	Ω	Incident I_b [W/m ²]	Incident I_d [W/m ²]	Abs. Inner Clear [W/m ²]	Abs. Inner Low-e [W/m ²]	Abs. Blind Layer [W/m ²]	Abs. Outer Layer [W/m ²]
1–3	0	$\approx 45^\circ$	630.7	49.3	19.8	16.8	307.5	123.1
4–6	+ 45°	$\approx 45^\circ$	600.0	46.9	15.1	12.8	255.4	130.1
7–9	+ 75°	$\approx 45^\circ$	634.0	49.6	1.2	1.1	244.5	157.7

3.3 CFD MODEL DEVELOPMENT

The governing equations for the transport of mass, momentum and energy are

The continuity equation:

$$\frac{\partial}{\partial x}(\rho u) + \frac{\partial}{\partial y}(\rho v) = 0 \quad (3.1)$$

The X-momentum transport equation:

$$\frac{\partial}{\partial x}(\rho uu) + \frac{\partial}{\partial y}(\rho uv) = -\frac{\partial P}{\partial x} + \frac{\partial}{\partial x}((\mu + \mu_t)\frac{\partial u}{\partial x}) + \frac{\partial}{\partial y}((\mu + \mu_t)\frac{\partial u}{\partial y}) \quad (3.2)$$

The Y-momentum transport equation:

$$\frac{\partial}{\partial x}(\rho v v) + \frac{\partial}{\partial y}(\rho u v) = -\frac{\partial P}{\partial y} + \rho g \beta (T - T_{ref}) + \frac{\partial}{\partial x}((\mu + \mu_t) \frac{\partial v}{\partial x}) + \frac{\partial}{\partial y}((\mu + \mu_t) \frac{\partial v}{\partial y}) \quad (3.3)$$

The energy transport equation:

$$\frac{\partial}{\partial x}(\rho u T) + \frac{\partial}{\partial y}(\rho v T) = \frac{\partial}{\partial x} \left(\frac{K + K_t}{c_p} \frac{\partial T}{\partial x} \right) + \frac{\partial}{\partial y} \left(\frac{K + K_t}{c_p} \frac{\partial T}{\partial y} \right) \quad (3.4)$$

where

- x, y Axis directions, m
- u, v Time-averaged velocity in the x and y direction, m/s
- P Dynamic pressure, pressure in excess of hydrostatic pressure, Pa
- μ Viscosity, kg/ms
- ν Kinematic viscosity, m/s
- ρ Density, kg/m³
- T Temperature, K
- β coefficient of thermal expansion, 1/K
- K Thermal conductivity, W/m-K
- K Turbulent thermal conductivity, W/m-K
- c_p Specific Heat, J/Kg

The CFD model was developed in the commercial package ANSYS FLUENT 6.3 (FLUENT, 2005). While FLUENT allows solar tracking options and solar absorption

calculations, the solar-thermal separation technique is much more versatile. FLUENT is control-volume based and discretizes the flow domain into small control volumes via the process of meshing. The governing equations for mass, momentum, energy, and turbulence transport are solved at every control volume. The flow domain consists of both the ventilated and closed cavities, with all the surrounding glazing and shading walls. The set of partial differential equations is linearized, and the resulting matrix is solved iteratively (Gauss-Seidel) to give velocity, temperature and turbulence quantities at every control volume.

The SIMPLE algorithm was used to solve the pressure-velocity coupling (FLUENT, 2005). Governing equations for momentum, energy, turbulent kinetic energy, k , and turbulent dissipation rate, ϵ_k , were solved using a First Order Upwind scheme. The under-relaxation factors for pressure, momentum, k and ϵ_k were set to 0.3, 0.7, 0.8, and 0.8, respectively. The convergence criteria for scaled residuals were set to 10^{-4} for the momentum, k , and ϵ_k equations and 10^{-7} for the energy equation. The conservation equation for a general variable φ at control volume P can be written as

$$a_p \varphi_p = \sum_{nb} a_{nb} \varphi_{nb} + b \quad (3.5)$$

Here a_p is the center control volume coefficient, a_{nb} are the influence coefficients for the neighboring control volumes, and b is a contribution of the source term. The residual, R_φ , is defined as the imbalance in equation 3.5, summed over all control volumes in the computational domain:

$$R_\varphi = \sum \left| \sum_{nb} a_{nb} \varphi_{nb} + b - a_p \varphi_p \right| \quad (3.6)$$

The scaled residual, \bar{R}_φ , is defined as

$$\bar{R}_\varphi = \frac{\sum \left| \sum_{nb} a_{nb} \varphi_{nb} + b - a_p \varphi_p \right|}{\sum |a_p \varphi_p|} \quad (3.7)$$

FLUENT (2005) claims that for most flows and most solvers it is sufficient to set the convergence criteria for scaled residuals to 10^{-3} for all equations and 10^{-6} for the energy equation. To ensure convergence, the criteria were set to one order of magnitude lower than the suggested values. FLUENT further recommends that some real physical parameters such as drag coefficient or heat transfer coefficient be monitored to ensure convergence. After convergence was achieved, any subsequent iteration resulted in a change in blind area-averaged surface temperature of less than 0.02 °C.

3.3.1 Model Geometry

The flow domain consists of the upper (shading and vision) section of the Spherical-Solar BIPV/T (Figure 3.1). The flow is modelled as two-dimensional. Three-dimensional effects were neglected. Three slat angles, 0, 45, and 75°, were considered. A unique mesh was developed at every slat angle. These angles were chosen because they cover a range from open to almost closed blind positions. The experimental measurements described in the subsequent chapter were also made at these slat angles. The channel

width, glazing thicknesses, venetian blind slat width, slat thickness, slat spacing, slat radius of curvature, and slat angles were as follows:

w	Channel Width, 92 mm
t_{gi}	Indoor glazing thickness, indoor-pane, 3 mm
t_{gii}	Low-e glazing thickness, 3 mm
t_{go}	Outdoor glazing thickness, 5 mm
w_s	slat width, 49 mm
t_s	slat thickness, 0 (slat thickness ignored)
s	slat spacing, 43.9 mm
r_s	slat radius of curvature, 0 (slat curvature ignored)
φ	slat angle, 0, 45, and 75°.

3.3.2 Boundary Conditions

The boundary conditions include inlet, outlet, blind slat walls, insulated walls, closed cavity walls and channel walls (Table 3.4) (Figure 3.1). No-slip conditions are applied to all walls ($u = 0$, $v = 0$). The glazings were insulated at the ends ($\partial T / \partial y = 0$). The indoor convective heat transfer coefficient is calculated based on the temperature difference between the interior and the inner-most pane, ΔT , and the height of the glazing, H (ASHRAE, 2005). The indoor convective heat transfer coefficient varied from about 2 to 3 W/m²K:

$$h_{c,in} = 1.46[\Delta T / H]^{0.25} \quad (3.8)$$

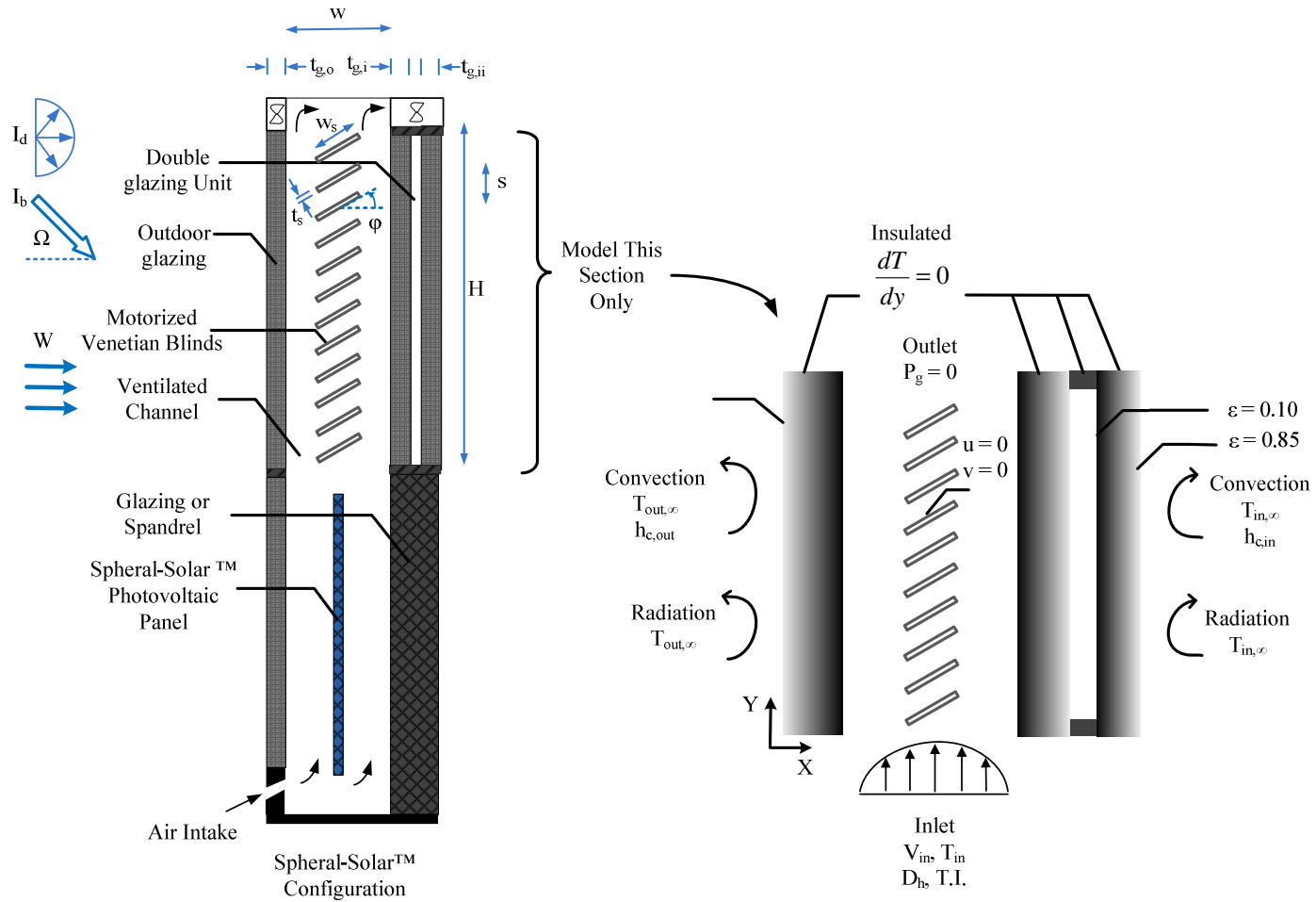


Figure 3.1: Flow domain geometry and boundary conditions.

The outdoor convective heat transfer coefficient ranges from 5 to 7.4 W/m²K and is calculated based on the outdoor wind speed, W , and the cubic root of building volume, Z (Duffie and Beckman, 1991):

$$h_{c,out} = \max[5, 8.6W^{0.6} / Z^{0.4}] \quad (3.9)$$

The velocity and temperature profiles, V_{in} and T_{in} , hydraulic diameter D_h , and turbulent intensity, T.I., are specified at the inlet. V_{in} and T_{in} are based on experimental measurements. D_h is taken to be twice the width of the channel, w . The turbulent intensity is set equal to 10% always. The turbulent intensity is the root-mean-square of the fluctuations in velocity divided by the time-averaged velocity and depends totally on the upstream history of the flow. Generally, T.I. is between 1% and 10%. An empirical correlation exists for T.I. in the core of a fully-developed pipe flow. It depends on the Reynolds' number based on the hydraulic diameter, Re_{D_h} (FLUENT, 2005):

$$T.I. = 0.16(Re_{D_h})^{-1/8} \quad (3.10)$$

For the range of Reynolds' numbers encountered in this work (1400 to 6000), application of the above equation results in turbulent intensities ranging between 5% and 6%. However, turbulent intensities are expected to be higher because of the chaotic entrance region. The geometry of the entrance region, where air gets sucked into the system (just below the photovoltaic panel), is such that the flow turns sharply and experiences higher-than-usual turbulence levels (Liao, 2005). Therefore it is expected

that by the time the flow reaches the inlet (just below the blind layer) it retains high turbulence levels. Also, wind gusts create instability and are expected to contribute to high turbulence levels. For these reasons the T.I. was set to 10% consistently throughout this work.

The outlet is specified as having zero gauge pressure. Solid regions, i.e, the blind and the glazings, have specified volumetric heat generation terms. Air with constant properties at 20°C, except density, is assigned to fluid regions, i.e., the closed cavity and the channel. The Boussinesq approximation was used to account for the temperature variations of density (FLUENT, 2005).

3.3.3 Turbulence and Near Wall Modelling

The Reynolds' numbers, based on channel width, range from 1400 to 6000, according to the practical range of air flow velocities of about 0.1 to 0.6 m/s. The Grashof numbers, based on the channel width and the temperature difference between the blind slats and the glazings, range from 1.0 to 2.5×10^7 . The flow is driven most often by a mix of free and forced convection.

The flow is subject to separation (from the tip of the slats) and swirls because of the presence of the blind slats. The “realizable” $k-\epsilon_k$ model of Shih et al. (1995) was selected at all flow rates and blind slat angles. This $k-\epsilon_k$ model has been extensively validated for wall-bounded flows, rotating and separating flows, and flows over obstacles (Shih et al., 1995, Kim et al., 1999, and FLUENT, 2005). This $k-\epsilon_k$ model has

been previously employed for similar channel flows in BIPV/Ts at Reynolds' numbers, based on the hydraulic diameter, as low as even 1600 (Liao et al., 2007, and Safer et al., 2005).

Table 3.4: Summary of the boundary conditions.

Inlet	V_{in}	T_{in}	D_h	T.I.
Outlet	$P_g = 0$			
Walls	$u = 0$	$v = 0$		
Outdoor	$h_{c,out}$	T_{ext}	$\epsilon_{lw} = 0.84$	T_{ext}
Indoor	$h_{c,in}$	T_{int}	$\epsilon_{lw} = 0.84$	T_{int}
Insulated	$\dot{q}'' = 0$			
Solid Regions	\dot{g}			

As we will see in the subsequent chapter, the fluid between the blind slats has relatively low velocity. Therefore, laminar heat transfer may occur from the surface of the blind slats, except near the tips, even when the rest of the flow (in the regions bounded by the blind slats on one side and the glazing surfaces on the other side) may be mostly turbulent. In other words, laminar and turbulent heat transfer may co-exist in the channel. Furthermore, the flow is somewhat unsteady because the tip of the blind slats cause separation and vortex shedding. For these reasons a steady RANS-based (Reynolds Averaging Navier Stokes) model may not capture all features of the flow, but as we will see in the subsequent chapter, heat transfer is satisfactorily modelled inside the channel using a Shih's RANS-based $k-\epsilon_k$ model. Since most of the heat transfer occurs from the glazing surface and the tips of the blind slats (not the middle of the

blind slats where laminar heat transfer may occur) and since the CFD seems to predict the heat transfer satisfactorily in these regions the use of a steady RANS-based model is justified in this work. Unless a more sophisticated numerical scheme, such as Direct Numerical Simulation (DNS), is used a CFD simulation cannot capture unsteadiness and simultaneous laminar and turbulent heat transfer.

Shih's k- ϵ_k model has a revised dissipation rate equation and a revised eddy viscosity formulation over the standard k- ϵ_k model. Unlike the standard k- ϵ_k model the eddy viscosity model parameter, C_μ , is not constant (Shih et al., 1995, and FLUENT, 2005).

The eddy viscosity formulation and the k and ϵ_k transport equations are

The eddy viscosity formulation (Shih et al., 1995):

$$\mu_t = \rho C_\mu \frac{k^2}{\epsilon_k} \quad (3.11)$$

The turbulent kinetic energy transport equation (FLUENT, 2005):

$$\frac{\partial}{\partial t}(\rho k) + \frac{\partial}{\partial x_i}(\rho k u_j) = \frac{\partial}{\partial x_i} \left[\left(\mu + \frac{\mu_t}{\sigma_k} \right) \frac{\partial k}{\partial x_i} \right] + G_k + G_b - \rho \epsilon_k \quad (3.12)$$

The turbulent kinetic energy dissipation transport equation (FLUENT, 2005):

$$\begin{aligned} \frac{\partial}{\partial t}(\rho \epsilon_k) + \frac{\partial}{\partial x_j}(\rho \epsilon_k u_j) = & \frac{\partial}{\partial x_j} \left[\left(\mu + \frac{\mu_t}{\sigma_\epsilon} \right) \frac{\partial \epsilon_k}{\partial x_j} \right] + \rho C_1 S \epsilon_k \\ & - \rho C_2 \frac{\epsilon_k^2}{k + \sqrt{\nu \epsilon_k}} + C_{1\epsilon} \frac{\epsilon_k}{k} C_{3\epsilon} G_b \end{aligned} \quad (3.13)$$

$$C_1 = \max \left[0.43, \frac{\eta}{\eta + 5} \right], \eta = S \frac{k}{\epsilon_k} \quad (\text{FLUENT, 2005}) \quad (3.14)$$

$$S = \sqrt{2S_{ij}S_{ij}}, S_{ij} = \frac{1}{2}(U_{i,j} + U_{j,i}) \quad (\text{Shih, 1995}) \quad (3.15)$$

$$C_{1\varepsilon} = 1.44, C_2 = 1.9, \sigma_k = 1.0, \sigma_\varepsilon = 1.2 \quad (\text{FLUENT, 2005}) \quad (3.16)$$

where

μ_t	Turbulent viscosity, kg/ms
k	Turbulent kinetic energy, m^2/s^2
ε_k	Rate of dissipation of turbulent kinetic energy, m^2/s^3
$\eta, C_{\mu}, C_{1\varepsilon}, C_{3\varepsilon}$	Model parameters
S	Modulus of the mean rate of strain tensor, 1/s
$U_{i,j}$	Time-average mean velocity, m/s
G_k	Production of turbulent kinetic energy, kg/ms^3
G_b	Generation of turbulent kinetic energy due to buoyancy, kg/ms^3

A two-layer model is adopted treating the viscosity affected region and the core turbulent region individually. In FLUENT there are two wall treatment options available: the Standard Wall Function (SWF) and the Enhanced Wall Treatment (EWT). The SWF uses a pre-defined velocity profile (equilibrium turbulent boundary layer) to resolve the near-wall velocities. Because they are designed with specific (equilibrium) conditions in mind they tend to fail for flows involving separation and recirculation. The EWT resolves the velocity of fluid all the way to the wall and is suitable for low Re flows and flows with complex wall phenomena. In the near wall region the viscous sublayer is resolved using the EWT option and in the core flow region Shih's k and ε_k equations are applied. The EWT requires a much finer mesh near the walls. FLUENT

suggests that at least 10 control volume cells be placed in the viscosity affected region ($y^+ < 5$). The demarcation between the viscosity affected region and the core turbulence region is set by the Reynolds' number based on the distance from the wall ($Re_y = 200$):

$$Re_y = \frac{\rho\sqrt{k}y}{\mu} \quad (3.17)$$

3.3.4 Radiation Model

Long-wave radiation is solved between the glass and blind surfaces, including inside the double-glazing unit, using the FLUENT's Surface-to-Surface (S2S) grey-diffuse radiation model. The S2S model divides the radiating surfaces into small surfaces and treats air as a non-participating fluid. The outgoing and the incident flux on every element k , $q_{out,k}$ and $q_{in,k}$ (Equations 3.18–3.20), can be combined to form a system of equations based on surface radiosities, J_k (Equations 3.21–3.22):

$$q_{out,k} = \varepsilon_k \sigma T_k^4 + \rho_k q_{in,k} \quad (3.18)$$

$$q_{in,k} = \sum_{j=1}^N F_{k,j} q_{out,j} \quad (3.19)$$

$$q_{out,k} = \varepsilon_k \sigma T_k^4 + \rho_k \sum_{j=1}^N F_{k,j} q_{out,j} \quad (3.20)$$

$$J_k = E_k + \rho_k \sum_{j=1}^N F_{k,j} J_j \quad (3.21)$$

$$K_{[N \times N]} J_{[N \times 1]} = E_{[N \times 1]} \quad (3.22)$$

where

$F_{k,j}$ View factor

$E_{[N \times N]}$ Emissivity matrix

$K_{[N \times N]}$ Matrix of constants depending on surface properties and geometry

The long-wave hemispherical properties of all radiating surfaces are summarized in Table 3.5. The long-wave emissivity of soda lime glass is 0.84 (Hollands et al., 2001). The long-wave normal emissivity of the blind slat surface was measured to be 0.76 (Appendix 1). The hemispherical emissivity of the low- ϵ coating was previously provided by Hadlock (2006).

Table 3.5: Hemispherical long-wave emissivity and total reflectivity of surfaces.

	ϵ_{lw}	ρ_{lw}
Clear glazings	0.84	0.16
Low-e glazing	0.10	0.90
Blind slat	0.77	0.23

3.4 CFD BASIC FLUID DYNAMICAL VALIDATION

Before developing the CFD model of the BIPV/T system, a simple flow inside an AFW was considered to assess the capabilities of FLUENT in modelling fluid flow. A simulation of a forced channel flow with between-the-panes venetian blinds was performed and the results were compared with published numerical data. The geometry was very similar to the one in the BIPV/T. The flow was modelled as two-dimensional and steady. The channel was 200 mm wide and 3 m high. The blind slats were 77 mm

wide. The flow mean speed (mass flow rate divided by density and divided by the entire width of channel (200 mm)) was 0.05 m/s. The velocity field was considered only and the thermal effects were not. The details of the geometry and numerical procedure are outlined in Safer et al. (2005). Shih's $k-\epsilon_k$ turbulence model was selected to be consistent with Safer who also used that $k-\epsilon_k$ model. The streamwise velocity profile is compared, at a height of 2 m, between the simulation results of Safer and the simulation developed in this work (Figure 3.2). The software package FLUENT seems to predict the streamwise velocity remarkably consistently.

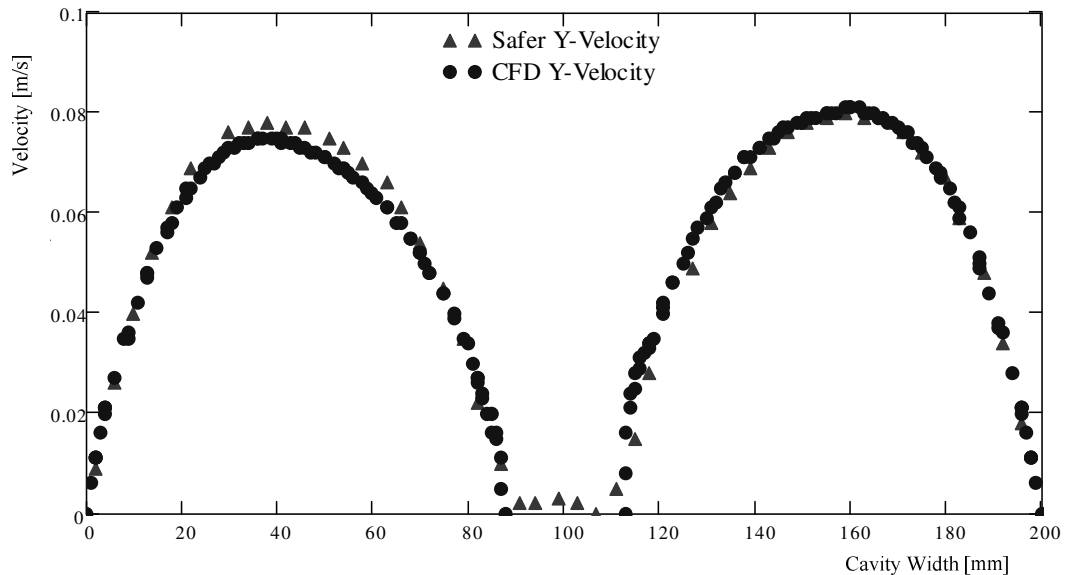


Figure 3.2: Streamwise velocity at a height of 2 m (adapted from Safer et al., 2005).

3.5 MESH GENERATION

Generating a mesh for the BIPV/T system is a difficult task because of the presence of very small (blind slats) and very large length scales. The glazing and blind surfaces were divided into small rectangular elements (about 2.0 mm in size) with decreasing

element size near the solid boundaries. Triangular elements were used for meshing the core region. Triangular elements have the advantage that they can be easily adapted and refined to a complex geometry (Figure 3.3).

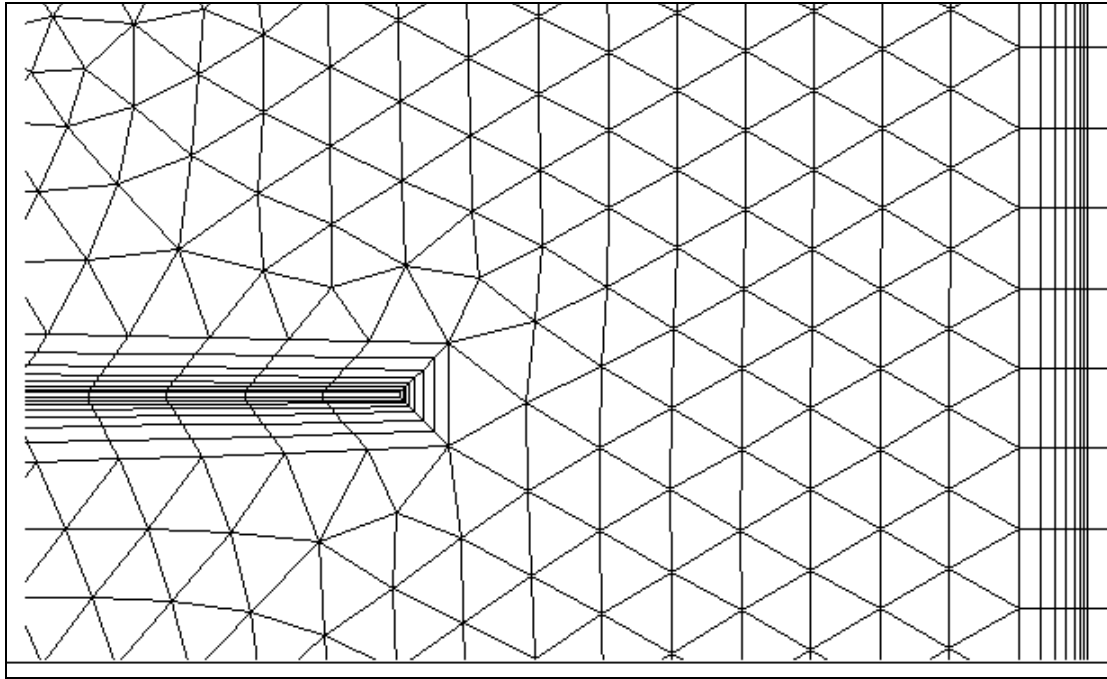


Figure 3.3: The mesh at $\varphi = 0^\circ$.

3.5.1 Mesh Independence

To ensure mesh-independent results, a series of tests were run at various mesh densities and various inlet mean speeds. The mesh at $\varphi = 45^\circ$ was used as an example. The (triangular) element size was varied from 5.5 mm to 1.3 mm to find the appropriate element size (Figure 3.4). The indoor and outdoor glazing temperatures were fixed: 30 and 10 °C, respectively. A uniform heat flux rate was specified at blind walls. The blind surfaces total heat generation term was set to 200 W. The inlet temperature was uniform and fixed: 25 °C. The blind average temperature was used as an indicator to confirm

mesh independent solution. The element size 1.96 mm (35000 control volumes) was deemed sufficiently small. Decreasing the element size below 1.96 mm did not seem to improve the solution accuracy appreciably.

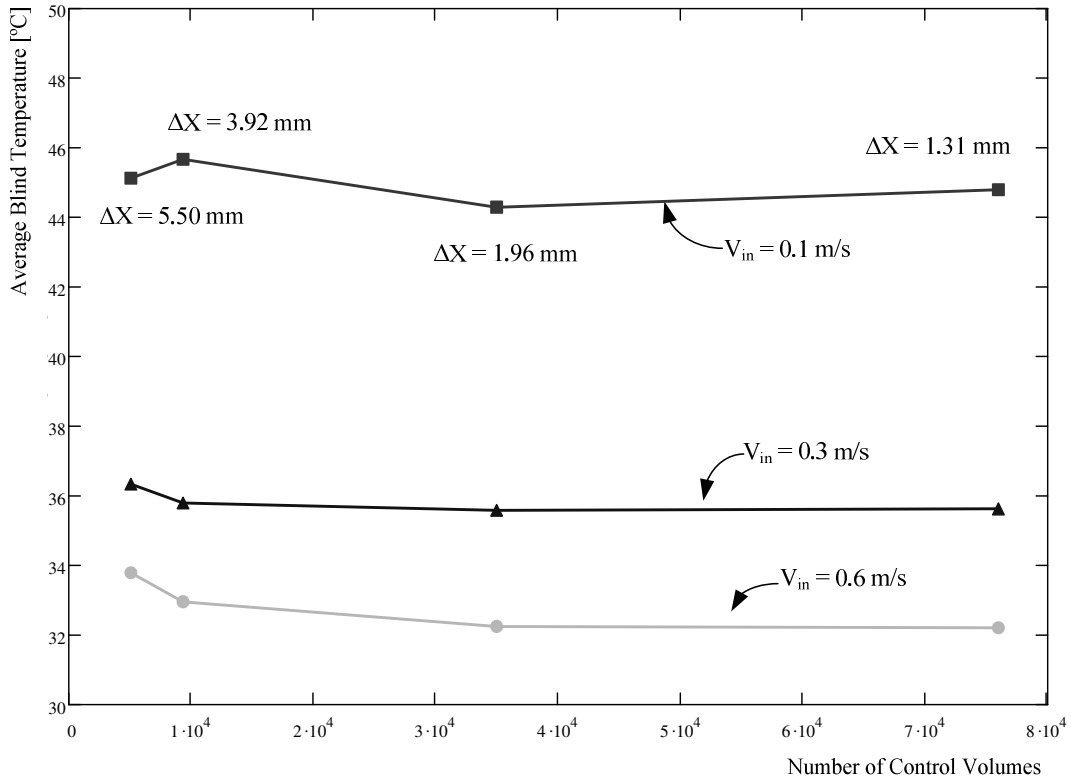


Figure 3.4: Mesh Independence tests.

3.5.2 Near Wall Mesh Resolution

The EWT requires a specific mesh near the wall. To resolve the near wall velocities FLUENT suggests that 10 control volumes be placed in the viscosity-affected region ($y^+ < 5$). Although not presented here, simple channel flow (without obstructions) tests (at similar Reynolds' numbers as encountered in this work) reveal that FLUENT's EWT is actually quite capable of resolving the near wall velocities and predicting, for

example, the wall shear stress satisfactorily (in comparison with published data on wall shear stress) even when there are fewer than 10 control volumes present in the viscosity-affected region. In other words, the criterion of placing 10 control volumes below $y^+ < 5$ is rather conservative. As long as there are a few cells (about 5) placed below $y^+ < 5$, refining the near wall mesh does not seem to improve the near wall solution accuracy appreciably. Given the specific near wall mesh (geometrically decreasing cell size near the walls), if the first cell is placed well below $y^+ = 5$, it is reasonable to believe that there are sufficient number of cells placed in the viscosity-affected region, if not 10, to resolve the viscosity-affected region. A quick y^+ check can be done on the CFD models of the BIPV/T to ensure that there are adequate number of control volumes in the viscosity-affected region. The mesh at $\phi = 0^\circ$ is used as an example to show the range of y^+ values, at three fan speeds, 10, 20, and 30 Hz. The first node glazing walls y^+ and slat walls y^+ fall mostly below 0.45 (Figure 3.5). Therefore, it is suspected that the mesh is sufficiently fine near the walls for the enhance wall treatment of the solid boundaries.

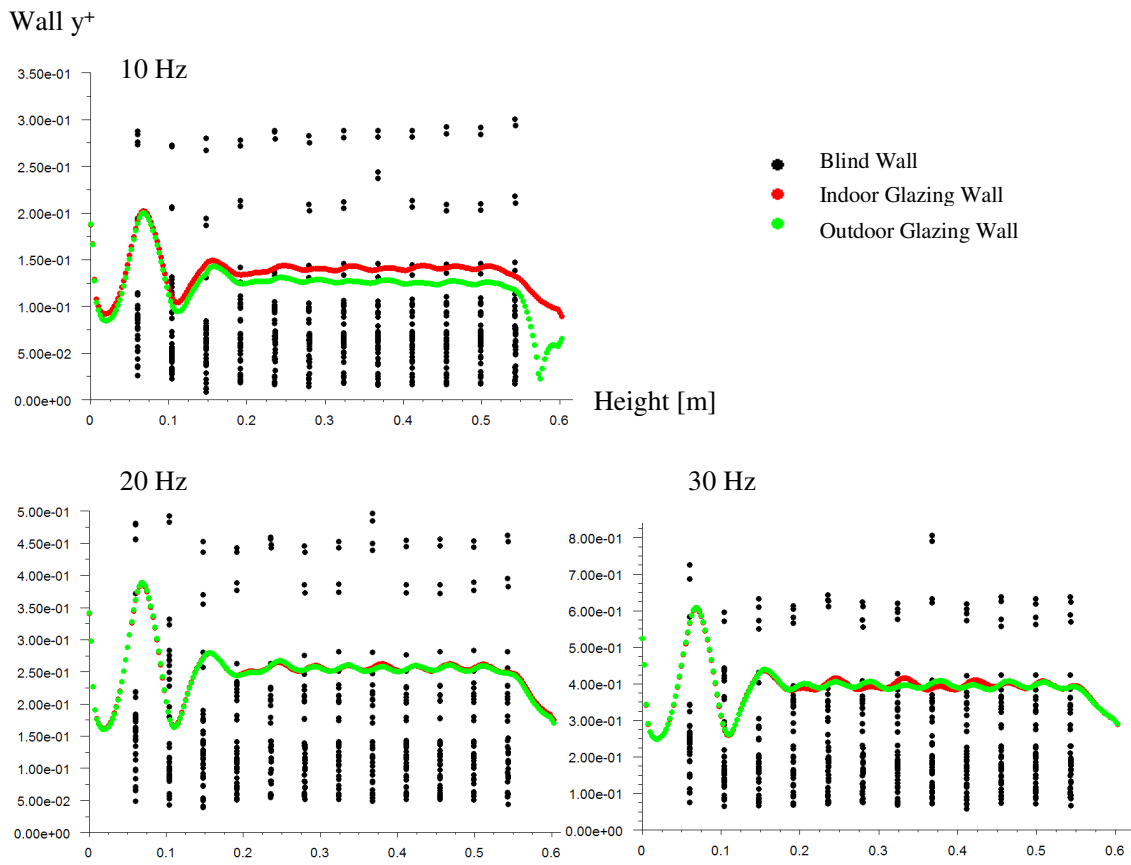


Figure 3.5: Vertical wall y^+ plots, 10 Hz, 20 Hz, 30 Hz, $\phi = 0^\circ$.

CHAPTER 4

MODEL VALIDATION

Chapter 3 presented the numerical models for the BIPV/T system. This chapter presents the experimental setup, procedure and results that were used to validate those models. PIV and temperature measurements were made on the upper section of the Spherical-Solar™ BIPV/T at various blind slat angles and airflow rates. Surface temperature and velocity field comparisons were made between the experimental results and CFD results.

4.1 SYSTEM DESCRIPTION

The upper (vision and shading) section of the Spherical-Solar™ BIPV/T is considered. The two BIPV/T configurations are presented in Fig 4.1. They are located in a rooftop test chamber with room dimensions of 3.0 m × 2.9 m × 3.0 m. The BIPV/T system consists of a 92 mm-wide mechanically ventilated channel, i.e., an AFW, with a 5 mm-thick outdoor glazing layer and an indoor conventional double glazing unit (3 mm thick panes spaced 12.7 mm apart). A venetian blind layer was placed in the middle of the ventilated channel. The blind slats were 49 mm wide, 0.17 mm (± 0.01 mm) thick, and

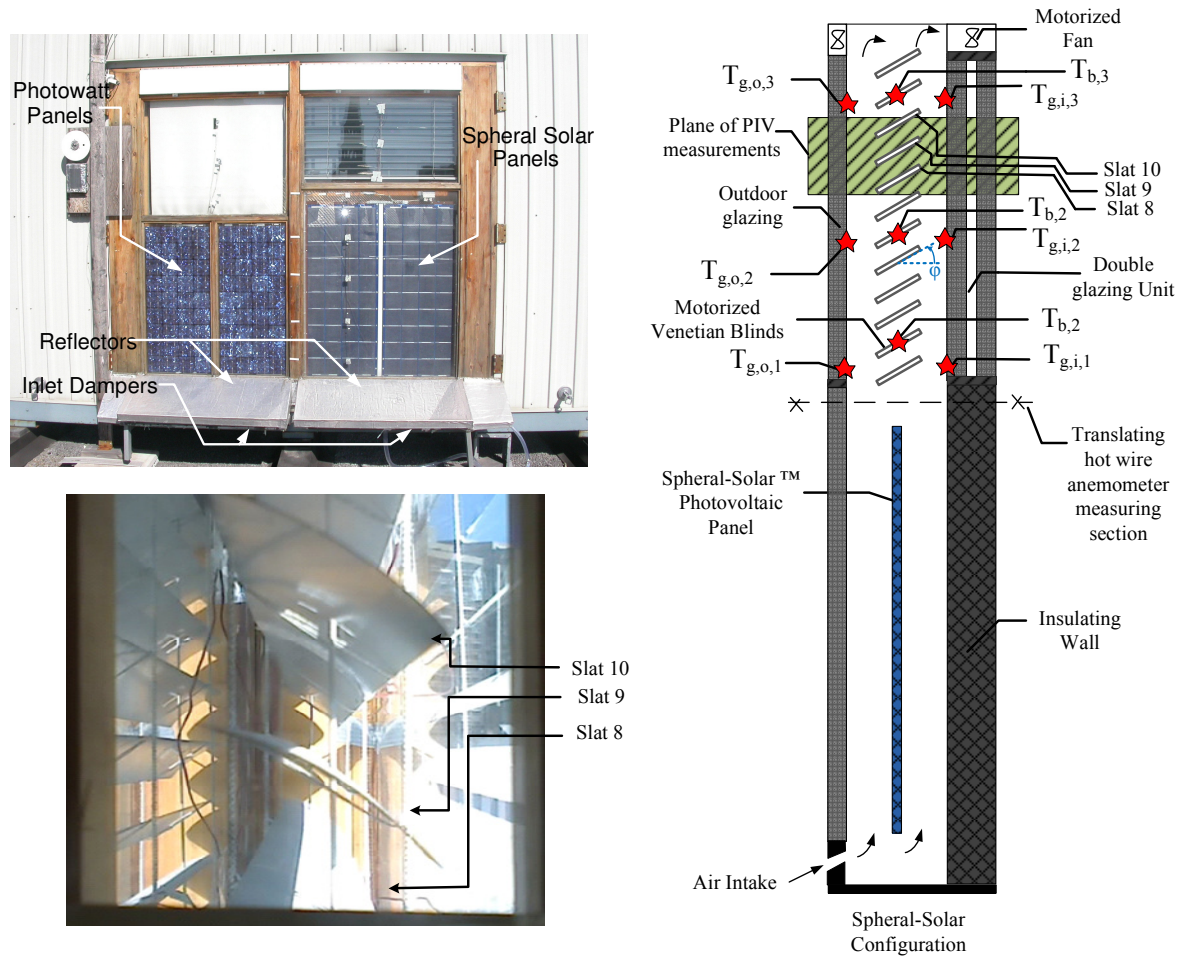


Figure 4.1: The two BIPV/T configurations at Concordia University, a schematic of the Spheral-Solar™ configuration, the location of thermocouples and the plane of PIV measurements.

43.9 mm spaced apart. The BIPV/T system is connected to an AC TECH M1105SB variable frequency fan, operating between 0–60 Hz, with inlet motorized dampers. Total (beam + diffuse) incident solar radiation on a vertical surface (The BIPV/T window) is recorded every minute by a LI-2005A pyronometer mounted on the south-facing facade just above the BIPV/T window. The outdoor ambient weather conditions, namely temperature, wind speed, and wind direction are recorded every minute using an integrated LICOR LI-1401 weather station. An Agilent 34970a data acquisition system recorded the weather data and controlled the operation of the fan and the inlet dampers. Table 3.1 presents a summary of some of the control and measurement equipment.

An Eppley Normal-Incidence Pyroheliometer is placed outside the test hut and measures the direct beam radiation. The diffuse component of total radiation can be calculated via (Duffie and Beckman, 1991)

$$I_{tot} = I_b \times \cos(\theta) + I_d \quad (4.1)$$

where

I_b Direct beam radiation flux, W/m^2

I_d Diffuse radiation flux on a vertical wall due to diffuse ground-reflected and sky radiation, W/m^2

I_{tot} Total incident radiation flux, W/m^2

θ The angle of incidence on a vertical wall. The solar azimuth angle for a vertical surface.

Table 4.1: Some control and measurement equipment

Item	Manufacturer	Model	Power Supply	Measuring Range	Accuracy in percentage of full span output
Pyronometer	LICOR	LI-2005A	7-16VDC	0-1500 W/m ²	±5%
Ambient Temperature	LICOR	LI-1401	7-16VDC	-40-60 °C	±0.8 °C ±3%
Wind	LICOR	LI-1401	7-16VDC	0-180 km/hr	±1.77 km/hr
Damper Control	BELIMO	LM24-SR-2.0US	24VAC± 20% 50/60 Hz 24VDC± 10%	Maximum Angle of Rotation: 95°	
Fan	AC TECH	MS1105SB	120/240VAC	0-60 Hz	
Data Acquisition	Agilent	34970A	120VAC		

4.2 EXPERIMENTAL PROCEDURE

Nine experimental scenarios were considered at three blind slat angles ($\phi = 0, 45^\circ$, and 75°) and three fan frequency settings (10, 20, and 30 Hz) in late-fall or near-winter outdoor conditions (Sep 22, 2008) (Table 4.2). The blind slat angles were chosen to cover a range of blind positions from open to almost-closed. The fan settings were

chosen to cover a suitable and practical range of mean air speeds. The mean air speed inside the channel was limited to a practical range of about 0.1 to 0.6 m/s at all times, below which the natural convection mechanisms drive the flow, and above which the blind slats start to shake unstably in space.

Table 4.2: Experimental scenario design

Scenario	Fan speed	ϕ
1	10 Hz	0°
2	20 Hz	0°
3	30 Hz	0°
4	10 Hz	45°
5	20 Hz	45°
6	30 Hz	45°
7	10 Hz	75°
8	20 Hz	75°
9	30 Hz	75°

Between-the-panes indoor glazing, outdoor glazing and blind surface temperatures were measured using T-type thermocouples (accuracy $\pm 0.5^\circ\text{C}$) at three locations along each glazing and shading layer: near the top and the bottom frame, and in the center of the glass (Figure 4.1).

PIV measurements were made at a location far downstream of the inlet, but sufficiently far away from the outlet, in anticipation that the flow would be fully periodically

developed at that location, meaning that the velocity field between every two slats would repeat itself. The plane of PIV measurements consisted of a section containing three consecutive blind slats and the space in between (Figure 4.1).

Detailed inlet (and outlet) modelling is important in numerical modelling of forced flow in BIPV/T systems (Saelens, 2002, and Mei et al., 2003). A translating hot wire anemometer (temperature accuracy of $\pm 0.3^\circ\text{C}$ and velocity measurement repeatability of $0.03 \text{ m/s} \pm 1\%$ of reading) measured the air velocity and temperature at the inlet of the system, just below the blind layer and just above the PV panel, at eleven equally-spaced measuring locations across the channel. About ten measurements were recorded at measuring location for each scenario. Although not presented in this work, hot wire anemometer and PIV observations showed that the inlet streamwise velocity profiles (and the temperature profiles to some extent) were usually highly asymmetric. Because of the placement of the air intake, the PV and the opaque wall behind PV, the indoor side of PV receives more air flow than the outdoor side. Therefore, it is important to accurately model the inlet.

The outdoor ambient temperature, T_{ext} , varied from 10.8 to 13.1 °C. The indoor ambient temperature, T_{int} , was maintained at about 22 °C at all times. The sky was clear during all scenarios. The indoor and outdoor conditions, inlet conditions, and incident solar radiation were averaged and assumed to be constant during each scenario, which took only about three minutes.

4.3 PIV EQUIPMENT SETUP

PIV is a whole-field and non-intrusive velocity measuring technique that can be used for internal channel flows. The entire flow field can be captured at once, and no external probes are inserted into the flow. A Dantec Dynamics PIV system, including the lasers, the traverser, and the computer processor, was installed inside the test hut (Figure 4.2). NewWave Solo 120 15Hz Nd:YAG lasers, which could deliver up to 50 mJ at a wavelength of 532 nm, were used to illuminate the seeding particles. The Laser sheet thickness was 1.5 mm.

A 10-bit charged-couple device (CCD) Nikon camera (1600x1186 pixels) and a Nikon Nikkor lens (60 mm focal length and F/2.8 aperture designation) were used to record the position of the illuminated seeding particles. A Bostitch CAP2060P compressor was used to generate olive oil seeding particles (approximately 3 μm in diameter). The lasers provide two consecutive pulses (bursts) with a very short time difference between the two pulses. The camera was then synchronized with the lasers and recorded two pictures in a row. PIV is based on the spatial and temporal resolution of motion of the small particles released inside the flow. These particles, called seeding particles, act like markers; By comparing their location at the beginning and at the end of a short time interval, the velocity vector can be calculated at that specific time and location. The time between the pulses, Δt , ranged from 650 μs to 2600 μs , depending on the maximum flow speed, to ensure appropriate particle displacement within an interrogation cell (see Section 4.5.1: Particle Displacement). For each measurement, about 500 sets of pictures were taken. The uncertainty due to finite sample size was

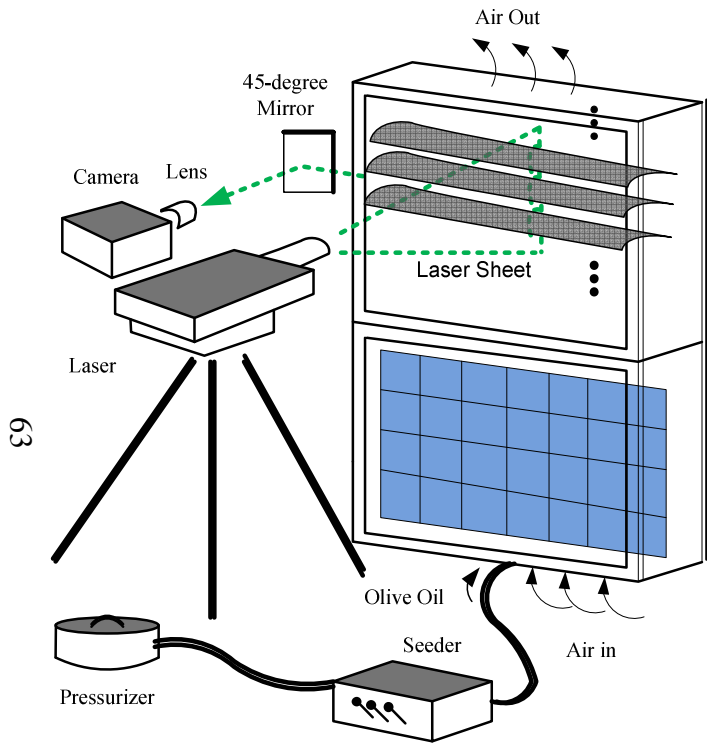


Figure 4.2: PIV equipment setup.

evaluated (see Section 4.5.2: Uncertainty) and it was considered to be reasonably small for the purposes of this work , i.e., model validation.

A 45° reflecting mirror was used to allow the camera to be placed parallel to the laser on the traverser. The blind slat angle was set to zero for all PIV measurements to limit undesirable shading of the laser sheet behind the slats. These shaded regions can be seen in Figure 4.5 (page 68) to the right of the slats, and they are larger at non- zero slat angles. The shaded regions may result in many inaccurate velocity calculations in the interrogation cells where they fall. To measure the velocity field at non-zero slat angles, a more sophisticated laser-mounting apparatus, such as a special tripod, must be used to direct the laser beam parallel to the slats.

4.4 PIV CORRELATION, VALIDATION, AND MASKING

The recorded image of the field-of-view of PIV can be divided into a number of small cells referred to as interrogation cells. Each interrogation cells contains several particle images. Each particle may take up a few pixels in the image domain. Analysis of the displacements of images by means of spatial correlation methods (cross-correlation or auto-correlation) leads to an estimation of the fluid velocity in each interrogation cell. An example of what a correlation plane looks like in an interrogation cell is shown in Figure 4.3. The highest peak in the correlation plane leads to the calculation of the fluid velocity in that interrogation cell.

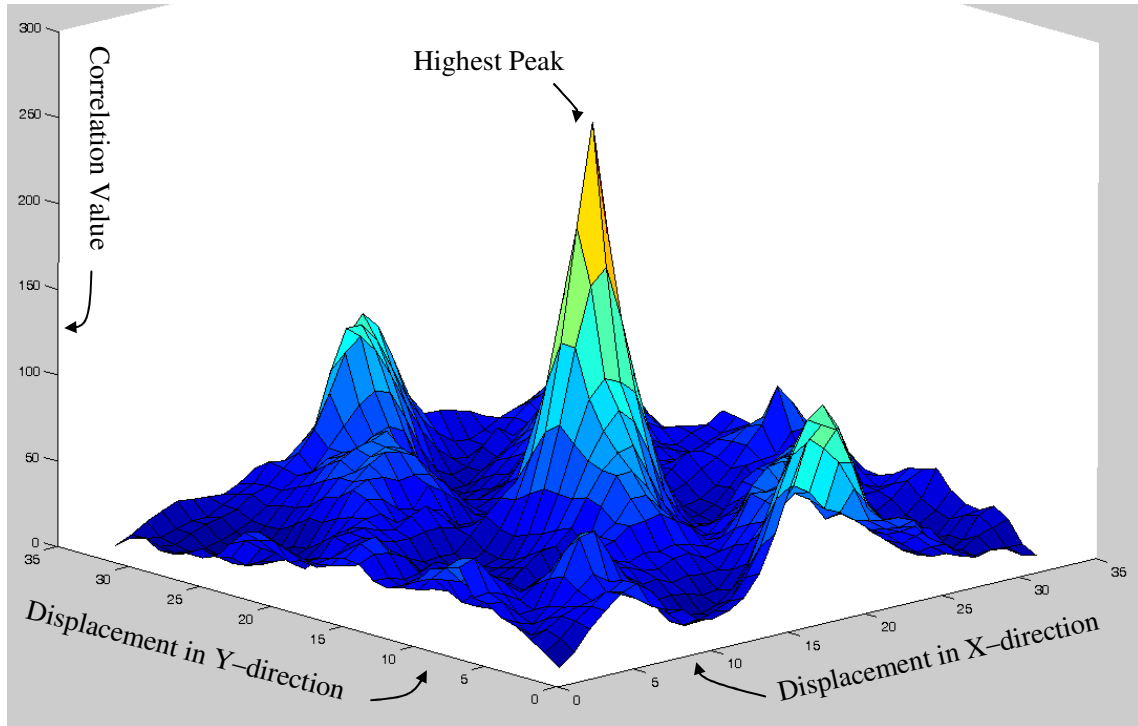


Figure 4.3: An example of a correlation plane.

The “adaptive cross-correlation” algorithm (FlowManager, 2002) was employed to calculate the velocity vectors in a final interrogation cell size of 32×32 pixels with 50% overlapping between adjacent cells. While a 16×16 interrogation cell size is usually used, a 32×32 interrogation cell size was used in this work to ensure that there are sufficient seeding particles in each cell. The adaptive correlation is commonly referred to as the ‘super-resolution’ algorithm. The super-resolution algorithm is a two-pass algorithm where the image of the field-of-view is analyzed first using conventional correlation analysis. Then, the information about the velocity vector calculation is used to “enhance the probability of being able to track the individual particles within interrogation cells” (Adrian, 1997). Interrogation cell size was 64×64 pixels in the first

pass and 32×32 pixels in the second pass. Figure 4.4 illustrates interrogation cell subdivision in the super-resolution algorithm. The ultimate resolution in PIV is determined by one's ability to track individual particles (Adrian, 1991). The super-resolution algorithm makes it possible to achieve higher spatial resolutions as it is possible to achieve reliable pairing of a large fraction of the particle image pairs (Keane et al., 1995).

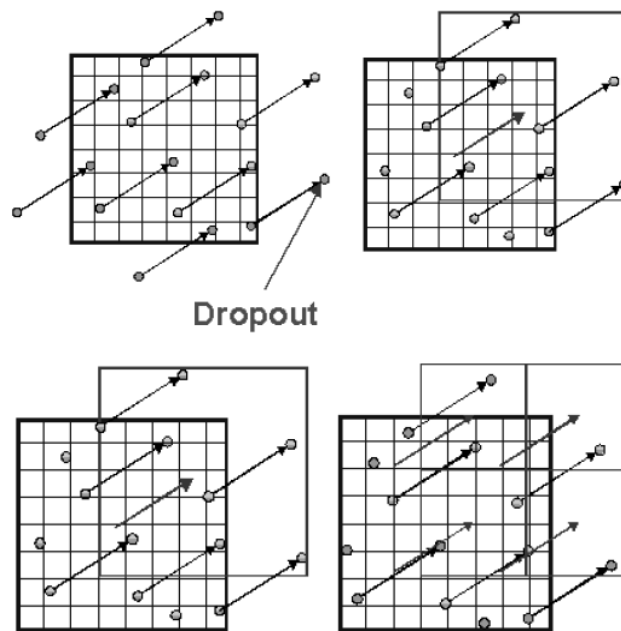


Figure 4.4: The super-resolution (adaptive correlation) algorithm showing interrogation area subdivision (reproduced from FlowManager, 2002).

FlowManager (2002) claims that the adaptive correlation algorithm is suitable for flows where large velocity gradients exist and flows where small scale motions are embedded in a large scale motion. The flow in this work experiences large shear near the tips of the blind slats and also contains some small scale motions (slow-

moving vortices) embedded in a large scale bulk flow motion (the core flow region). Therefore, the adaptive correlation is chosen in this work.

“Outliers” are incorrect vectors resulting from noise in the correlation plane. It is possible, but usually not necessary, to recognize these vectors and replace them with more accurate vector estimations. Recognizing outliers (validation) and replacing them with other vectors (substitution) in PIV are largely for “visual appearance” reasons (FlowManager, 2002). For example, when presenting the velocity vector field or the streamline contours based on the vector field, it is desirable to recognize outliers and replace them with better-looking vectors (see Figures 4.11–4.13, pages 80–82). Therefore, a “peak validation” option, with a minimum acceptable ratio of 1.1, and a “local neighbour averaging substitution” option were selected in FlowManager to post process PIV results. Thus, if the ratio of the height peak to the second highest peak in the correlation plane is smaller than 1.1, then the velocity calculation in that interrogation cell is replaced by an average of its neighbouring vectors. The validation and substitution affected only about 9% of the velocity vector calculations at 10 Hz, 8% at 20 Hz, and 10% at 30 Hz. Therefore, the PIV results were not significantly altered by the validation and substitution process described above. In fact, most of the vertical velocity values that are used for model validation (see Figures 4.14–4.15, page 83, and Figure 4.19, page 89) were not affected by the rejection and substitution process.

While validation and substitution are optional, it is necessary to manually disregard the velocity calculations in regions where the laser sheet is shaded. Unwanted laser sheet

shading on one side of the blind slats can contaminate the otherwise good velocity calculation. Therefore, a mask was created and applied to all PIV images (Figure 4.5).

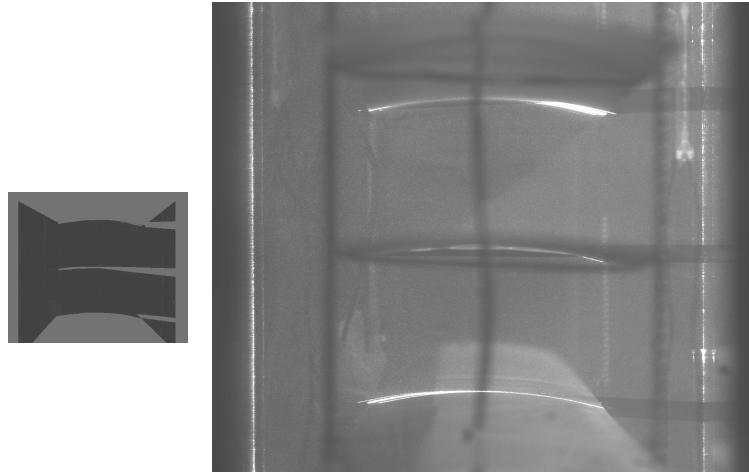


Figure 4.5: A typical PIV picture showing the laser sheet shading on the right side of the slats and the mask.

4.5 PIV UNCERTAINTY ESTIMATION

It is important to quantify and find bounds on the uncertainties associated with any experimental technique, including PIV. The uncertainties in PIV measurements were considered in the context of particle displacement, standard deviation in the velocity calculations, and dynamic and spatial ranges.

4.5.1 Particle Displacement

The laser pulse delay setting and the interrogation cell size can significantly affect the particle displacement on the image plane and are therefore related to the uncertainties in PIV. Too large of a particle displacement, relative to the interrogation cell size, may result in the image of the particles to be lost. This is what is referred to as “loss of pairs” where either the initial or the final particle position is lost. To minimize the error in PIV

associated with loss of pairs, it is generally recommended to keep the displacement of the particles below one-quarter of interrogation cell size (FlowManager, 2002).

This means that in a final interrogation cell size of 32×32 the ideal particle displacement must be around 8 pixels, not much larger. The laser pulse delay must be set according to the mean fluid velocity to give a displacement of about 8 pixels. The laser pulse delay must be 2600 μs at 8Hz fan setting (mean fluid speed of about 0.1 m/s) because the maximum local velocity is about 0.375 m/s. The laser pulse delay must be 650 μs at 30 Hz. At 8Hz:

$$\frac{\sqrt{u^2 + v^2_{\max}} \cdot (\Delta t)}{\text{Size of one pixel}} \approx 8 \quad (4.1)$$

$$\text{Size of one pixel} = \frac{\text{field of view in X - direction}}{\text{CCD camera dimension in X - direction}} = \frac{196\text{mm}}{1600\text{pixels}} = 0.1225\text{mm}$$

$$\frac{(0.375\text{m/s}) \cdot (\Delta t)}{0.1225\text{mm}} \approx 8$$

$$\Delta t \approx 2600\mu\text{sec}$$

4.5.2 Standard Deviation

The random fluctuations in the PIV technique and the turbulent fluctuations in the flow give rise to uncertainties in the PIV velocity calculations. It is essentially impossible to separate the effects of the random (equipment and correlation algorithm) fluctuations and the turbulent fluctuations on the individual velocity calculations. Therefore, the standard practice is to find a range of uncertainties (standard deviation) in velocity calculations resulting from the combined effects of both random and turbulent

fluctuations. The uncertainties can be calculated based on the standard deviation and the number of samples and can be expressed as a percentage of the mean fluid velocity:

$$P = \frac{1.96\sigma}{\sqrt{N}} \quad (95\% \text{ confidence}) \quad (4.2)$$

where

σ Standard deviation

N Sample size

In the core flow region the uncertainties were about 3–7% at 10 Hz, 3–7% at 20 Hz, and 8–11% at 30 Hz. In the recirculation regions the uncertainties were about 1–5% at 10 Hz, 2–6% at 20 Hz, and 5–8% at 30 Hz. The uncertainties were sometimes fairly large, given that they are usually lower than 5% in PIV, but a number of factors in this flow may be responsible for the occasionally high uncertainties:

- 1) The experiments were conducted in an outdoor test hut and wind gusts would cause instability.
- 2) There is some evidence (compare Figures 4.8 and 4.9, pages 77 and 78) that parts of the flow (between the blind slats) may be unsteady in nature resulting in high uncertainties.
- 3) Three dimensional structures in the flow may be present.

4.5.3 Dynamic Velocity and Spatial Ranges

The Dynamic Velocity Range (DVR) and the Dynamic Spatial Range (DSR) are measures of PIV's equipment limitations and resolutions. A DVR and DSR assessment

must always be performed to make sure that the range of velocities has been appropriately bracketed and the PIV equipment has been used in an appropriate way.

The DVR is the ratio of the maximum resolvable velocity to the minimum resolvable velocity. The minimum resolvable scale is the rms in velocity measurement, σ_u . The DVR represents the range of velocities that can be experimentally investigated and is inversely proportional to the uncertainties in velocity calculations. The DSR is the number of independent (i.e. non-overlapping) vector calculations that can be made in a linear section of the field of view. It is related to the spatial resolution of the flow field, and is defined as the ratio of the maximum resolvable displacement to the minimum resolvable displacement. Large DSRs allows one to measure small-scale variations embedded in a large-scale motion. The “PIV uncertainty principle” states that the product of the DVR and DSR is a constant for a given set of instruments (Adrian, 1997). For this reason the choice of PIV settings, such as the laser pulse delay and the interrogation cell size depend on a reasonable compromise between the DVR and DSR. The DVR is (Adrian, 1997):

$$DVR = \frac{u_{\max}}{\sigma_u} = \frac{u_{\max}}{\sigma_{\Delta x} / M \Delta t} \quad (4.3)$$

where

u_{\max} Maximum fluid velocity, m/s

$\sigma_{\Delta x}$ rms in velocity calculations in the pixel domain, m/s

M Magnification

Since $\sigma_{\Delta X}$ is equipment dependent and very difficult to estimate, if not impossible, FlowManager (2002) recommends that DVR be roughly calculated as:

$$DVR = \frac{\text{maximum displacement in number of pixels}}{0.1} \quad (4.4)$$

The DSR is:

$$DSR = \frac{L_x / M}{\Delta X_{\max}} \quad (4.5)$$

where,

L_x / M Field of view of camera, in number of pixels

ΔX_{\max} Maximum particle displacement, in number of pixels

The DVR and DSR were always bracketed to a reasonable range of about 100 to 200.

At 30 Hz for example:

$$DVR = \frac{9.2}{0.1} = 92$$

$$DSR = \frac{1600 \text{ pixels}}{9.2 \text{ pixel}} = 174$$

4.6 VELOCITY FIELD VALIDATION

Instantaneous and time-averaged velocity vector fields from PIV reveal that the general shape of the velocity fields agrees with the CFD simulations. Instantaneous velocity vector fields (Figures 4.6–4.9, pages 75–78) reveal that at all air flow rates, the flow tends to move mostly on the left and the right sides of the blind slats (i.e., the core flow region) and between the blind slats two relatively slow-moving vortices are observed,

which change in size and location with time (compare Figures 4.8 and 4.9). The fluid velocity is relatively high in the core flow region and no apparent mass crosses over (from one side of the blind layer to the other). The contours of streamlines obtained from CFD revealed that the flow speed is relatively high in the core flow region and two counter-rotating vortices of about equal size are formed between every two blind slats (Figure 4.10, page 79). These vortices have been previously observed at $\phi = 0^\circ$ in a numerical study of flow field around blind slats (Safer et al., 2005). Although the mean flow speeds and the ratio of the slat width to the channel width were quite different in that work, similar vortices were observed. The blind layer effectively divides the flow into two streams, one to the left and one to the right of the blind layer, and no apparent mass cross-over occurs between the two streams.

While instantaneous velocity fields suggest that the vortices change in size and location, averaging the velocity fields tends to give seemingly large and stable-looking vortices, of about equal size (Figures 4.11–4.13, pages 80–82). The average velocity fields seem to compare better with the CFD solutions, qualitatively, than the instantaneous fields. Although the average velocity fields seem to match the CFD solutions, neither of the two gives a true representation of what actually happens in the flow. From the instantaneous pictures, unlike what the average fields suggest, the flow is likely unsteady and periodic because the vortices are not stable.

In the regions near the glazings (boundary layer regions) and near the blind slats (especially near the tips of the slats) undesirable laser scattering causes much contrast

difference in the PIV pictures compared to the surrounding regions. The undesirable laser scattering causes the outlines of the glazing and the blind slats to be visible in Figure 4.5. In the regions near the glazings and blind slats, the PIV calculations are unreliable and must not be used for any sort of validation; However, in the core flow region and in between the blind slats (regions not very close to the glazings or the blind slats), both average and instantaneous fields show fast uni-directional motion and some sort of slow recirculatory motion, respectively, suggesting that the general shape of the velocity field agrees between CFD and PIV.

Considering the streamwise velocities, the streamwise velocity profiles match with the CFD predictions in the recirculation regions and in the core flow regions, except near the glazings. The streamwise velocity profiles are shown in Figures 4.14 and 4.15 (page 83), corresponding to scenarios 1 and 3, at a horizontal section, $y = 475.6$ mm, mid-height between slats 8 and 9. In the region where the largest errors occur (to the right of the blind layer in the core flow region the error is about 33% at 10 Hz (absolute error of 0.12 m/s) and 21% at 30 Hz (absolute error of 0.32 m/s). While these errors seem to be large, peak velocities (in the core flow regions on the right and left side of the blind layer) compared well between PIV and CFD. At 10 Hz the peak velocities have an error of 5% on the left side and 18% on the right side of the blind layer, and at 30 Hz they have errors of 11% on the left and 0.5% on the right side.

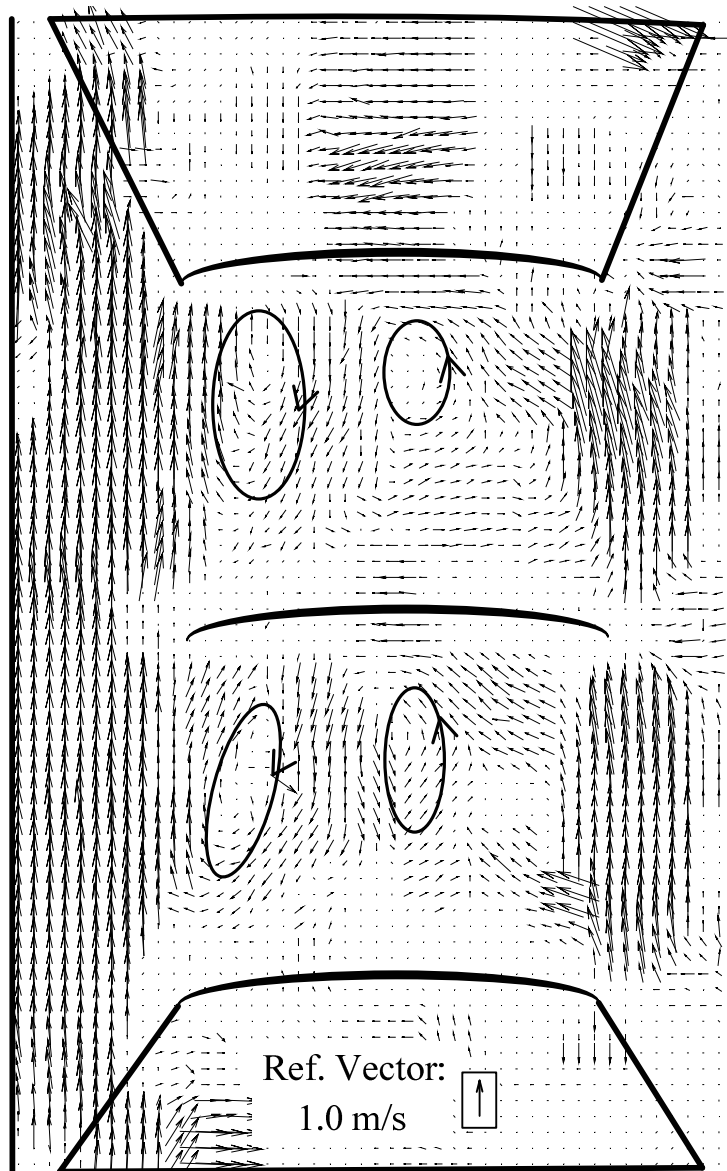


Figure 4.6: The instantaneous velocity field, $\phi = 0^\circ$, fan speed = 10 Hz, $V_{in} = 0.13$ m/s.

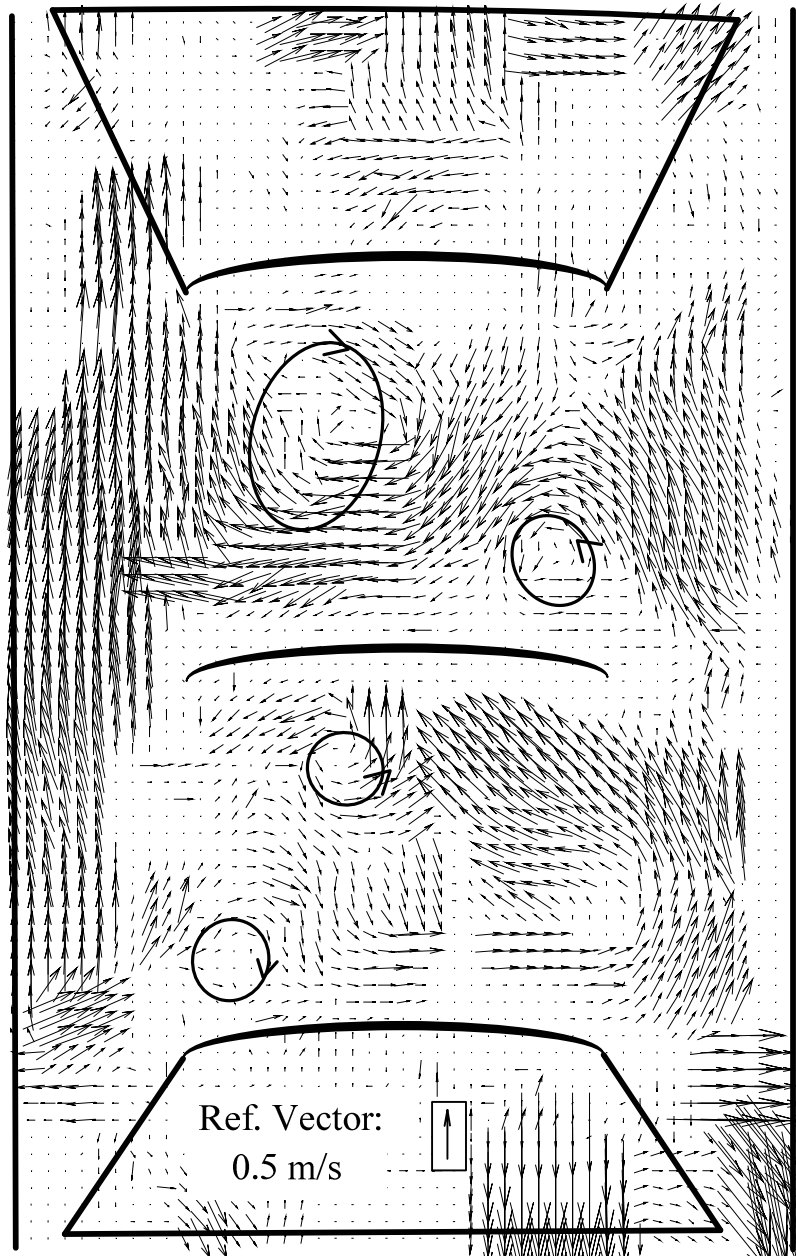


Figure 4.7: The instantaneous velocity field, $\phi = 0^\circ$, fan speed = 20 Hz, $V_{in} = 0.31$ m/s.

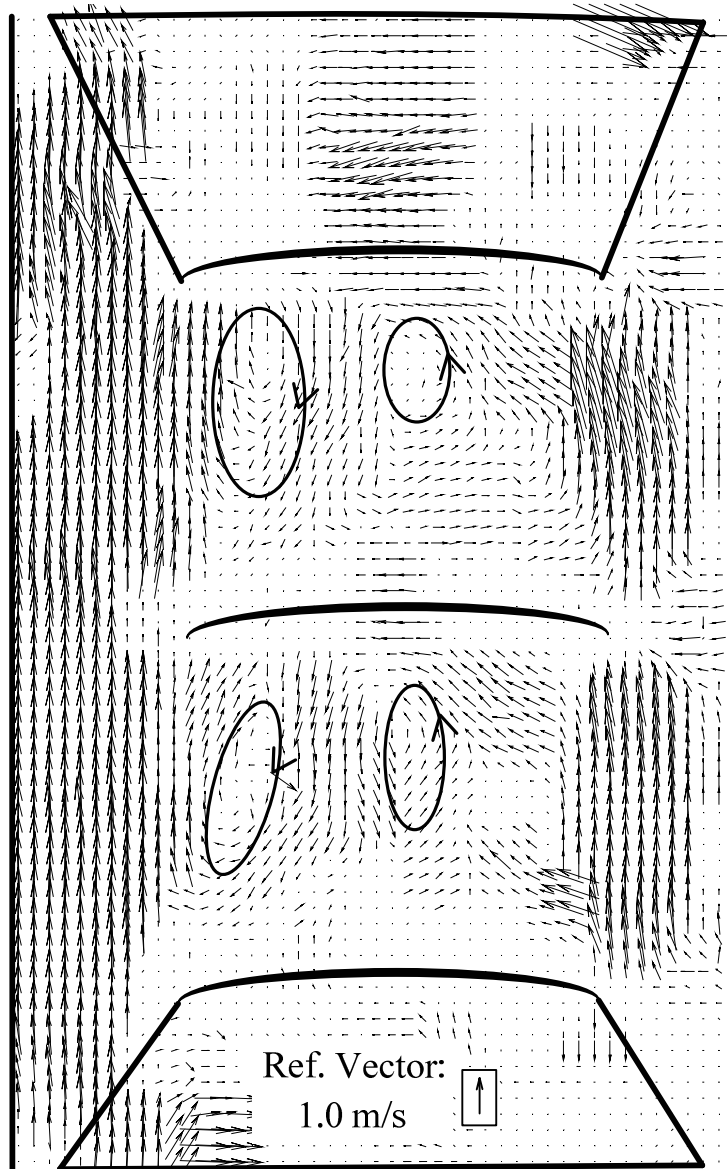


Figure 4.8: The instantaneous velocity field, $\phi = 0^\circ$, fan speed = 30 Hz, $V_{in} = 0.56$ m/s.

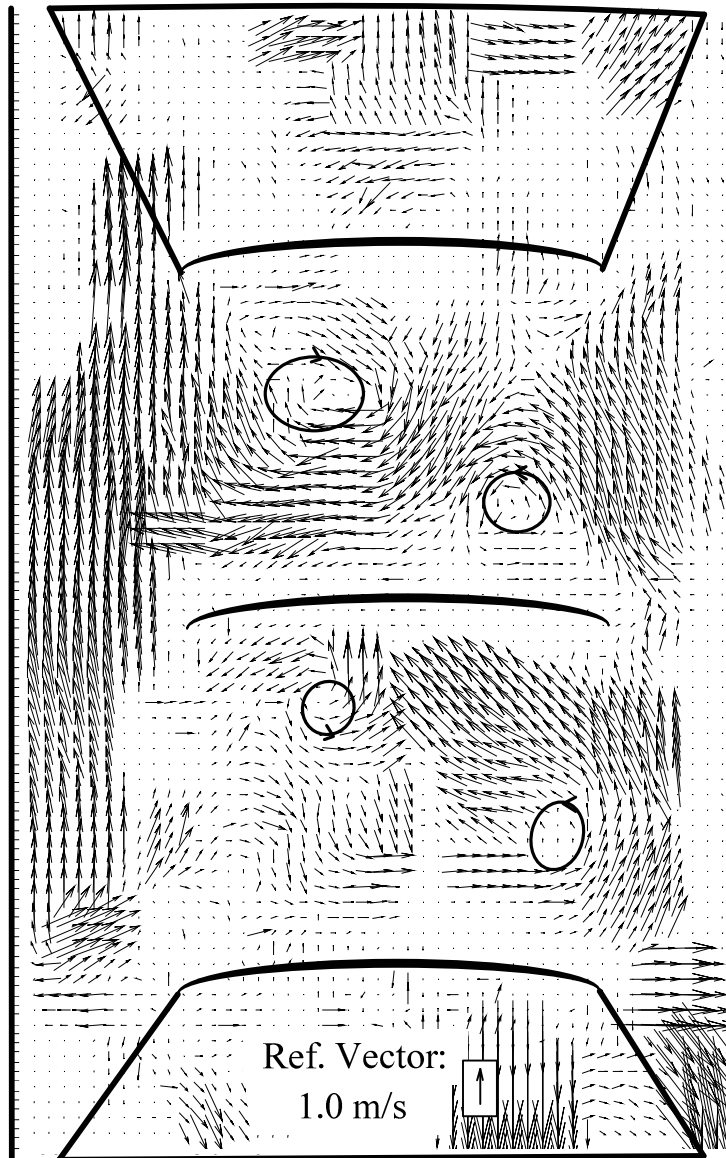


Figure 4.9: Another instantaneous velocity field at 30 Hz, $\varphi = 0^\circ$, $V_{in} = 0.56$ m/s.

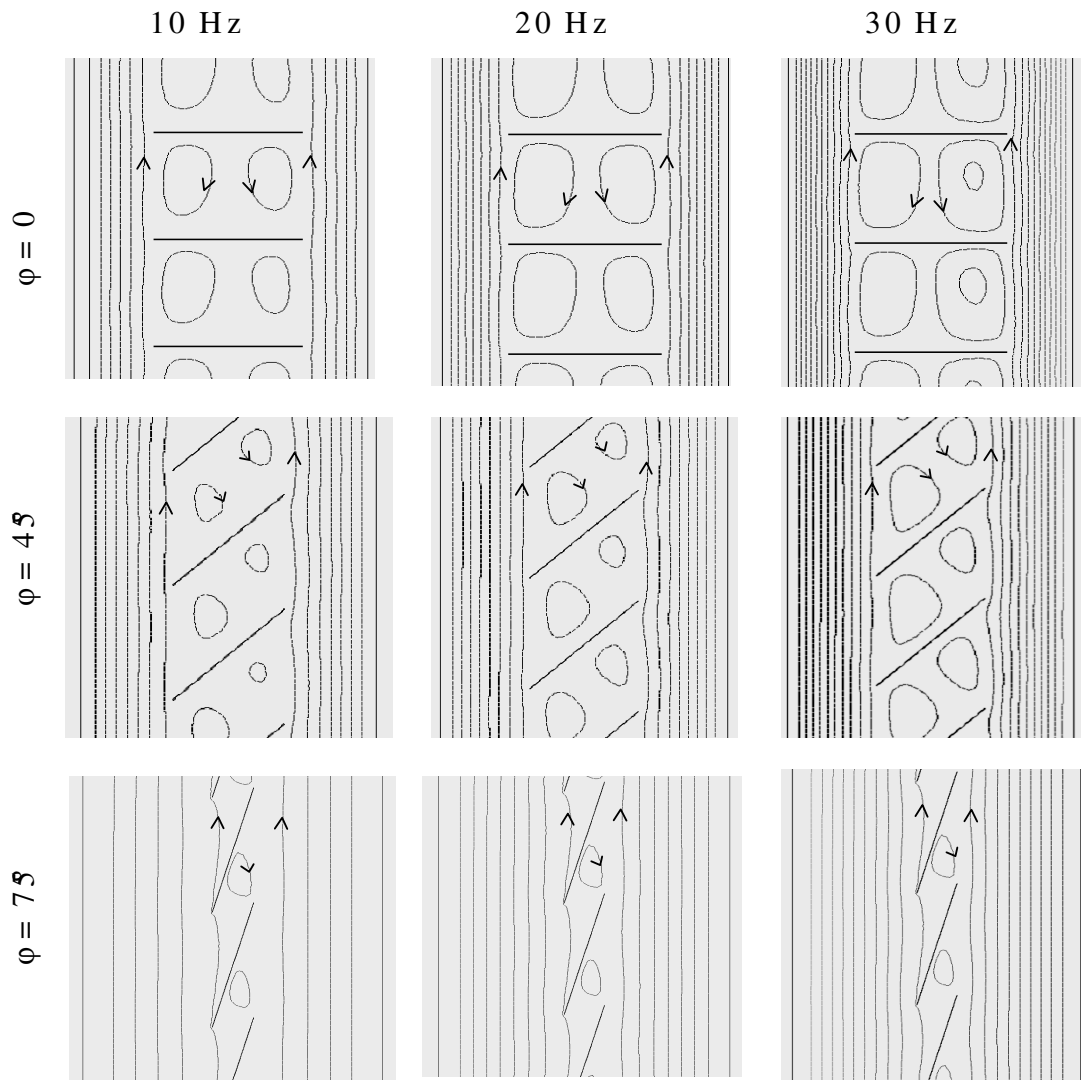


Figure 4.10: The streamline contours from CFD.

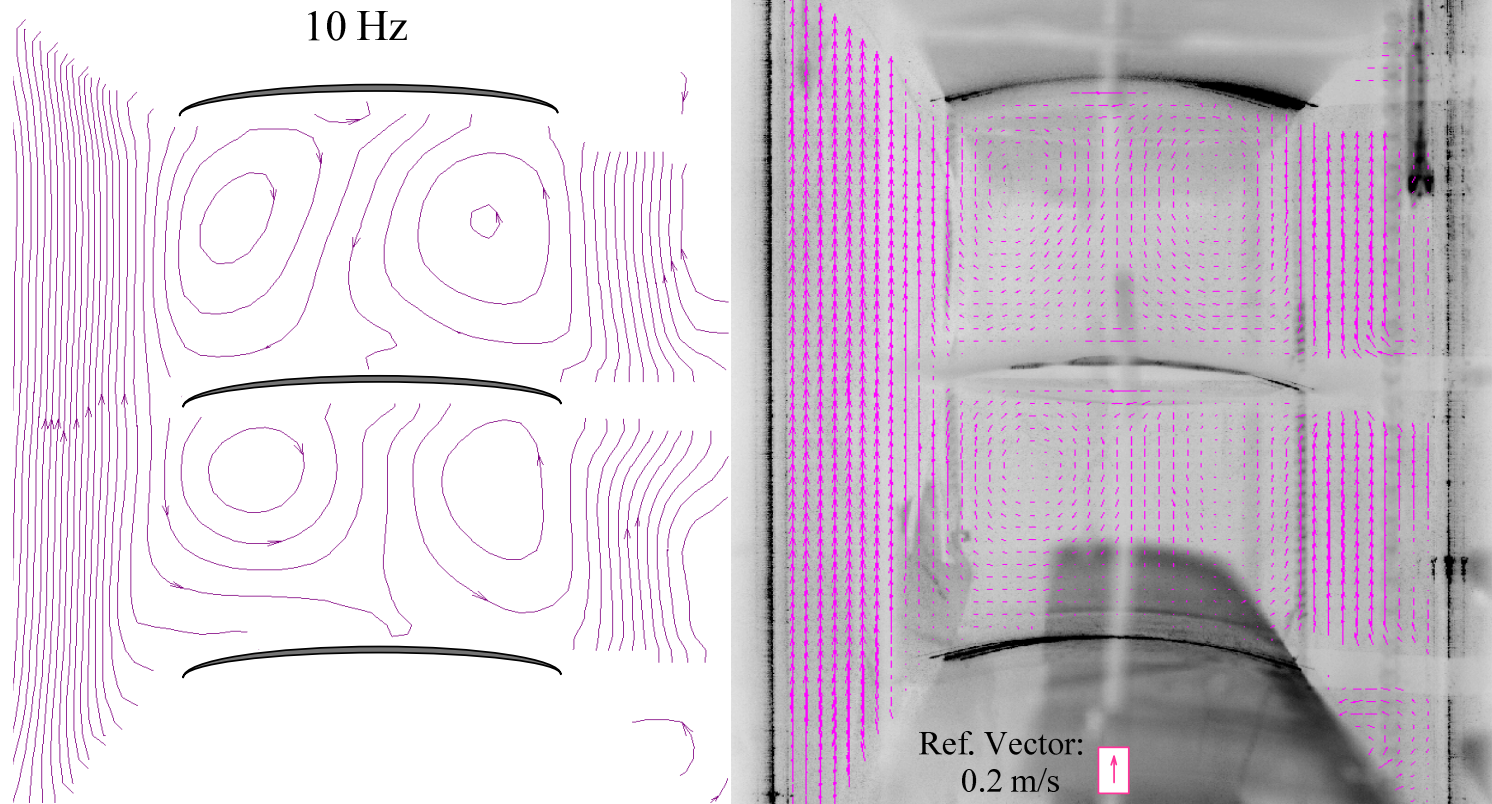


Figure 4.11: Approximate streamline contours and velocity vector field, $\phi = 0^\circ$. Fan speed = 10 Hz, $V_{in} = 0.13$ m/s.

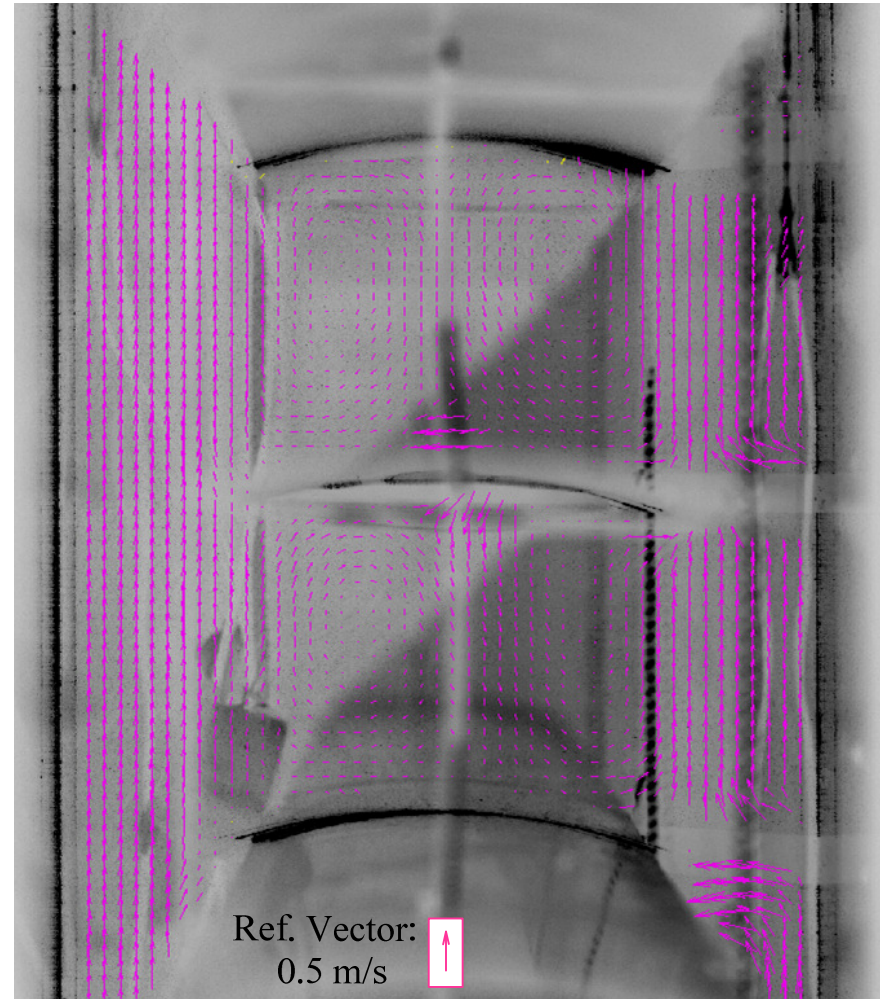
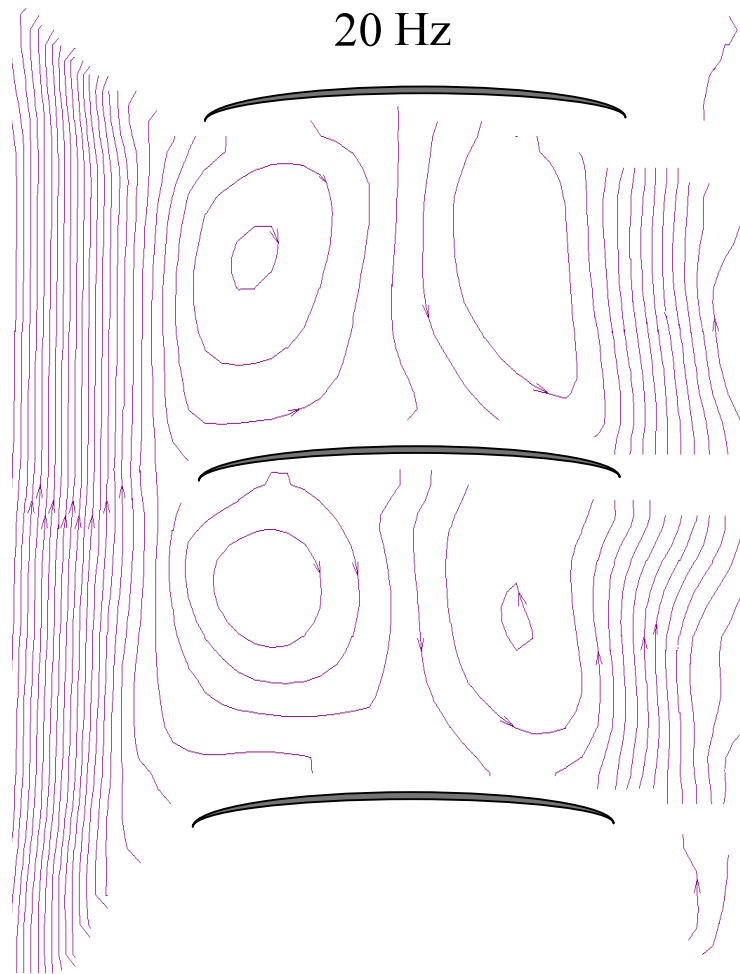


Figure 4.12: The streamline contours and velocity vector field, $\varphi = 0^\circ$. Fan speed = 20 Hz, $V_{in} = 0.31$ m/s.

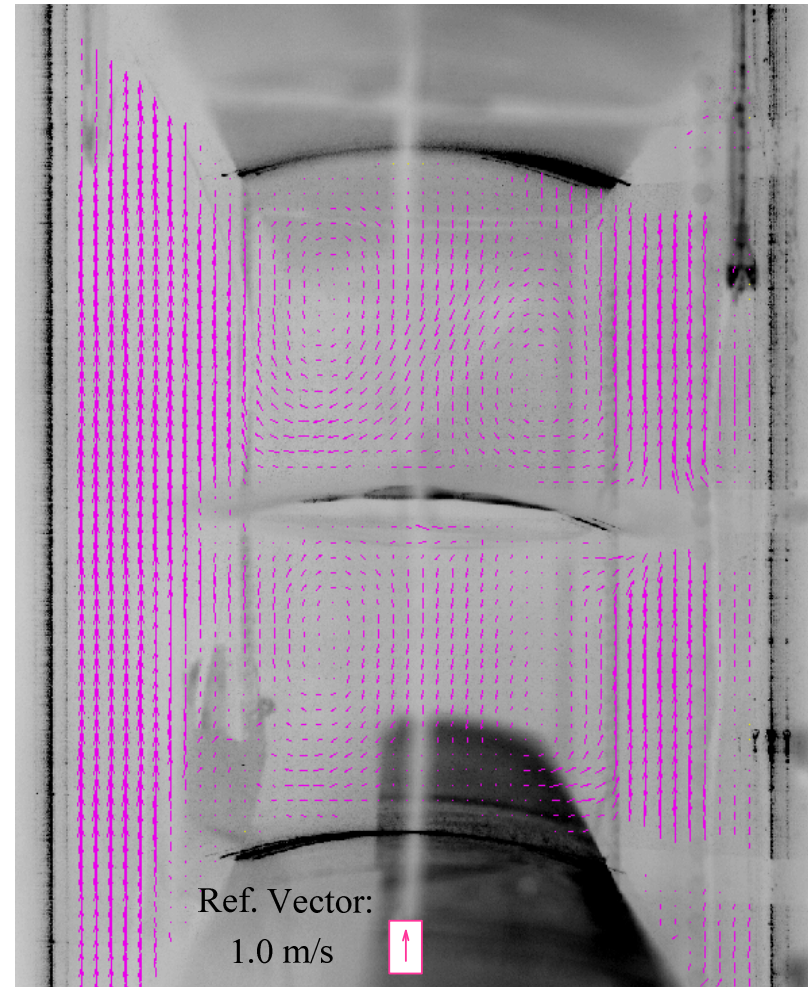
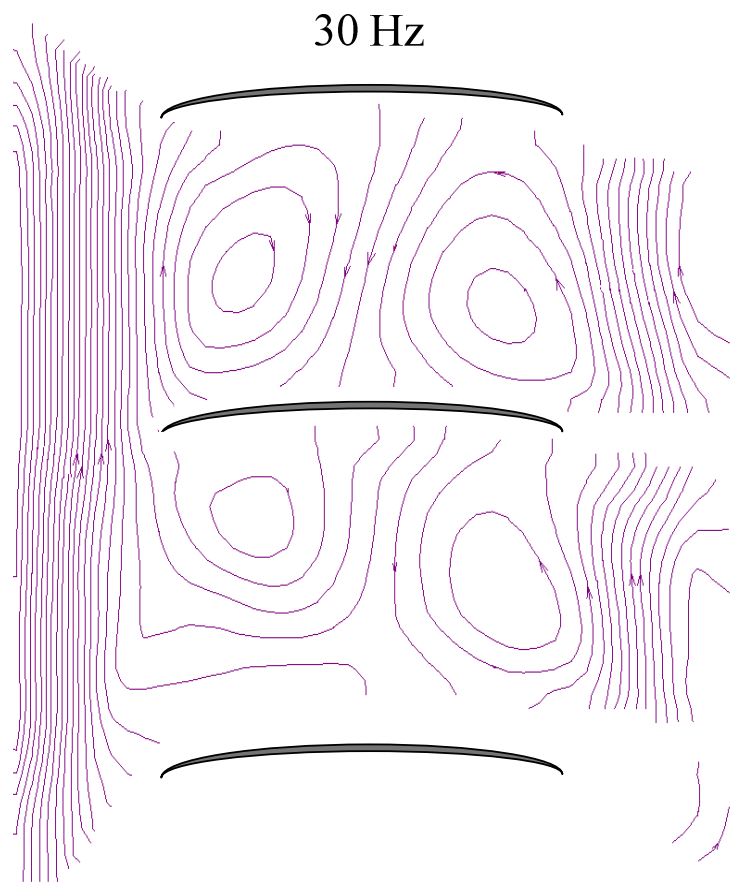


Figure 4.13: The streamline contours and velocity vector field, $\phi = 0^\circ$. Fan speed = 30 Hz, $V_{in} = 0.56$ m/s.

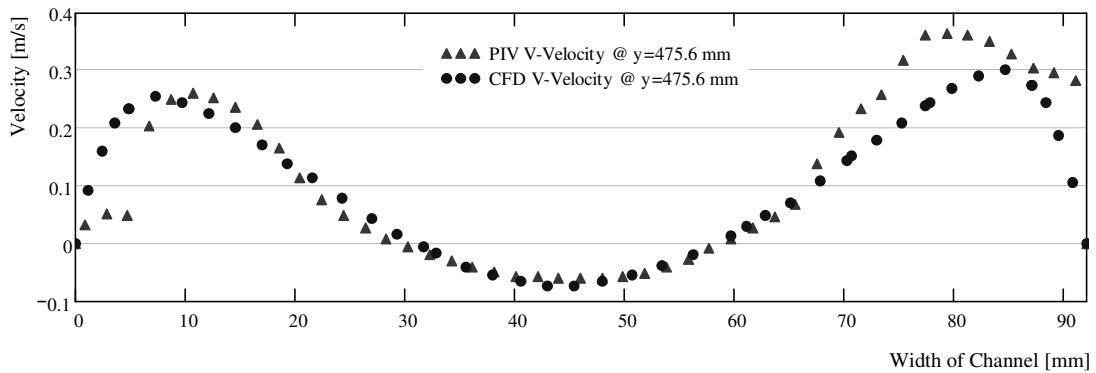


Figure 4.14: Streamwise velocity Profile from PIV and CFD, mid-height between slats 8 and 9, $\phi = 0^\circ$, 10 Hz, $V_{in} = 0.13$ m/s.

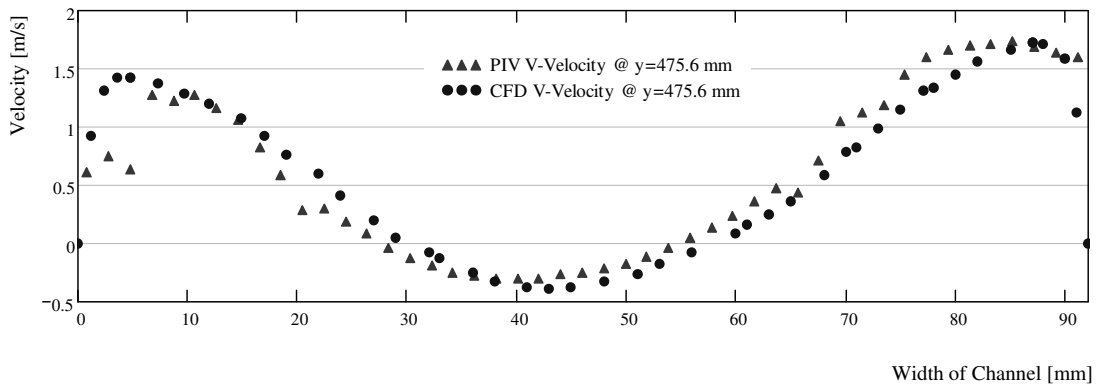


Figure 4.15: Streamwise velocity Profile from PIV and CFD, mid-height between slats 8 and 9, $\phi = 0^\circ$, 30 Hz, $V_{in} = 0.56$ m/s.

4.7 TEMPERATURE VALIDATION

Between-the-panes mid-height (center-of-window) glazing and blind surface temperature comparisons were made between the CFD results and the experimental measurements (Figures 4.16–4.18). The experimental temperatures appear as scattered error bars and have a confidence interval of 95%. The uncertainties in temperatures were calculated according to

$$\bar{T} - T' < T < \bar{T} + T' \quad (4.6)$$

and

$$T' = \sqrt{b^2 + p^2} \quad (4.7)$$

where

\bar{T} Mean Temperature

T' Uncertainty in Mean Temperature (95% confidence interval)

b Bias error: ± 0.5 °C according to the thermocouple manufacturer

p Precision error: $p = \frac{1.96\sigma}{\sqrt{N}}$

and

σ Standard Deviation

N Number of Samples ($N > 10$)

The glazing temperatures are very sensitive to indoor and outdoor boundary conditions and are not predicted very well. For better prediction of glazing temperatures more accurate formulae are recommended to predict heat transfer to indoor and outdoor ambient (Equations 3.9 and 3.10). The blind temperatures, however, depend strongly on the level of irradiation and convective heat transfer modelling from the slats and agree well between measurement and simulation.

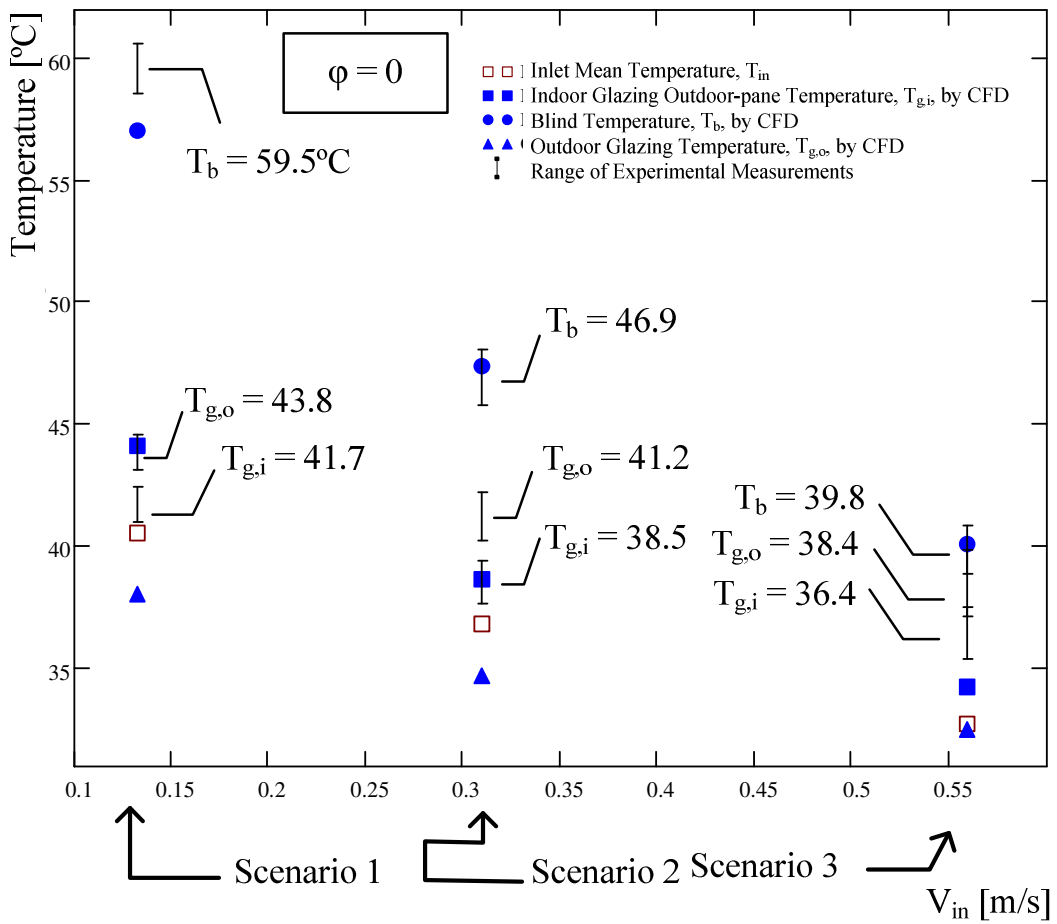


Figure 4.16: Experimental temperature readings and corresponding CFD predictions, $\phi = 0^\circ$.

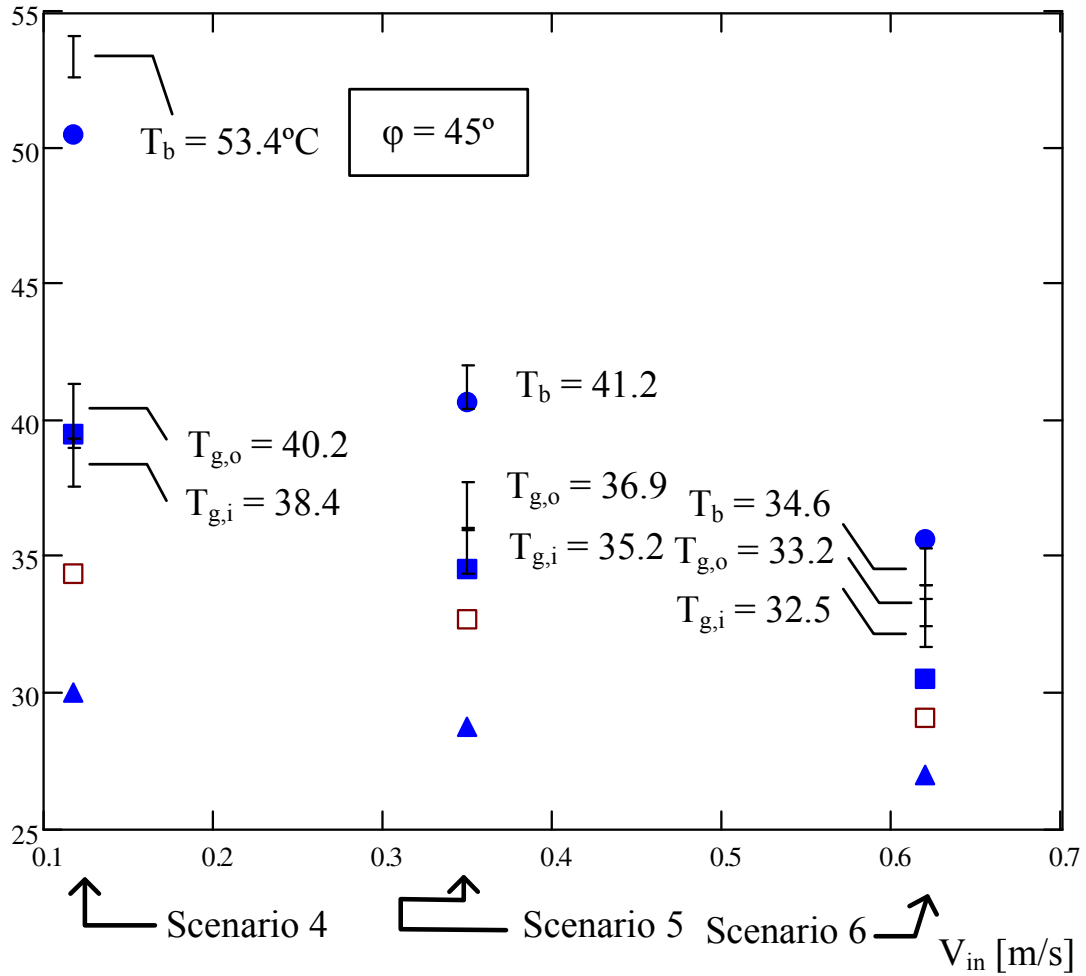


Figure 4.17: Experimental temperature readings and corresponding CFD predictions, $\phi = 45^\circ$.

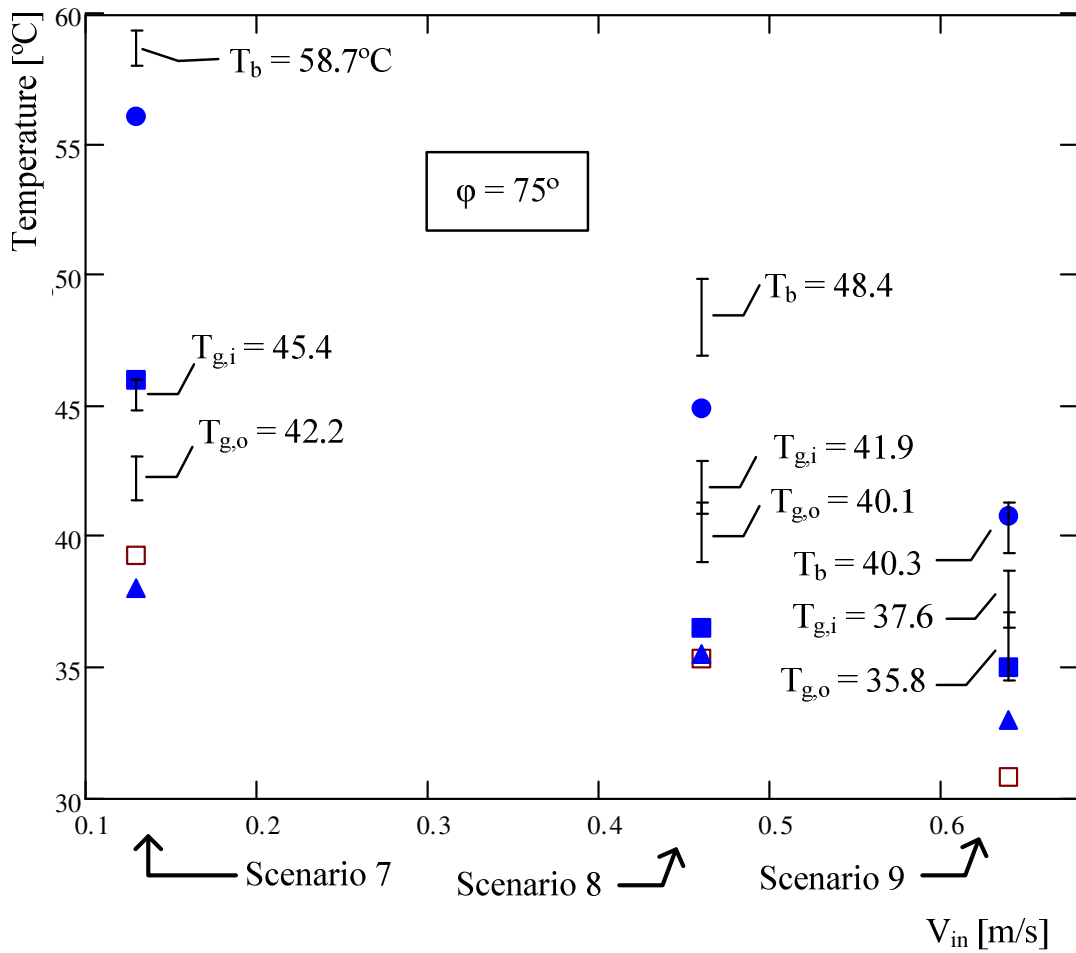


Figure 4.18: Experimental temperature readings and corresponding CFD predictions, $\phi = 75^\circ$.

4.8 RESULTS

Some experimental observations cannot be used for validation purposes, but they are worthwhile presenting here because they help understand the flow and understand the potential of the BIPV/T:

- The velocity field did not change much between slats 8 to 9 and 9 to 10. The streamwise velocity profiles at a section mid-height between slats 8 to 9 and 9 to 10 seemed to be similar (Figure 4.19). This suggests that although the height of the channel is only 0.5 m, the flow reaches fully periodically developed conditions quickly downstream of the inlet at all flow rates, at least at $\varphi = 0^\circ$.
- The temperature stratification along the glazings and the shading layer can be very large at times. The blind slats may sometimes cause some shading on parts of their neighboring slats, depending on φ and Ω . The blind layer slat surface temperatures can vary as much as 12.8 °C along the height and between shaded and unshaded spots (the blind slat solar normal-hemispherical reflectivity is 0.59 (Appendix 1)). The slat temperatures can vary by as much as 2–2.5 °C when measured on a single slat depending on whether the thermocouples are located in a shaded part or unshaded. The indoor glazing had a maximum temperature variation of about 5 °C, but the outdoor glazing temperatures were roughly uniform along the height. The channel air temperature can vary by as much as 5–6 °C from inlet to outlet, during low flow rate and high irradiation scenarios. An air temperature stratification of such magnitudes suggests that significant savings can be realized in winter heating using ventilated windows with between-the-panes shading devices.

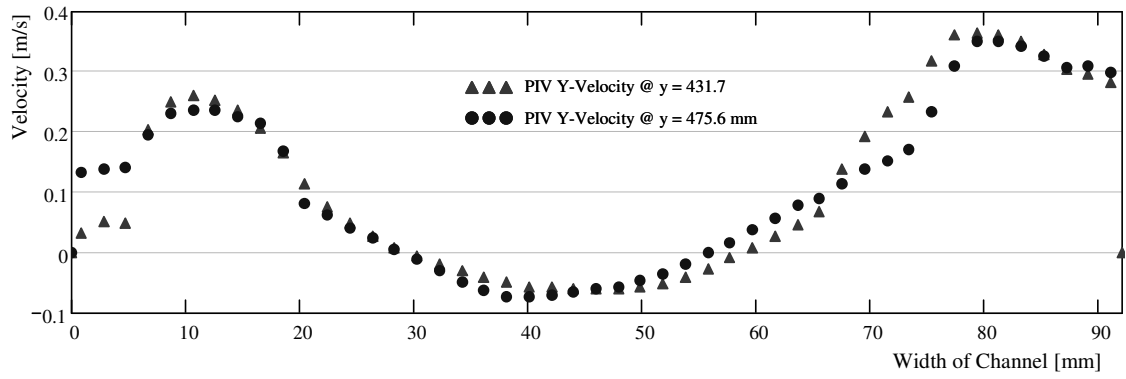


Figure 4.19: Streamwise velocity profile mid-height between slats 8 to 9, $y = 431.7$ mm, and 9 to 10, $y = 475.6$ mm.

CHAPTER 5

SIMPLIFIED APPROACH

Building on the numerical procedure described in chapter 3 and the experimental findings covered in Chapter 4, this chapter presents a simple 1–D model of the BIPV/T and its validation. For several reasons, a nodal-based 1–D model is a very useful tool for studying the thermal behaviour of BIPV/T systems. On the most fundamental level of thermal modeling, it is desirable to obtain an estimate of surface temperatures and heat fluxes across various components of the system. Knowledge of average surface temperatures and heat fluxes provides valuable information about the thermodynamics and gives valuable insight into the inner workings of this complex thermal system. On an optimization and design level, a 1–D model is particularly attractive because it provides average Convective Heat Transfer Coefficients, CHTCs, that can be easily integrated into building energy simulation software. Between-the-panes average CHTCs depend on the flow geometry, mean flow speed V_{in} , blind slat angle ϕ , and level of irradiation I_{tot} , and they contain enough information about the flow to provide a unique solution to a convective-based heat transfer problem. Once calculated and tabulated for various

geometries and flow conditions they can be easily input into a building energy simulation software package to optimize the performance of BIPV/T systems.

5.1 MODEL DESCRIPTION

Every glazing and shading layer is assigned one temperature node. There is one node assigned to the indoor and one assigned to the outdoor ambient air. The air inside the ventilated channel is assigned two temperature nodes, one on each side of the blind layer. Convective and long-wave radiative heat transfer is solved between various nodes. The 1-D model is based on the following assumptions (Figure 5.1):

- Isothermal surfaces,
- Steady-state conditions,
- Solar-thermal separation,
- Linearized radiation heat transfer, and
- Negligible edge-of-window effects.

The nodal temperatures are estimated, and then the nodal radiosities and heat transfer coefficients are calculated based on these estimations. The nodal (front and back) radiosities are J_{2f} , J_{2b} , J_{3f} , J_{3b} ... J_{5f} , and J_{5b} and are calculated from fundamental radiation equations. The heat transfer coefficients $h_{c,in}$, $h_{c,23}$, $h_{c,out}$, are calculated from appropriate correlations (Appendix 4). The long-wave radiation heat transfer is linearized and $h_{r,in}$, $h_{r,23}$, $h_{r,34}$, $h_{r,45}$ and $h_{r,out}$ are calculated based on the temperature estimations. The between-the-panes CHTCs, $h_{g,i}$, $h_{b,i}$, $h_{b,o}$, and $h_{g,o}$ must be provided to the 1-D model. An energy balance is performed at every node, and the resulting system of equations is solved to give the nodal temperatures.

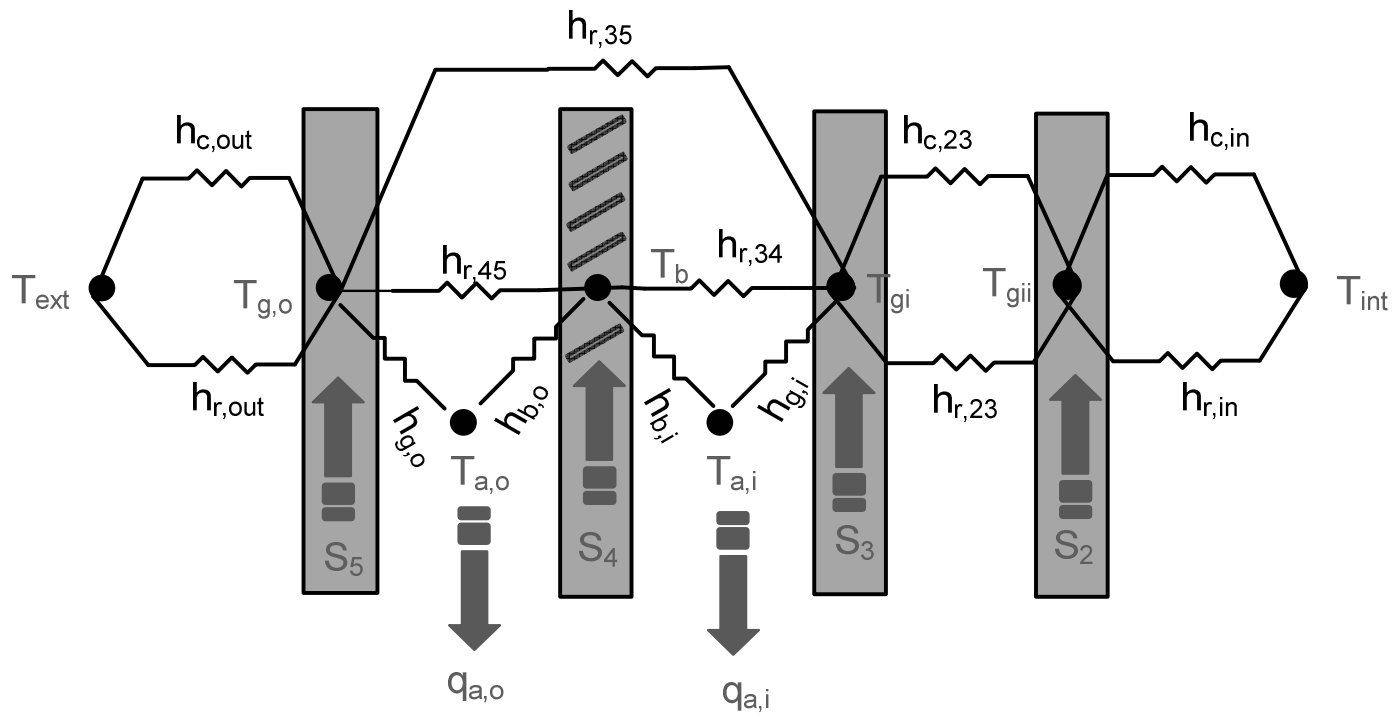


Figure 5.1: Thermal resistor network.

These new temperatures replace the initial estimations, and the solution procedure continues iteratively until convergence is achieved, at which point average surface temperatures, average heat transfer coefficients and average heat flux rates are known.

5.1.1 Long-wave Radiation Heat Transfer

A layer-based long-wave radiation analysis of a glazing arrangement is a straightforward task. Each node can communicate thermally only with its neighbouring nodes owing to the opaqueness of the material in the long-wave range. The radiation heat transfer between every two neighbouring nodes can be linearized and represented by a single radiative heat transfer coefficient. The radiation analysis is much more complex however, when a venetian blind layer is present in between a glazing arrangement. The venetian blind layer, due to its open-ness, acts effectively as a diathermanous layer allowing the glazing layers to “see” each other across the blind layer. Therefore, in addition to $h_{r,34}$ and $h_{r,45}$, $h_{r,35}$ is also required to complete the thermal resistor network inside the ventilated channel. Using front and back effective (including multiple inter-reflections and transmissions) reflectance, transmittance, and emittance of the glazing layers and the blind layer, a radiosity balance can be performed on the front and back side of every node to give $h_{r,34}$, $h_{r,45}$, and $h_{r,35}$ (Collins and Wright, 2004).

5.1.2 Between-the-panes Convective Heat Transfer Coefficients

Local “slat-to-slat” CHTCs can be defined, based on local heat flux rates, and used in a 2-D finite element model to give vertical variation of temperature along every layer.

Local heat flux rates can be obtained from CFD and integrated between every two consecutive blind slats (Figure 5.2):

$$h_{g,o} = \frac{q'_{g,o}}{s(T_{g,o} - T_{a,o})} \quad (5.1)$$

$$h_{b,o} = \frac{q'_{b,o}}{s(T_b - T_{a,o})} \quad (5.2)$$

$$q'_{b,o} = \int_0^{w_{eff}} \rho V q dx \Big|_{y=y_1} - \int_0^{w_{eff}} \rho V q dx \Big|_{y=y_2} - \int_{y_1}^{y_2} q'_{g,o} dy \Big|_{x=0} \quad (5.3)$$

where

$q'_{g,o}$ Outdoor Glazing wall heat transfer rate per unit length into paper, W/m

$q'_{b,o}$ Blind wall heat transfer rate per unit length into paper, W/m

T_b Average top and bottom slat surface temperature

q Enthalpy, J/kg

Local heat flux rate profiles from the glazing surfaces have a repeating fluctuating pattern because of the presence of the blind slats. Although local CHTCs are not calculated in this work local heat flux rate profiles are obtained and presented to illustrate the repeating fluctuating pattern. When the slat-tip-to-glazing distance is smallest, $\phi = 0^\circ$, and when maximum temperature gradients exists inside the system, 10 Hz fan setting, the fluctuations are most pronounced. Therefore scenario 1 is presented only (Figure 5.3).

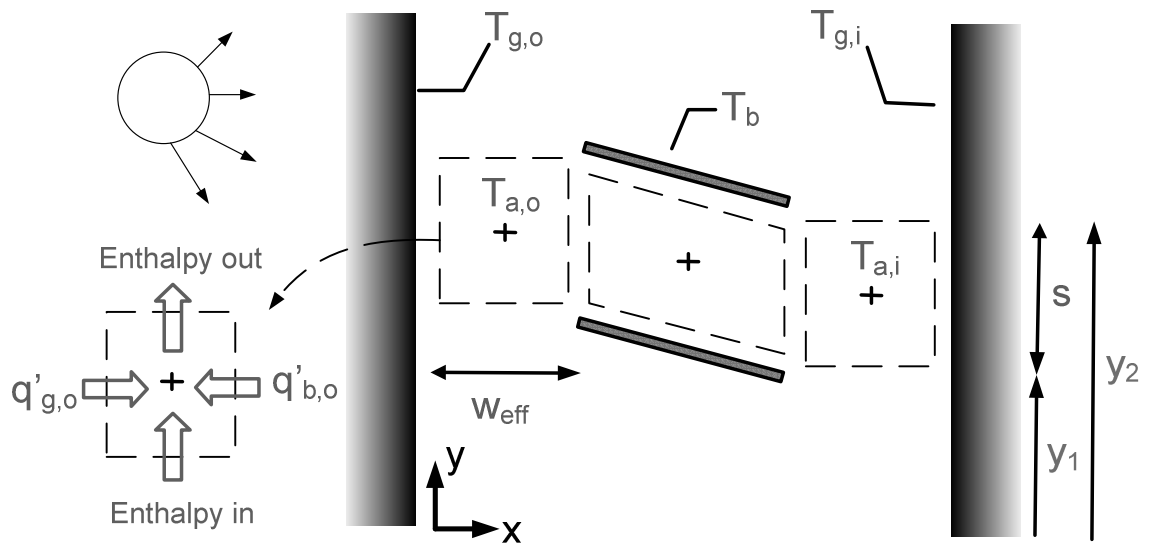


Figure 5.2: Local slat-to-slat energy balance and heat fluxes.

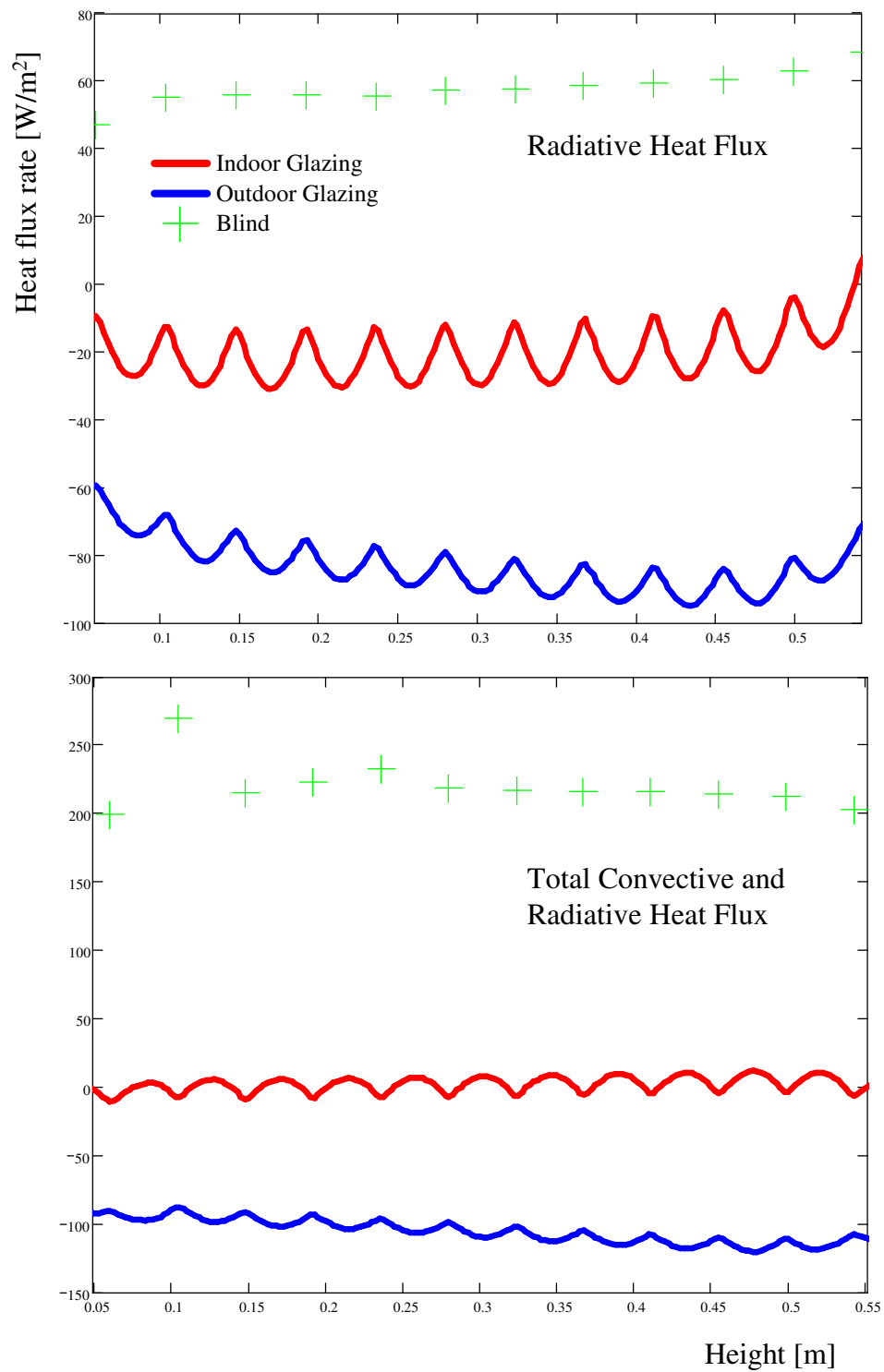


Figure 5.3: Vertical radiative and total heat transfer rate profiles, $\phi = 0^\circ$, 10 Hz.

Similar to local CHTCs, average CHTCs can be defined from average heat flux rates. The heat flux rate profiles can be integrated (averaged), in a similar manner, over the entire height of the window, H , instead of slat spacing, s .

The blind layer in the 1-D model is represented as a non-porous layer dividing the channel into two distinct sides and disallowing any heat transfer by mass motion across the blind layer (Figure 5.4). PIV results confirm that no apparent mass cross-over occurs through the blind slats, as discussed in Chapter 3. The two nodes, T_{ao} and T_{ai} , can communicate thermally with each other only through T_b . By carefully selecting four CHTCs, h_{go} , h_{bo} , h_{bi} and h_{gi} , the complex problem of between-the-panes convective heat transfer from fluid to three surfaces, T_{go} , T_b , and T_{gi} , can be solved. The blind layer is further represented as a uniform layer consistently through the solar-optical, long-wave, and thermal analysis. An effective area equal to the glazing areas is used in the analysis, in place of actual area available for heat transfer; i.e. slat surface area. The blind layer can be treated no differently than the glazing layers if appropriate effective radiative properties or appropriate heat transfer coefficients are used.

The between-the-panes average CHTCs are calculated and presented at $\varphi = 0$, 45 and 75°, and at various mean air speeds, V_{in} (Figure 5.5). At $\varphi = 0$, the CHTCs are the highest, and they tend to grow faster with increasing air flow rate than other φ . This is because at $\varphi = 0$ the blind slats impose a much larger obstruction to the flow and the flow attempts to make sharper turns around the tips of the slats.

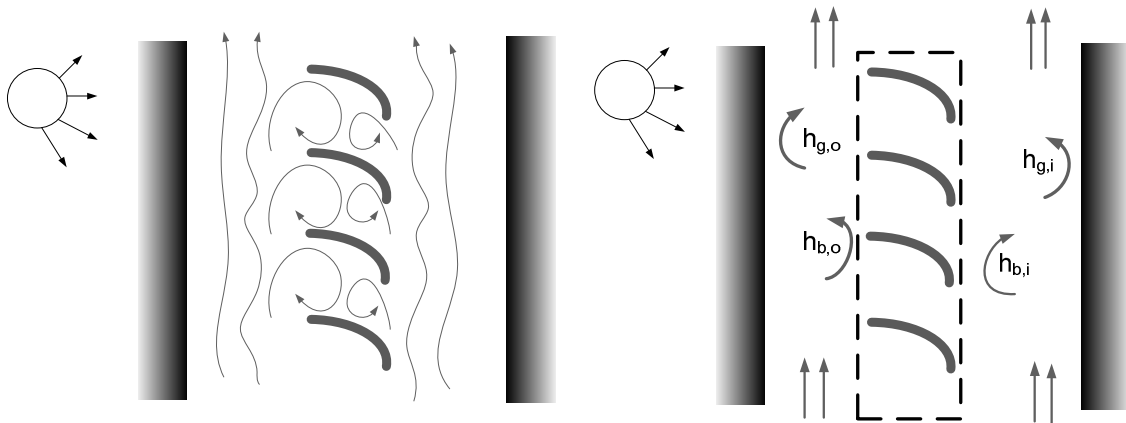


Figure 5.4: Actual air flow around blind slats on the left. Blind representation on the right.

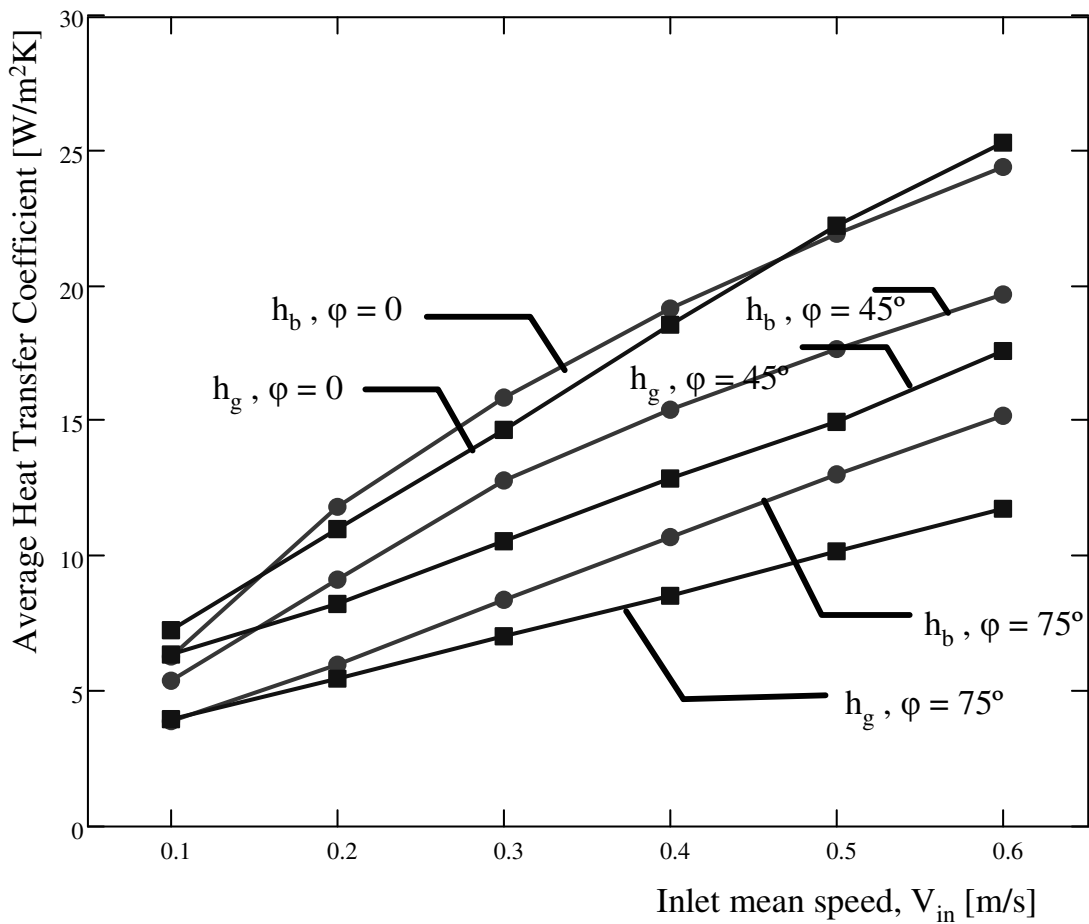


Figure 5.5: Average convective heat transfer coefficients.

5.2 MODEL VALIDATION

Between-the-panes average glazing and blind temperature predictions are compared with the CFD predictions and the experimental results at various V_{in} and ϕ (Figures 5.6–5.8). Similar to CFD predictions, blind layer temperature predictions are more accurate than glazing temperature predictions; however, the 1–D model predictions are always remarkably close to CFD predictions (usually within ± 1.5 °C). This suggests that although high vertical temperature stratifications exist the use of average temperatures for each layer may result in adequately accurate temperature and heat flux rate predictions. Therefore, the use of 1–D model may be justified.

5.3 PARAMETRIC ANALYSIS

Parametric analysis is a useful tool to understand a complex thermal system and help optimize its performance. In parameter analysis, first, a base scenario is defined with fixed inlet, solar and boundary conditions. Then the effect of varying these conditions on the thermal performance of is investigated. The air thermal gain, i.e., the heat transfer to the air per unit area of the window, can be used as an indication of the system performance.

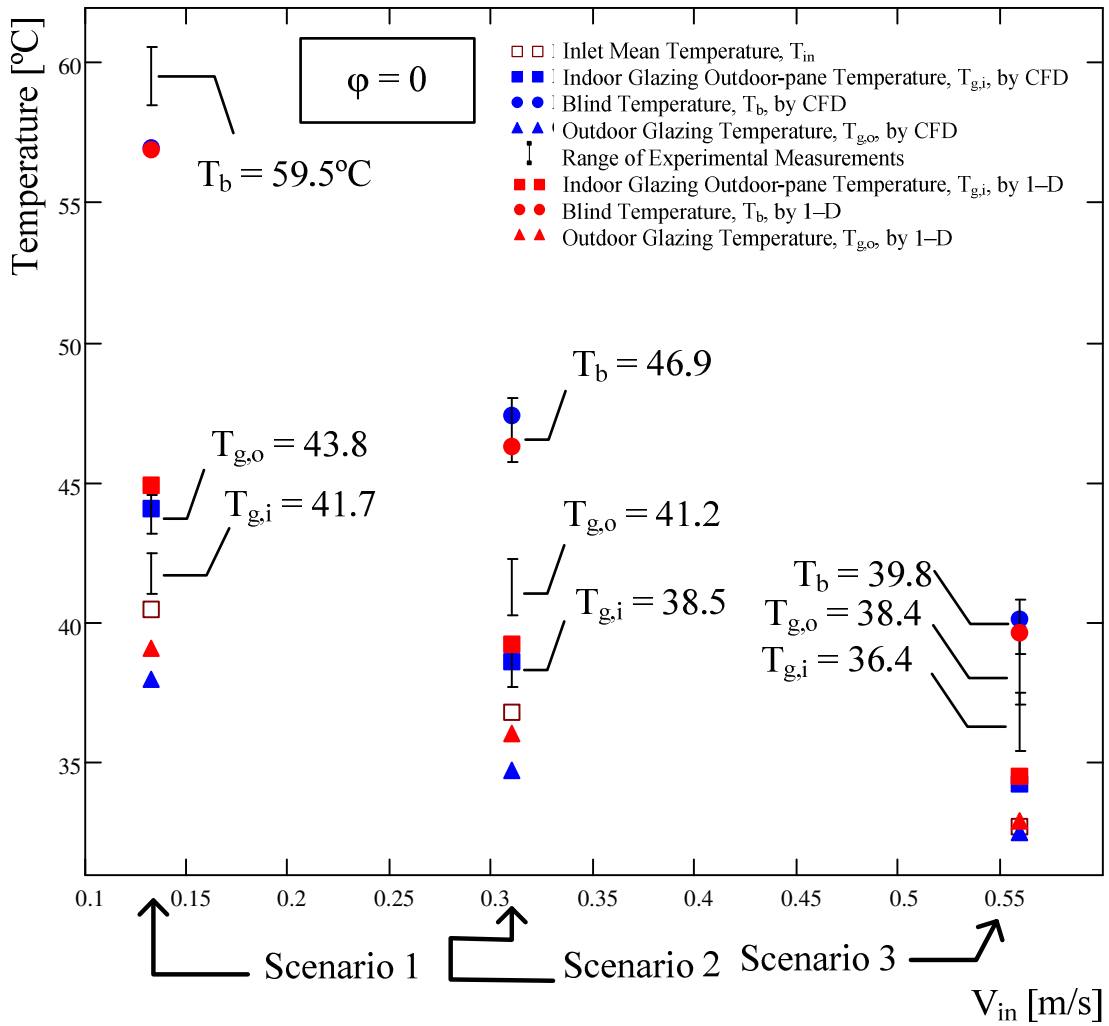


Figure 5.6: 1-D and CFD temperature predictions against experimental readings, Scenarios 1, 2 and 3, $\phi = 0$, $I_{tot} = 680 \text{ W/m}^2$, $T_{int} = 22.8^\circ\text{C}$, $T_{ext} = 13.0^\circ\text{C}$.

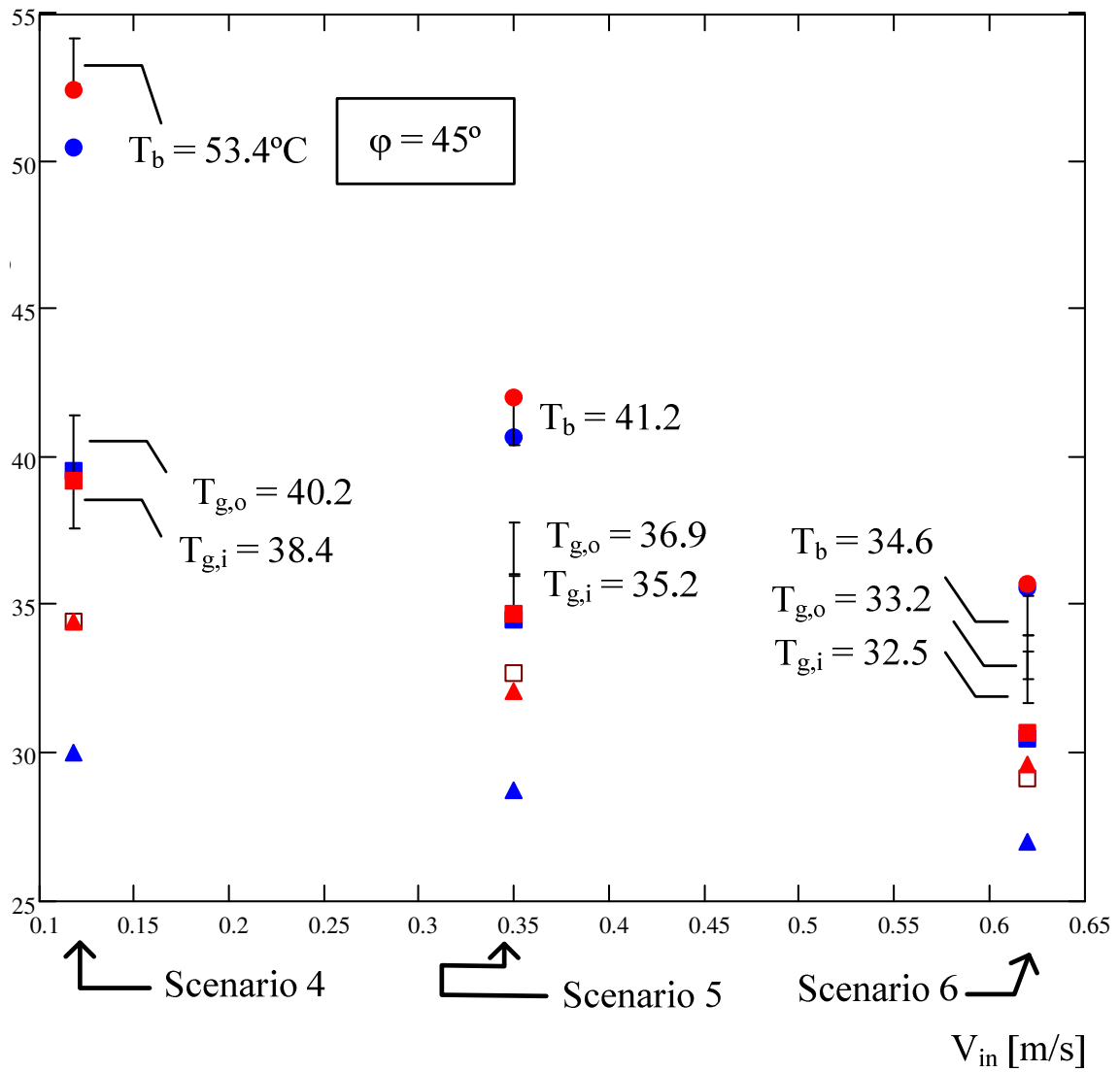


Figure 5.7: 1-D and CFD temperature predictions against experimental readings, Scenarios 4, 5, and 6, $\phi = 45^\circ$, $I_{tot} = 650 \text{ W/m}^2$, $T_{int} = 22.0^\circ\text{C}$, $T_{ext} = 10.8^\circ\text{C}$.

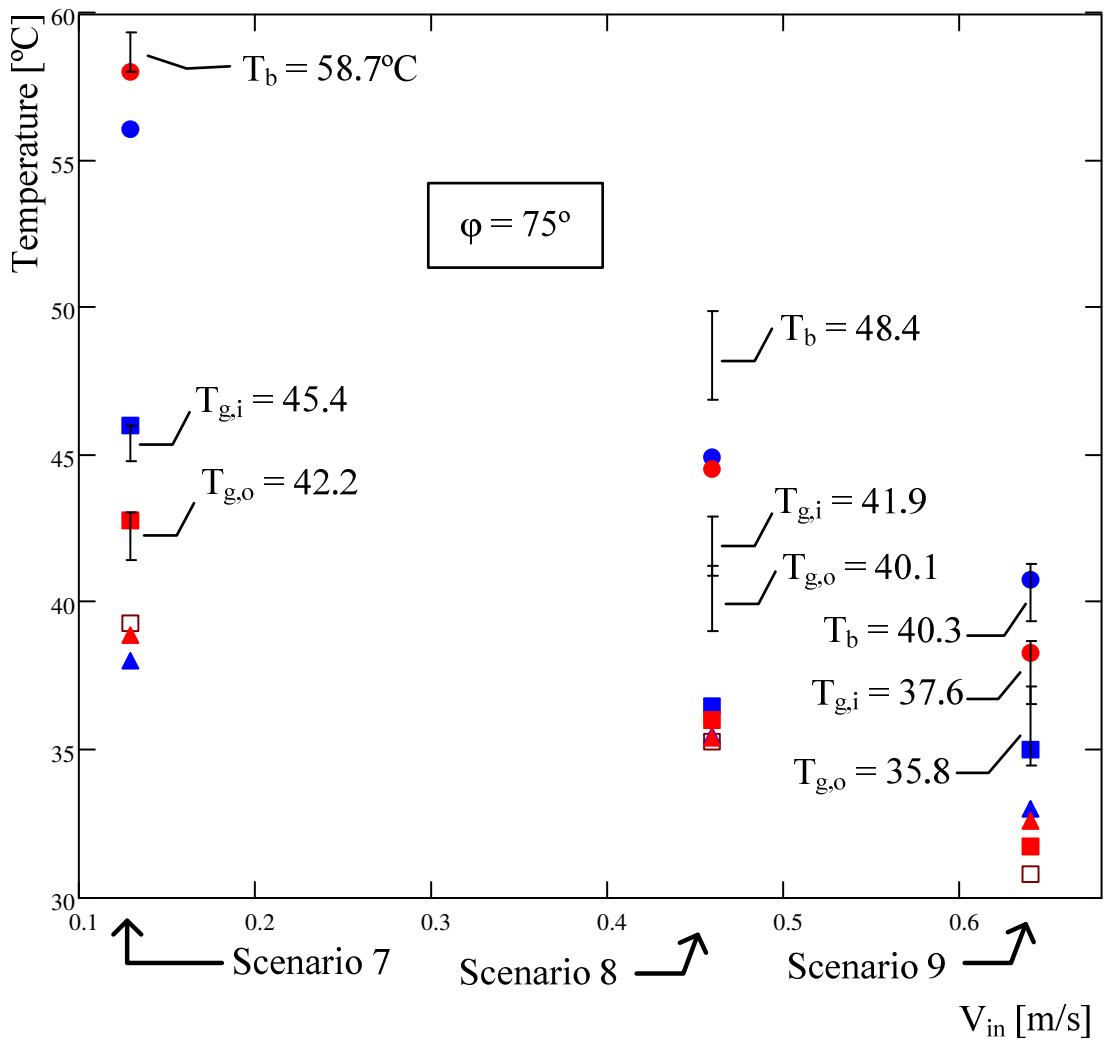


Figure 5.8: 1-D and CFD temperature predictions compared with experimental readings, Scenarios 7, 8 and 9, $\phi = 75^\circ$, $I_{tot} = 692$ W/m², $T_{int} = 22.2$ °C, $T_{ext} = 13.1$ °C.

The 1-D model can be conveniently used to perform parametric analysis. The model must, however, be used in conjunction with a 1-D model of the lower (PV) section of the BIPV/T to be able to represent the entire system at once, not just the upper (vision and shading) section. Although optimization is beyond the scope of this work, and although the 1-D model must preferably be integrated with a model of the lower section before it can be used, it is useful however to show what the model is capable of doing.

The parameters in the base scenario are: $h_{c,out} = 5 \text{ W/m}^2\text{-K}$, $T_{ext} = 0^\circ\text{C}$, $h_{c,in} = 3 \text{ W/m}^2\text{-K}$, $T_{int} = 20^\circ\text{C}$, $V_{in} = 0.3 \text{ m/s}$, $T_{in} = 25^\circ\text{C}$, $I_b = 600 \text{ W/m}^2$, $I_d = 0 \text{ W/m}^2$, $\phi = 0^\circ$, $\Omega = 45^\circ$. The effect of varying I_b , $h_{c,out}$, $h_{c,in}$, V_{in} , T_{in} , and ϕ on the air thermal gain, q_{air} , is shown in Figures 5.9–5.10.

The effect of I_b on q_{air} is significant, as expected. The effect of $h_{c,out}$ is also significant, but the effect of $h_{c,in}$ is minimal; Therefore, the heat transfer from the outdoor pane (to the channel air) is more significantly influenced by $h_{c,out}$ than is the heat transfer from the indoor double-glazing unit influence by $h_{c,in}$. V_{in} and T_{in} have a strong influence on q_{air} , but they are interdependent. So they must not be examined separately. They are however presented separately here to demonstrate the methodology. The effect of ϕ on q_{air} is somewhat significant because ϕ affects the heat transfer coefficients inside the channel and also alters the distribution of solar fluxes.

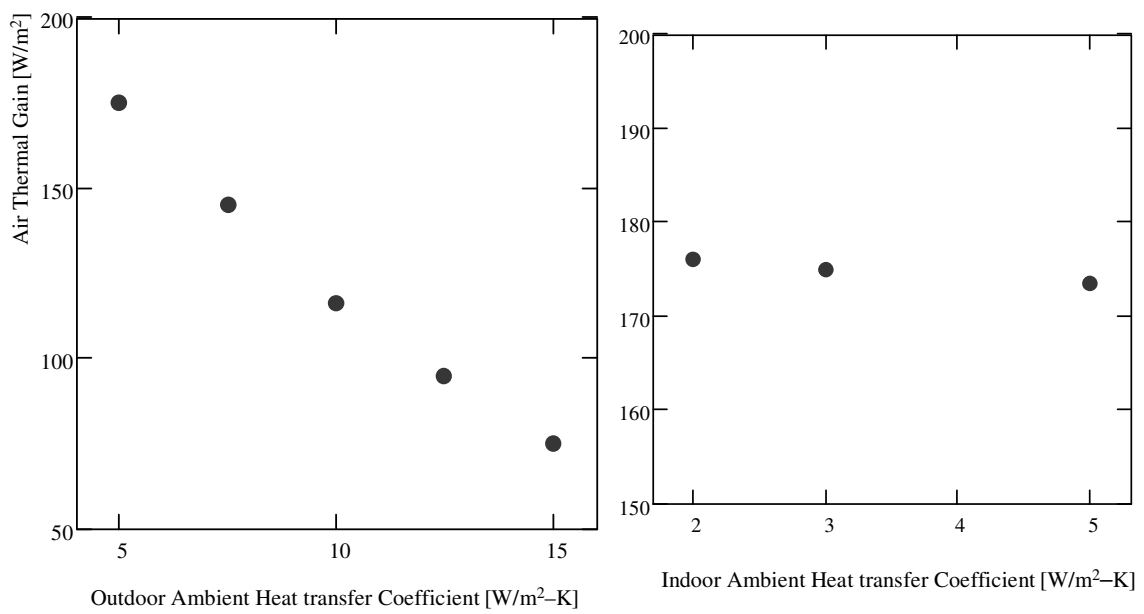


Figure 5.9: q_{air} vs. $h_{c,in}$ and $h_{c,out}$

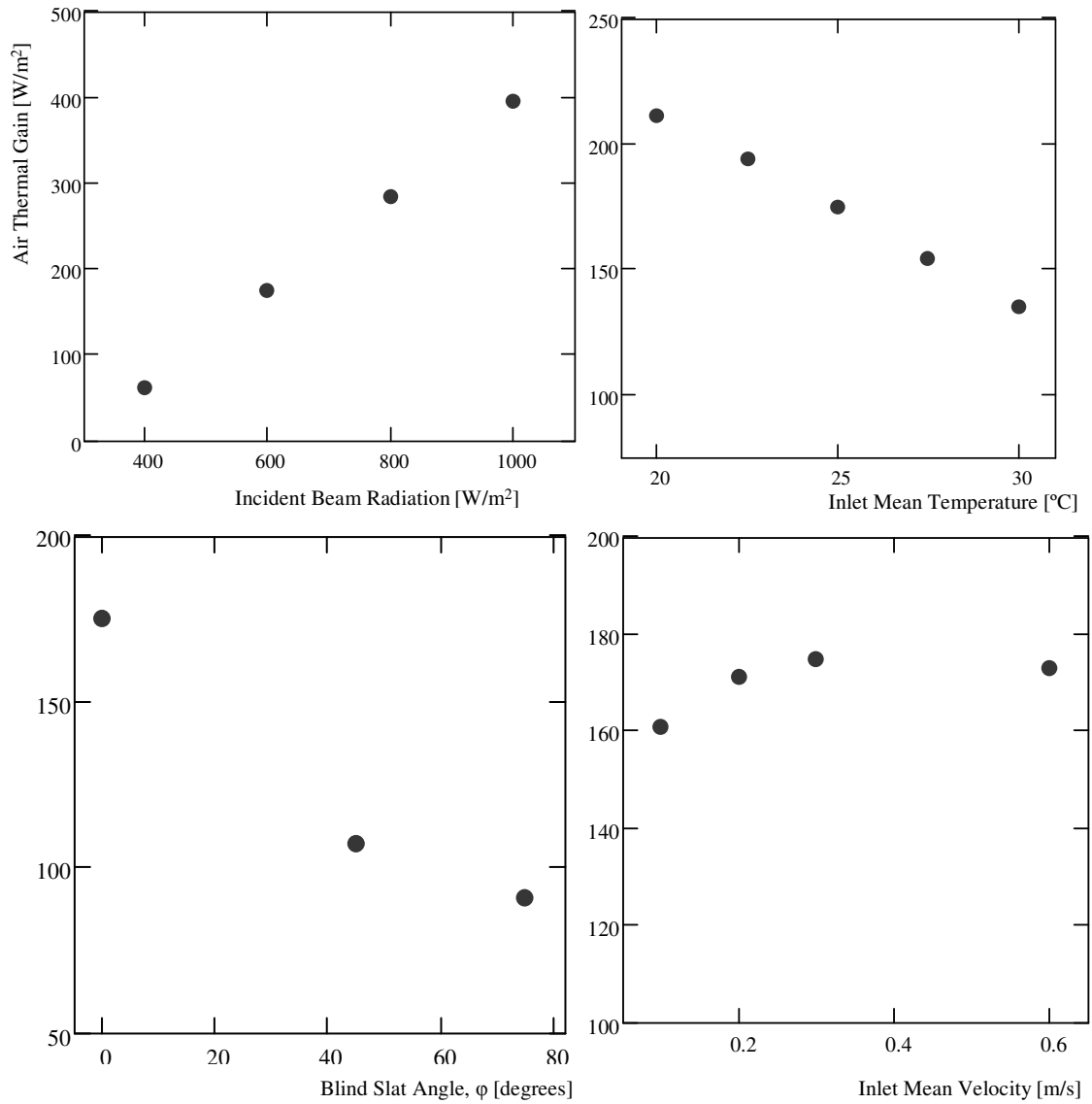


Figure 5.10: q_{air} vs. I_b , V_{in} , T_{in} , and ϕ

5.4 SOLAR AND THERMAL GAINS

The solar and thermal heat fluxes that reach the interior space are referred to as the gains of the system. These heat fluxes are especially important because they reflect on the building occupant's thermal comfort and together they determine the thermal performance of the BIPV/T:

- The transmitted solar flux, I_{tra} ,
- The convective and radiative heat flux from the inner-most pane to the indoor environment, q_{in} , and
- The air thermal gain, q_{air} .

I_{tra} , q_{in} , and q_{air} have been estimated and presented for all nine scenarios using the 1-D model (Figure 5.11). The transmitted solar flux, I_{tra} , is highest at $\phi = 0^\circ$ and lowest at $\phi = 75^\circ$ because of minimum and maximum solar blockage, respectively. The direction of indoor-flowing convective and radiative heat transfer, q_{in} , is usually from the inner-most pane to the indoor environment, not the other way around. Therefore, the center-window heat transmission is usually in the form of gains, not losses. This is because the lower PV panel preheats the air substantially (air entering the window is warmer than the exterior air and usually warmer than even the interior air) and also because the blind slats have a large area available for solar absorption (slat width is 49 mm). By increasing the air flow rate the surface temperatures tend more towards the outdoor ambient temperature, and therefore the magnitude of indoor-flowing convective and radiative heat fluxes fall. The air thermal gain, q_{air} , or the change of enthalpy of air, is due to absorbed solar radiation and recovery of a portion of transmission gains (or losses). By increasing the air flow rate the convective heat transfer inside the channel is

significantly enhanced, at all ϕ . Therefore, a higher portion of absorbed solar radiation is removed by the air, instead of flowing to the outdoor or indoor environment. The air thermal gains are so high compared to solar transmission and center-window thermal transmission gains and they are so significantly enhanced by increasing the air flow rate that it may be practical to increase the flow rate to achieve higher overall gains, despite lower transmission gains (or higher transmission losses) and higher fan pressure drop losses.

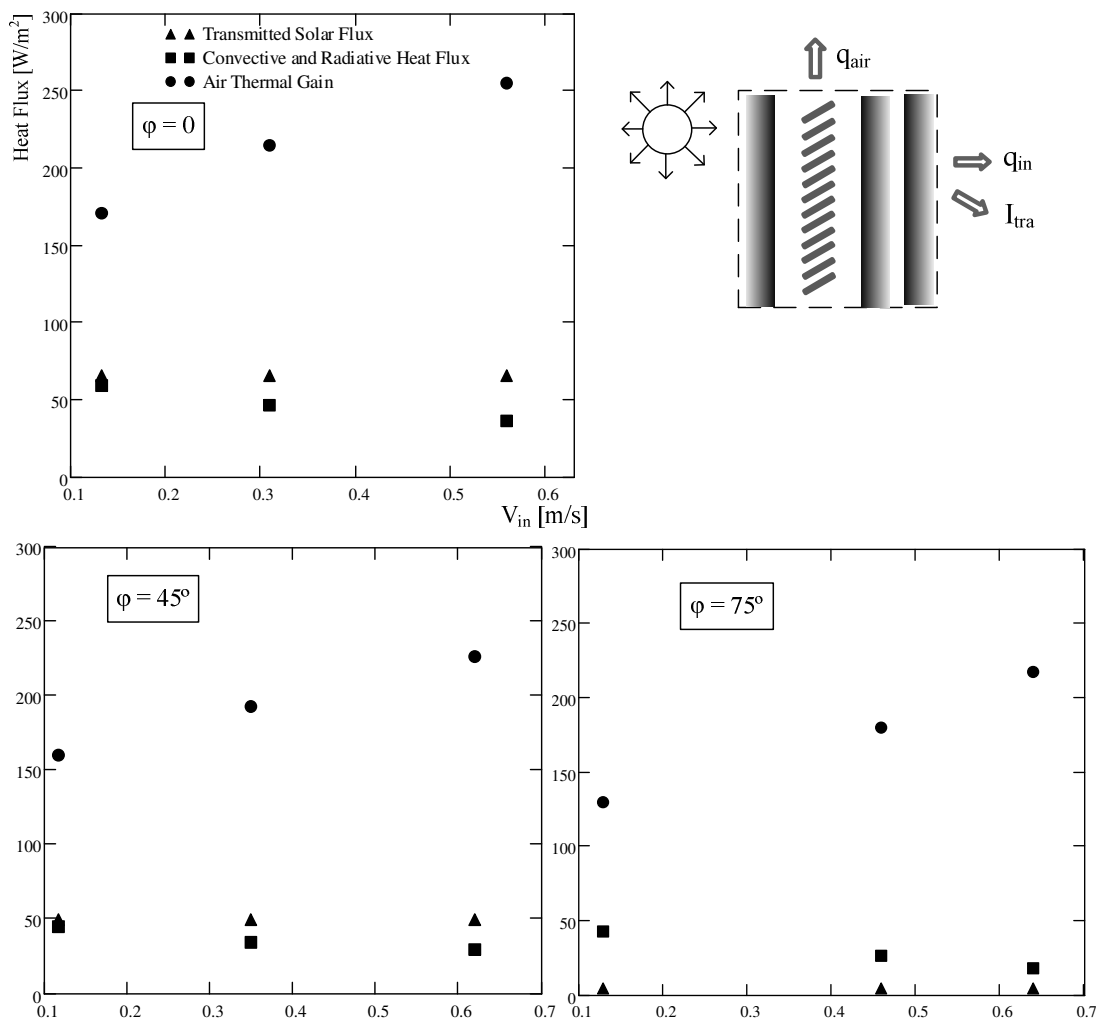


Figure 5.11: Solar and thermal Gains

CHAPTER 6

CONCLUSIONS

An overview of the experimental and numerical results for a BIPV/T system was presented. Solar-optical and CFD models were developed at three blind slat angles, $\varphi = 0, 45, \text{ and } 75^\circ$, and three fan speed settings, 10, 20 and 30 Hz, to predict the fluid flow and heat transfer inside the system. The velocity field was validated using PIV measurements. The general shape of the velocity field and the streamwise velocity profile at a horizontal section agreed with experimental results. The blind surface temperature was validated using thermocouple measurements. Between-the-panes convective heat transfer coefficients were obtained at various φ and used in a 1-D model to predict average surface temperatures. The 1-D model predicts average glazing and blind surface temperatures to within, usually, $\pm 1.5^\circ\text{C}$ of the CFD simulation. The following observations were made:

- PIV measurements at $\varphi = 0$ showed great similarity in the velocity field at all practical fan speed settings (practical flow rates). The flow was split into two main streams by the blind layer. The fluid velocity was high on the sides of the

blind layer. Between the blind slats the flow was unsteady, but two slow-moving counter-rotating vortices were often observed.

- The velocity field reached fully periodically developed conditions downstream of the inlet in that the same velocity vector map between every two blind slats repeated itself.
- Large temperature stratifications were observed along the glazing and the shading layers. The shading layer temperatures could vary by as much as 12.8 °C from top to bottom. The air temperature difference between inlet and outlet can reach as high as 5–6 °C at high irradiation and low fan speed settings. An air temperature rise of such magnitudes can bring significant savings to the energy bill of the building.
- In general, the glazing and shading surface temperatures were predicted well by the CFD and 1–D models. The glazing temperatures were very sensitive to indoor and outdoor heat transfer modeling. It is recommended that more accurate indoor and outdoor heat transfer models be used to give more accurate glazing temperature predictions. Comparing the CFD and the 1–D model their results were always very close to each other.

- Between-the-panes convective heat transfer coefficients were significantly affected by the fan speed settings. Mechanical ventilation enhanced the convective heat transfer inside the channel significantly at all ϕ .
- The air thermal gains increased very significantly by increasing the fan speed setting while the transmission gains through the window decreased minimally. Air thermal gains were much larger than the transmission gains and they increased so significantly with increasing the flow rate that it may be practical to increase the flow rate to achieve better overall gains.

REFERENCES

Adrian, R. J., 1997, Dynamic Ranges of Velocity and Spatial Resolution of Particle Image Velocimetry, *J. Meas. Sci. Technol.*, Vol. 8, pp. 1393-1398.

ASHRAE, 2005, 2005 Handbook of Fundamentals, Chapter 31.

ASTM E891, 1987, Standard Tables for Terrestrial Direct Normal Solar Spectral Irradiances for Air Mass 1.5, Annual Book of ASTM Standards.

Balocco, C. and Colombari, M., 2006, Thermal Behaviour of Interactive Mechanically Ventilated Double Glazed Facades: Non-dimensional Analysis, *J. Energy and Buildings*, Vol. 38, January, pp. 1-7.

Balocco, C., 2002, A Simple Model to Study Ventilated Energy Performance, *J. Energy and Buildings*, Vol. 34, June, pp. 469-475.

Brinkworth, B.J., 2002, Coupling of Convective and Radiative Heat Transfer in PV Cooling Ducts, *Transactions of the ASME*, 124, pp. 250-255.

Chen, Q., 1995, Comparison of Different k- ϵ models for indoor air flow computations, *Numerical Heat Transfer, Part B*, Vol. 28, pp. 353-369.

Charron, R., and A.K. Athienitis, 2006, A Two Dimensional Model of a Double Façade with Integrated Photovoltaic Panels, *ASME Journal of Solar Energy Engineering*, Vol. 128, pp. 160-167.

Compagno, A., 2005, From Double Windows to Double Building Envelopes, http://www.compagno.ch/EN/Vortrag_EN_rosenheim.htm, Last Visited: Feb, 2009.

Duffie, J.A., and W.A. Beckman, 1991, *Solar Engineering of Thermal Processes*. 2nd ed., Wiley Publishers.

- Davis, M.W., Hunter, F.A., and Dougherty, B.P., 2001, Predictions of Building Integrated Photovoltaic Cell Temperatures, *J. Solar Energy Engineering*, Vol. 123, August, pp. 200-210.
- Edwards, D.K., 1977, Solar Absorption by Each Element in an absorber-coverglass array, *J. Solar Energy*, Vol. 1, Issue 4, pp. 401-402.
- FlowManager Manual, 2002, Dantec Dynamics A/S, Tonsbakken, Denmark.
- FLUENT. 2005. FLUENT 6.3 Manual.
- Garnet, J.M., 1999, Thermal Performance of Windows with Inter-pane Venetian Blinds, Masters Thesis, University of Waterloo, Waterloo, Canada.
- Gratia, E. and De Herde, A., 2004, Natural Ventilation in a Double-Skin Facade, *J. Energy and Buildings*, Vol. 36, February, pp. 137-146.
- Hollands, K.G.T., 2004, Thermal Radiation Fundamentals, Begell House Inc., New York, USA.
- Hollands, K.G.T., Wright, J.L., Granqvist, C.G., 2001, Solar Energy – The state of the Art, ISES position papers, James and James Ltd. Ch. 2 (Glazings and Coatings), pp. 29-107.
- Hadlock, C., 2006, Modelling and Optimization of an Air Flow Window with Between-the-panes Shading Device, Masters thesis, University of Waterloo, Waterloo, Canada.
- Infield, D., Mei, L. and Eicker, U., 2004, Thermal Performance Estimation for Ventilated PV Facades, *J. Solar Energy*, Vol. 76, pp. 93-98.
- Ismail, K.A.R., and Henriquez, J.R., 2006, Simplified Model for a Ventilated Glass Window under Forced Air Flow Conditions, *Applied Thermal Engineering*, Vol. 26, pp. 295-302.
- Keane, R.D., Adrian, R.J., and J. Zhang, 1995, Super-resolution Particle Image Velocimetry, *Meas. Sci. Techno.*, Vol. 6, pp 754-768.
- Kim, S.E., Choudhury D., and B. Patel. 1997, Computations of Complex Turbulent Flows using the Commercial Code FLUENT, Proceedings of the ICASE/LaRC/AFOSR Symposium on Modeling Complex Turbulent Flows, Hampton, VA.
- Kotey, N.A., and J.L. Wright. 2006. Simplified Solar-optical effective properties of a Venetian Blind. Proceedings of SESCO Conference, Aug 21-24, Montreal, Ontario, Canada.

Liao, L., 2005, Numerical and Experimental Investigation of Building Integrated Photovoltaic-Thermal Systems, MASc Thesis, Concordia University, Montreal, Quebec, Canada.

Liao, L., A.K. Athienitis, L. Candanedo, K.W. Park, Y. Poissant, and M. Collins, 2007, Numerical and Experimental Study of Heat Transfer in a BIPV-thermal System. ASME Journal of Solar Energy Engineering, Vol. 129, Nov., pp. 423-430

Limb, N., 2002, Low-E Growth – Slow, But Definitely Not Low, USGlass Magazine, Vol 37, Issue 8, August.

Manz, H., 2004, Total Solar Energy Transmittance of Glass Double Facades with Free Convection, J. Energy and Buildings, Vol. 36, February, pp. 127-136.

Mei, L., Infield, D., Eicker, U. and Flux, V., 2003, Thermal Modelling of a Building with an Integrated Ventilated PV Facade, J. Energy and Buildings, Vol. 35, July, pp. 605-617.

Mootz, F., and Bezia, J.J., 1996, Numerical Study of a Ventilated Façade Panel, Solar Energy, Vol. 57, No. 1, pp. 29-36.

Moshfegh, B., and Sandberg, M., 1996, Investigation of Fluid Flow and Heat Transfer In a Vertical Channel Heated From One Side by PV Elements, Part I-Numerical Study, WREC 1996, pp. 248-253.

NRCan, 2008, Commercial/Institutional End-Use Model, Office of energy efficiency, Natural Resources Canada, Ottawa, September.

Posner, J.D., Buchanan, C.R., and Dunn-Rankin, D., 2003, Measurement and prediction of indoor air flow in a model room. J. of Energy and Building. Vol. 35 (50), pp. 515-526.

Rheault, S. and Bilgen, E., 1990, Experimental Study of Full-Size Automated Venetian Blind Windows, *J. Solar Energy*, Vol. 44, pp. 157-160.

Rodrigues, A. M., Canha da Piedade, A., Lahellec A., and Grandpeix, J.Y., 2000, Modelling natural convection in a heated vertical channel for room ventilation, J. Building and Environment, Vol. 35, pp. 455-469.

Safer, N., Woloszyn, M. and Roux, J.J., 2005. Three-dimensional simulation with a CFD tool of the airflow phenomena in single floor double-skin façade equipped with a Venetian blind, J. Solar Energy, Vol. 79, pp. 193-203.

Saelens, D., 2002, Energy Performance Assessment of Multiple-skin facades, Ph.D. thesis, Laboratory for Building Physics, Katholieke Universiteit Leuven, Belgium.

Santamouris, M., 2001, Solar and Natural Resources for a Better Efficiency in the Built Environment, Solar Energy – The State of the Art, ISES position papers, Ch. 1, James and James Ltd. pp. 1-22.

Shih, T.H., Liou, W.W., Shabbir, A., Yang, Z., Zhu, J. 1995. A New Eddy Viscosity Model for High Reynolds' Number Turbulence Flows. *Compt. Fluids* 24(3) 227-238.

Siegel, R., and Howell, J.R., 2002, Thermal Radiation Heat Transfer, 4th edition, Taylor & Francis, New York, USA.

Tasnim, S., and Collins, M., 2004, Laminar Natural Convection Heat Transfer in Windows with Between-the-panes Venetian Blinds, Proceedings of Solar Energy Society of Canada Inc., August 21-25, Waterloo, Ontario, Canada.

Tasnim, S., 2004, Numerical Analysis of Convective Heat Transfer for Horizontal, Between-the-panes Louvered Blinds, Masters Thesis, University of Waterloo, Waterloo, Canada.

TRNSYS, 2005, A TRAnSient SYstems Simulation program, <http://sel.me.wisc.edu/trnsys>, The Solar Energy Laboratory, University of Wisconsin-Madison, , Last Updated: Nov 2006, Last Visited Feb 2009.

Trombe, F., Robert, J. F., Cabanat, M., and Sesolis, B., 1977, Concrete Walls to Collect and Hold Heat, *Solar Age*, Vol. 2, No. 8, pp. 13-19.

Wigginton and McCarthy, 2000, Environmental Second Skin Systems, <http://www.battlemccarthy.com/Double%20Skin%20Website/index.htm>, June 1st, Last visited Dec 2008.

Wright, J.L., and N.A. Kotey. 2006, Solar Absorption by Each Element in a Glazing/Shading Layer Array. *ASHRAE Transactions*, Vol 112, Part 2.

Ye, P., Harrison, S.J., and Oosthuizen, P.H., 1999, Convective Heat Transfer from a Window with a Venetian Blind: Detailed Modelling, *ASHRAE Transactions*, Vol. 105, SE-99-15-03, pp. 1031-1037.

Zollner, A., Winter, E.R.F., and Viskanta, R., 2002, Experimental Studies of Combined Heat Transfer in Turbulent Mixed Convection Fluid Flows in Double-skin-facades, *International Journal of Heat and Mass Transfer*, 45, pp. 4401-4408.

APPENDIX 1

SOLAR OPTICAL AND LONG-WAVE MEASUREMENTS OF THE BLIND SLAT

The spectral solar normal-hemispherical reflectivity of the venetian blind slat surface was measured by the CARY5000 spectrophotometer (Fig A1.1). The CARY5000 is a dual-beam spectrophotometer with a built-in integrating sphere. An integrating sphere is a hollow sphere with a uniformly highly reflective inner surface. The reflectivity of a given sample was measured in comparison to the reflectivity of a reference sample. The measurement range was from 250 to 2500 nm. The standard 50-point ordinate method (ASTM E891, 1987) was used to spectrally average the reflectivities and give a total normal-hemispherical reflectivity of 0.59.

The long-wave normal emissivity of the blind slat surface was measured to be about 0.76 on the front and the back side by SOC400. The measurements were made for surface temperatures ranging from 275 to 235 K (Figure A1.2). The SOC400 is a portable handheld Fourier Transform Infrared Reflectometer (FTIR) with an operating range of 2 to 25 μm and a reflectance repeatability of 1%. The hemispherical emissivity

was equal to the normal emissivity multiplied by a factor of 0.96 for a dielectric surface;
i.e. painted aluminum slats (Hollands, 2004):

$$\varepsilon(T_s) = \varepsilon_n(T_s) (\varepsilon_\lambda / \varepsilon_n) \tag{A1.1}$$

and $(\varepsilon_\lambda / \varepsilon_n) \approx 0.96$ at ε_n

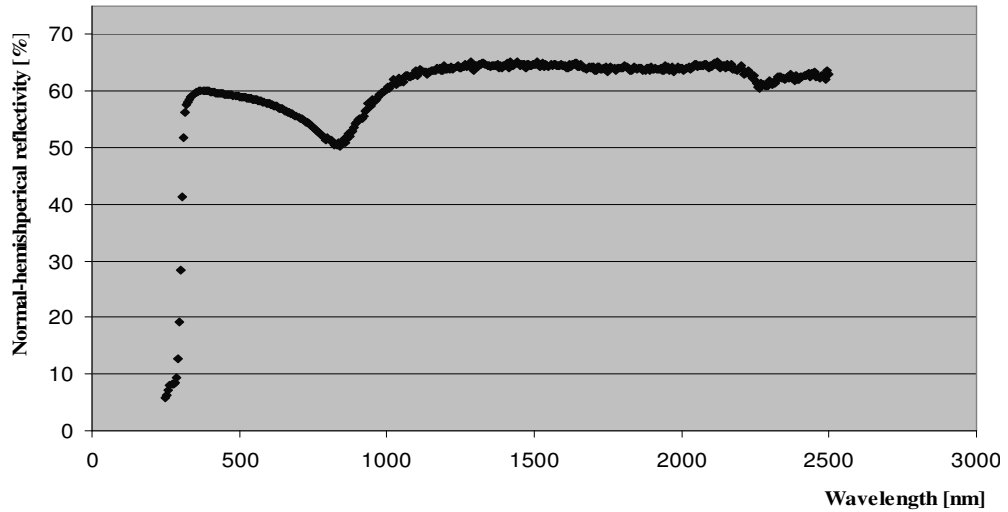


Figure A1.1 – Spectral normal-hemispherical solar reflectivity of the blind slat.

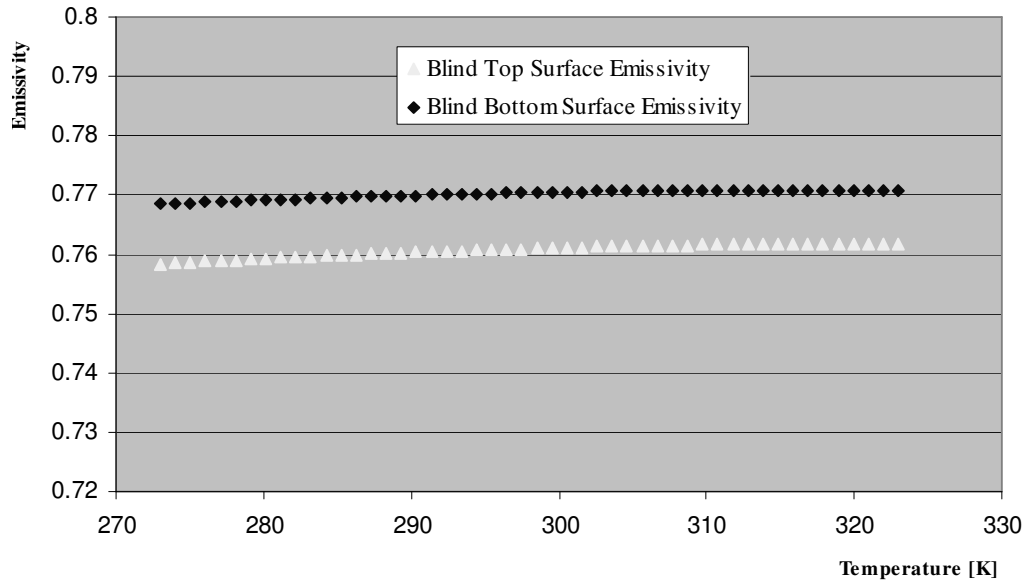


Figure A1.2 – The long-wave emissivity of the blind slat.

APPENDIX 2

THE VENETIAN BLIND MODEL

ORIGIN := 1

Daylight_Saving_Reversed_Time := 0

n := 8·30 + 22

$$\phi := 0 \cdot \frac{\pi}{180}$$

$\rho := 0.59$

Itot := 700

Ieppley := 900

$$\delta := 23.45 \cdot \sin \left[\left(360 \cdot \frac{284 + n}{365} \right) \cdot \frac{\pi}{180} \right]$$

$\delta = 0.605$

$\Phi := 45$

$$B := (n - 1) \cdot \frac{360}{365}$$

$$E := 229.2 \cdot \left(\begin{array}{l} 0.000075 + 0.001868 \cdot \cos \left(B \cdot \frac{\pi}{180} \right) - 0.032077 \cdot \sin \left(B \cdot \frac{\pi}{180} \right) \dots \\ + -0.014615 \cdot \cos \left(2 \cdot B \cdot \frac{\pi}{180} \right) - 0.04089 \cdot \sin \left(2 \cdot B \cdot \frac{\pi}{180} \right) \end{array} \right)$$

$E = 6.149$

Solar_Time := Daylight_Saving_Reversed_Time + 4·(75 - 74) + E

Solar_Time = 10.149

$$\omega := \frac{\text{Solar_Time}}{60} \cdot 15 \quad \omega = 2.537$$

$$\theta_z := \frac{180}{\pi} \left(\text{acos} \left(\cos \left(\Phi \cdot \frac{\pi}{180} \right) \cdot \cos \left(\delta \cdot \frac{\pi}{180} \right) \cdot \cos \left(\omega \cdot \frac{\pi}{180} \right) + \sin \left(\Phi \cdot \frac{\pi}{180} \right) \cdot \sin \left(\delta \cdot \frac{\pi}{180} \right) \right) \right)$$

$$\theta_z = 44.451$$

$$\alpha_s := 90 - \theta_z \quad \alpha_s = 45.549$$

$$\gamma_s := (\text{sign}(\omega)) \cdot \left| \frac{180}{\pi} \cdot \text{acos} \left(\frac{\cos \left(\theta_z \cdot \frac{\pi}{180} \right) \cdot \sin \left(\Phi \cdot \frac{\pi}{180} \right) - \sin \left(\delta \cdot \frac{\pi}{180} \right)}{\sin \left(\theta_z \cdot \frac{\pi}{180} \right) \cdot \cos \left(\Phi \cdot \frac{\pi}{180} \right)} \right) \right|$$

$$\gamma_s = 3.624$$

$$\theta_{\text{inc}} := \frac{180}{\pi} \cdot \text{acos} \left(\sin \left(\theta_z \cdot \frac{\pi}{180} \right) \cdot \cos \left(\gamma_s \cdot \frac{\pi}{180} \right) \right)$$

$$\theta_{\text{inc}} = 45.661$$

$$\gamma := 0$$

$$\theta_{\text{inc}} := \frac{180}{\pi} \cdot \text{acos} \left(\begin{array}{l} -\sin \left(\delta \cdot \frac{\pi}{180} \right) \cdot \cos \left(\Phi \cdot \frac{\pi}{180} \right) \cdot \cos \left(\gamma \cdot \frac{\pi}{180} \right) + \dots \\ + \cos \left(\delta \cdot \frac{\pi}{180} \right) \cdot \sin \left(\Phi \cdot \frac{\pi}{180} \right) \cdot \cos \left(\gamma \cdot \frac{\pi}{180} \right) \cdot \cos \left(\omega \cdot \frac{\pi}{180} \right) + \dots \\ + \cos \left(\delta \cdot \frac{\pi}{180} \right) \cdot \sin \left(\gamma \cdot \frac{\pi}{180} \right) \cdot \sin \left(\omega \cdot \frac{\pi}{180} \right) \end{array} \right)$$

$$\theta_{\text{inc}} = 45.661$$

$$\Omega := \frac{180}{\pi} \cdot \text{atan} \left(\frac{\tan \left(\alpha_s \cdot \frac{\pi}{180} \right)}{\cos \left(\gamma_s \cdot \frac{\pi}{180} \right)} \right)$$

$$\Omega = 45.606$$

$$\Omega := \Omega \cdot \frac{\pi}{180}$$

$$I_b := I_{\text{eppley}} \cdot \cos \left(\theta_{\text{inc}} \cdot \frac{\pi}{180} \right)$$

$$I_b = 629.012$$

$$I_d := I_{\text{tot}} - I_b$$

$$I_d = 70.988$$

Diffuse-Diffuse Calculations

$$w := 4.9$$

$$h := 4.39$$

$$Ds := \sqrt{[w \cdot (\cos(\phi))]^2 + (h - w \cdot \sin(\phi))^2}$$

$$Ds = 6.579$$

$$Db := \sqrt{[w \cdot (\cos(\phi))]^2 + (h + w \cdot \sin(\phi))^2}$$

$$Db = 6.579$$

$$F13 := \frac{w + h - Db}{2 \cdot h} \quad F13 = 0.309$$

$$F14 := \frac{w + h - Ds}{2 \cdot h} \quad F14 = 0.309$$

$$F23 := \frac{w + h - Ds}{2 \cdot h} \quad F23 = 0.309$$

$$F24 := \frac{w + h - Db}{2 \cdot h} \quad F24 = 0.309$$

$$F21 := \frac{Db + Ds - 2 \cdot w}{2 \cdot h} \quad F21 = 0.382$$

$$F34 := \frac{Db + Ds - 2 \cdot h}{2 \cdot w} \quad F34 = 0.447$$

$$F31 := \frac{w + h - Db}{2 \cdot w} \quad F31 = 0.277$$

$$F43 := F34 \quad F43 = 0.447$$

$$F41 := \frac{w + h - Ds}{2 \cdot w} \quad F41 = 0.277$$

$$A := \begin{pmatrix} 1 & 0 & -F13 \cdot \rho & -F14 \cdot \rho \\ 0 & 1 & -F23 \cdot \rho & -F24 \cdot \rho \\ 0 & 0 & 1 & -F34 \cdot \rho \\ 0 & 0 & -F43 \cdot \rho & 1 \end{pmatrix} \quad A = \begin{pmatrix} 1 & 0 & -0.182 & -0.182 \\ 0 & 1 & -0.182 & -0.182 \\ 0 & 0 & 1 & -0.264 \\ 0 & 0 & -0.264 & 1 \end{pmatrix}$$

$$\mathbf{b} := \begin{pmatrix} 0 \\ F21 \\ F31 \\ F41 \end{pmatrix}$$

$$\mathbf{b} = \begin{pmatrix} 0 \\ 0.382 \\ 0.277 \\ 0.277 \end{pmatrix}$$

$$\mathbf{G} := \mathbf{A}^{-1} \cdot \mathbf{b}$$

$$\mathbf{G} = \begin{pmatrix} 0.137 \\ 0.519 \\ 0.376 \\ 0.376 \end{pmatrix}$$

$$\tau4dd := G_2$$

$$\tau4dd = 0.519$$

$$\rho4fdd := G_1$$

$$\rho4fdd = 0.137$$

Beam-Diffuse Calculations

$$Z4 := \rho \cdot (1) \cdot \frac{\sin(\Omega + \phi)}{\cos(\Omega)}$$

$$Z4 = 0.603$$

$$wL := h \cdot \frac{\cos(\Omega)}{\sin(\Omega + \phi)}$$

$$wL = 4.298$$

$$wR := w - wL$$

$$wR = 0.602$$

$$\mathbf{A} := \begin{pmatrix} 0 \\ 0 \end{pmatrix}$$

$$\mathbf{B} := \begin{pmatrix} wL \cdot \cos(\phi) \\ wL \cdot \sin(\phi) \end{pmatrix}$$

$$\mathbf{C} := \begin{pmatrix} w \cdot \cos(\phi) \\ w \cdot \sin(\phi) \end{pmatrix}$$

$$\mathbf{E} := \begin{pmatrix} wL \cdot \cos(\phi) \\ h + wL \cdot \sin(\phi) \end{pmatrix}$$

$$\mathbf{D} := \begin{pmatrix} w \cdot \cos(\phi) \\ h + w \cdot \sin(\phi) \end{pmatrix}$$

$$\mathbf{F} := \begin{pmatrix} 0 \\ \mathbf{h} \end{pmatrix}$$

$$dls := \left| \sqrt{(\mathbf{F} - \mathbf{B})^T \cdot (\mathbf{F} - \mathbf{B})} \right| \quad dls = 6.144$$

$$drs := \left| \sqrt{(\mathbf{E} - \mathbf{C})^T \cdot (\mathbf{E} - \mathbf{C})} \right| \quad drs = 4.431$$

$$dlb := \left| \sqrt{(\mathbf{E} - \mathbf{A})^T \cdot (\mathbf{E} - \mathbf{A})} \right| \quad dlb = 6.144$$

$$drb := \left| \sqrt{(\mathbf{D} - \mathbf{B})^T \cdot (\mathbf{D} - \mathbf{B})} \right| \quad drb = 4.431$$

$$F13 := \frac{wL + h - dlb}{2 \cdot h} \quad F13 = 0.29$$

$$F14 := \frac{wL + h - dls}{2 \cdot h} \quad F14 = 0.29$$

$$F15 := \frac{dlb + w - wL - Db}{2 \cdot h} \quad F15 = 0.019$$

$$F16 := \frac{dls + w - wL - Ds}{2 \cdot h} \quad F16 = 0.019$$

$$F23 := \frac{drs + w - wR - Ds}{2 \cdot h} \quad F23 = 0.245$$

$$F24 := \frac{drb + w - wR - Db}{2 \cdot h} \quad F24 = 0.245$$

$$F25 := \frac{h + wR - drs}{2 \cdot h} \quad F25 = 0.064$$

$$F26 := \frac{h + wR - drb}{2 \cdot h} \quad F26 = 0.064$$

$$F34 := \frac{dlb + dls - 2 \cdot h}{2 \cdot wL} \quad F34 = 0.408$$

$$F35 := 0$$

$$F36 := \frac{h + Ds - drs - dls}{2 \cdot wL} \quad F36 = 0.046$$

$$F43 := F34$$

$$F45 := \frac{h + Db - drb - dlb}{2 \cdot wL} \quad F45 = 0.046$$

$$F46 := 0$$

$$F53 := 0$$

$$F54 := \frac{h + Db - drb - dlb}{2 \cdot wR} \quad F54 = 0.327$$

$$F56 := \frac{drb + drs - 2 \cdot h}{2 \cdot wR} \quad F56 = 0.068$$

$$F63 := \frac{h + Ds - drs - dls}{2 \cdot wR} \quad F63 = 0.327$$

$$F64 := 0$$

$$F65 := F56$$

$$A := \begin{pmatrix} 1 & 0 & -F13 \cdot \rho & -F14 \cdot \rho & -F15 \cdot \rho & -F16 \cdot \rho \\ 0 & 1 & -F23 \cdot \rho & -F24 \cdot \rho & -F25 \cdot \rho & -F26 \cdot \rho \\ 0 & 0 & 1 & -F34 \cdot \rho & -F35 \cdot \rho & -F36 \cdot \rho \\ 0 & 0 & -F43 \cdot \rho & 1 & -F45 \cdot \rho & -F46 \cdot \rho \\ 0 & 0 & -F53 \cdot \rho & -F54 \cdot \rho & 1 & -F56 \cdot \rho \\ 0 & 0 & -F63 \cdot \rho & -F64 \cdot \rho & -F65 \cdot \rho & 1 \end{pmatrix} \quad B := \begin{pmatrix} F14 \cdot Z4 \\ F24 \cdot Z4 \\ F34 \cdot Z4 \\ 0 \\ F54 \cdot Z4 \\ F64 \cdot Z4 \end{pmatrix}$$

$$A = \begin{pmatrix} 1 & 0 & -0.171 & -0.171 & -0.011 & -0.011 \\ 0 & 1 & -0.144 & -0.144 & -0.038 & -0.038 \\ 0 & 0 & 1 & -0.241 & 0 & -0.027 \\ 0 & 0 & -0.241 & 1 & -0.027 & 0 \\ 0 & 0 & 0 & -0.193 & 1 & -0.04 \\ 0 & 0 & -0.193 & 0 & -0.04 & 1 \end{pmatrix}$$

$$B = \begin{pmatrix} 0.175 \\ 0.148 \\ 0.246 \\ 0 \\ 0.197 \\ 0 \end{pmatrix}$$

$$G := A^{-1} \cdot B$$

$$\rho_{4\text{fbd}} := G_1$$

$$\tau_{4\text{fbd}} := G_2$$

$$\rho_{4\text{fbd}} = 0.235$$

$$\tau_{4\text{fbd}} = 0.206$$

$$G = \begin{pmatrix} 0.235 \\ 0.206 \\ 0.264 \\ 0.069 \\ 0.213 \\ 0.06 \end{pmatrix}$$

$$X := A^{-1} \cdot B$$

$$S1 := X_{1,1} - X_{2,1} + X_{3,1} - X_{4,1} \quad S1 = 69.765$$

$$S2 := (X_{5,1} - X_{6,1} + X_{7,1} - X_{8,1}) - (X_{1,1} - X_{2,1} + X_{3,1} - X_{4,1}) \quad S2 = 21.04$$

$$S3 := (X_{9,1} - X_{10,1} + X_{11,1} - X_{12,1}) - (X_{5,1} - X_{6,1} + X_{7,1} - X_{8,1}) \quad S3 = 17.845$$

$$S4 := (X_{13,1} - X_{14,1} + X_{15,1} - X_{16,1}) - (X_{9,1} - X_{10,1} + X_{11,1} - X_{12,1}) \quad S4 = 312.829$$

$$S5 := (X_{17,1} - X_{18,1} + X_{19,1} - X_{20,1}) - (X_{13,1} - X_{14,1} + X_{15,1} - X_{16,1}) \quad S5 = 127.026$$

$$S6 := X_{18,1} + X_{20,1}$$

$$S6 = 151.494$$

$$S1 + S2 + S3 + S4 + S5 + S6 = 700$$

$$Ib + Id = 700$$

APPENDIX 4

THE THERMAL RESISTOR NETWORK

ORIGIN := 1

σ := $5.67 \cdot 10^{-8}$

Air Properties at 300K:

ρ := 1.18

Cp := 1005

k := 0.0260

v := $1.614 \cdot 10^{-5}$

Pr := 0.71

g := 9.8

β := $\frac{1}{300}$

Input Parameters

Vin := 0.56

Tinleft := 32.7

Tinright := 32.7

Tinc := 22.8

Tinr := 22.8

Tout := 13

S2 := 19.8

S3 := 16.8

S4 := 307.5

$$S5 := 123$$

$$hbo := 23$$

$$hbi := 23$$

$$hgo := 24$$

$$hgi := 24$$

$$W := 0$$

Glazing/Shading Layer Properties

$$\epsilon_{3f} := 0.84$$

$$\rho_{3f} := 0.16$$

$$\rho_{4b} := 0.04$$

$$\rho_{4f} := 0.04$$

$$\epsilon_{4f} := 0.52$$

$$\epsilon_{4b} := 0.52$$

$$\tau_4 := 0.47$$

$$\epsilon_{5b} := 0.84$$

$$\rho_{5b} := 0.16$$

Initial Guesses

$$\begin{pmatrix} T2 \\ T3 \\ T4 \\ T5 \\ Tmar \\ Tmal \end{pmatrix} := \begin{pmatrix} 27.495 \\ 34.386 \\ 39.499 \\ 31.996 \\ 33.864 \\ 33.524 \end{pmatrix}$$

Calculate heat transfer coefficients

$$h_{12c} := 1.46 [(|T2 - Tinc|) \div 0.5]^{0.25} \quad h_{12c} = 2.556$$

$$h_{12r} := \frac{0.84 \cdot \sigma \cdot [(T2 + 273)^4 - (Tmr + 273)^4]}{T2 - Tmr} \quad h_{12r} = 5.049$$

$$Ra := \frac{g \cdot \beta \cdot |T3 - T2| \cdot 0.0127^3}{\nu^2} \cdot Pr$$

$$\text{Nu} := 0.42 \cdot \text{Ra}^{0.25} \cdot \text{Pr}^{0.012} \cdot \left(\frac{0.5}{0.0127} \right)^{-0.3}$$

$$\text{h23c} := \frac{k \cdot \text{Nu}}{0.0127} \quad \text{h23c} = 1.694$$

$$\text{h23r} := \frac{0.098 \cdot \sigma \cdot [(T3 + 273)^4 - (T2 + 273)^4]}{T3 - T2} \quad \text{h23r} = 0.624$$

$$\text{h23} := \text{h23c} + \text{h23r} \quad \text{h23} = 2.318$$

$$\text{h56} := \max \left(5, 8.6 \cdot \frac{W^{0.6}}{2.97^{0.4}} \right) + \frac{0.84 \cdot \sigma \cdot [(T5 + 273)^4 - (Tout + 273)^4]}{T5 - Tout} \quad \text{h56} = 9.921$$

**Calculate the long-wave radiative heat transfer coefficients
Within the Ventilated Cavity:**

$$\text{J5b3} := 0 \quad \text{J4f3} := 0 \quad \text{J4b3} := 0 \quad \text{J3f3} := 1$$

$$\text{J5b4b} := 0 \quad \text{J4f4b} := 0 \quad \text{J4b4b} := 1 \quad \text{J3f4b} := 0$$

$$\text{J5b4f} := 0 \quad \text{J4f4f} := 1 \quad \text{J4b4f} := 0 \quad \text{J3f4f} := 0$$

$$\text{J5b5} := 1 \quad \text{J4f5} := 0 \quad \text{J4b5} := 0 \quad \text{J3f5} := 0$$

Given

$$\text{J3f3} = \epsilon_{3f} \cdot \sigma \cdot [(T3 + 273)^4] + \rho_{3f} \cdot \text{J4b3}$$

$$\text{J4b3} = \rho_{4b} \cdot \text{J3f3} + \tau_4 \cdot \text{J5b3}$$

$$\text{J4f3} = \rho_{4f} \cdot \text{J5b3} + \tau_4 \cdot \text{J3f3}$$

$$\text{J5b3} = \rho_{5b} \cdot \text{J4f3}$$

$$J4b4b = \epsilon_{4b} \cdot \sigma \cdot [(T4 + 273)^4] + \rho_{4b} \cdot J3f4b + \tau_4 \cdot J5b4b$$

$$J4f4b = \rho_{4f} \cdot J5b4b + \tau_4 \cdot J3f4b$$

$$J5b4b = \rho_{5b} \cdot J4f4b$$

$$J3f4f = \rho_{3f} \cdot J4b4f$$

$$J4b4f = \rho_{4b} \cdot J3f4f + \tau_4 \cdot J5b4f$$

$$J4f4f = \epsilon_{4f} \cdot \sigma \cdot [(T4 + 273)^4] + \rho_{4f} \cdot J5b4f + \tau_4 \cdot J3f4f$$

$$J5b4f = \rho_{5b} \cdot J4f4f$$

$$J3f4b = \rho_{3f} \cdot J4b4b$$

$$J3f5 = \rho_{3f} \cdot J4b5$$

$$J4b5 = \rho_{4b} \cdot J3f5 + \tau_4 \cdot J5b5$$

$$J4f5 = \rho_{4f} \cdot J5b5 + \tau_4 \cdot J3f5$$

$$J5b5 = \epsilon_{5b} \cdot \sigma \cdot [(T5 + 273)^4] + \rho_{5b} \cdot J4f5$$

$$(J3f3 \quad J4b3 \quad J4f3 \quad J5b3 \quad J3f4b \quad J4b4b \quad J4f4b \quad J5b4b \quad J3f4f \quad \bullet \quad \bullet) := \bullet$$

$$(\bullet \quad \bullet \quad J4b4f \quad J4f4f \quad J5b4f \quad J3f5 \quad J4b5 \quad J4f5 \quad J5b5) := \bullet$$

$$\bullet := \text{Find}(J3f3, J4b3, J4f3, J5b3, J3f4b, J4b4b, J4f4b, J5b4b, J3f4f, \bullet, \bullet, \bullet, \bullet, \bullet, \bullet, \bullet, \bullet)^T$$

$$\bullet := \text{Find}(\bullet, \bullet, \bullet, \bullet, \bullet, \bullet, \bullet, \bullet, \bullet, \bullet, J4b4f, J4f4f, J5b4f, J3f5, J4b5, J4f5, J5b5)^T$$

$$J4f3 - J5b3 - J4b5 + J3f5 = 4.811$$

$$J3f3 + J5b3 - J4b3 - J4f3 - J4b4b - J4b4f + J3f4b + J3f4f = -16.509$$

$$J4f4b + J4f4f - J5b4b - J5b4f - J3f5 - J5b5 + J4b5 + J4f5 = 23.948$$

$$h35r := \frac{J4f3 - J5b3 - J4b5 + J3f5}{T3 - T5}$$

$$h35r = 2.013$$

$$h34r := \frac{J3f3 + J5b3 - J4b3 - J4f3 - J4b4b - J4b4f + J3f4b + J3f4f}{T3 - T4}$$

$$h34r = 3.229$$

$$h45r := \frac{J4f4b + J4f4f - J5b4b - J5b4f - J3f5 - J5b5 + J4b5 + J4f5}{T4 - T5}$$

$$h45r = 3.192$$

Solve the Matrix:

$$A := \begin{pmatrix} -h12c - h12r - h23 & h23 & 0 & \dots & \dots & \dots \\ h23 & -h35r - h34r - hgi - h23 & h34r & \dots & \dots & \dots \\ 0 & h34r & -h34r - hbi - h45r - hbo & \dots & \dots & \dots \\ 0 & h35r & h45r & \dots & \dots & \dots \\ 0 & hgi & hbi & \dots & \dots & \dots \\ 0 & 0 & hbo & \dots & \dots & \dots \end{pmatrix}$$

$$\begin{bmatrix} \dots & 0 & 0 & \dots \\ \dots & h35r & hgi & \dots \\ \dots & h45r & hbi & \dots \\ \dots & -h45r - h35r - hgo - h56 & 0 & \dots \\ \dots & 0 & -hgi - hbi - \frac{(\rho \cdot Vin \cdot 0.092) \cdot Cp}{0.5} & \dots \\ \dots & hgo & 0 & \dots \end{bmatrix}$$

$$\begin{bmatrix}
 \blacksquare & \blacksquare & \blacksquare & \blacksquare & \blacksquare & 0 \\
 \blacksquare & \blacksquare & \blacksquare & \blacksquare & \blacksquare & 0 \\
 \blacksquare & \blacksquare & \blacksquare & \blacksquare & \blacksquare & \mathbf{hbo} \\
 \blacksquare & \blacksquare & \blacksquare & \blacksquare & \blacksquare & \mathbf{hgo} \\
 \blacksquare & \blacksquare & \blacksquare & \blacksquare & \blacksquare & 0 \\
 \blacksquare & \blacksquare & \blacksquare & \blacksquare & \blacksquare & -\mathbf{hgo} - \mathbf{hbo} - \frac{(\rho \cdot \mathbf{Vin} \cdot 0.092) \cdot \mathbf{Cp}}{0.5}
 \end{bmatrix}
 \mathbf{b} :=
 \begin{bmatrix}
 -\mathbf{Tinr} \cdot \mathbf{h12r} - \mathbf{Tinc} \cdot \mathbf{h12c} - \mathbf{S2} \\
 -\mathbf{S3} \\
 -\mathbf{S4} \\
 -\mathbf{S5} - \mathbf{h56} \cdot \mathbf{Tout} \\
 \frac{-(\rho \cdot \mathbf{Vin} \cdot 0.092) \cdot \mathbf{Cp} \cdot \mathbf{Tinright}}{0.5} \\
 \frac{-(\rho \cdot \mathbf{Vin} \cdot 0.092) \cdot \mathbf{Cp} \cdot \mathbf{Tinleft}}{0.5}
 \end{bmatrix}$$

$$\begin{pmatrix}
 \mathbf{T2} \\
 \mathbf{T3} \\
 \mathbf{T4} \\
 \mathbf{T5} \\
 \mathbf{Tmar} \\
 \mathbf{Tmal}
 \end{pmatrix}
 := \mathbf{A}^{-1} \cdot \mathbf{b}
 =
 \begin{pmatrix}
 \mathbf{T2} \\
 \mathbf{T3} \\
 \mathbf{T4} \\
 \mathbf{T5} \\
 \mathbf{Tmar} \\
 \mathbf{Tmal}
 \end{pmatrix}
 =
 \begin{pmatrix}
 27.502 \\
 34.386 \\
 39.499 \\
 31.996 \\
 33.863 \\
 33.524
 \end{pmatrix}$$

$$\Delta \mathbf{Tinlet_to_outlet} := \frac{(2 \cdot \mathbf{Tmar} - \mathbf{Tinright}) + (2 \cdot \mathbf{Tmal} - \mathbf{Tinleft})}{2} - \frac{\mathbf{Tinright} + \mathbf{Tinleft}}{2}$$

$$\Delta \mathbf{Tinlet_to_outlet} = 1.988$$

Now Iterate